

APPLICATION OF LASER INDUCED DESORPTION TO STUDY VELOCITY-RESOLVED KINETICS

Dissertation zur Erlangung des
mathematisch-naturwissenschaftlichen Doktorgrades
"Doctor rerum naturalium"
der Georg-August-University Göttingen

im Promotionsprogramm Chemie
der Georg-August University School of Science (GAUSS)

vorgelegt von
Kim Papendorf
aus Galway

Göttingen, 2022

Betreuungsausschuss

Prof. Dr. Alec M. Wodtke
Institut für Physikalische Chemie, Georg-August-Universität Göttingen

Prof. Dr. Dirk Schwarzer
Max-Planck-Institut für Multidisziplinäre Naturwissenschaften

Mitglieder der Prüfungskommission

Referent: Prof. Dr. Alec M. Wodtke
Institut für Physikalische Chemie, Georg-August-Universität Göttingen

Korreferent: Prof. Dr. Dirk Schwarzer
Max-Planck-Institut für Multidisziplinäre Naturwissenschaften

Weitere Mitglieder der Prüfungskommission

Prof. Dr. Theofanis N. Kitsopoulos
Institut für Physikalische Chemie, Georg-August-Universität Göttingen

Prof. Dr. Claus Ropers
Max-Planck-Institut für Multidisziplinäre Naturwissenschaften

Prof. Dr. Jürgen Troe
Institut für Physikalische Chemie, Georg-August-Universität Göttingen

Prof. Dr. Thomas Zeuch
Institut für Physikalische Chemie, Georg-August-Universität Göttingen

Abstract

In this work, I present a new method to measure velocity-resolved kinetics (VRK) of chemical reactions on surfaces. Ultra-fast laser-induced desorption (LID) is utilized as a tool to directly measure coverages of adsorbates. This highly non-linear process leads to a very high heating rate at the surface, which favors the desorption reaction, and other reactions are interrupted or suppressed.

In principle, all kind of adsorbates are desorbed simultaneously and particle selection is achieved afterwards during the detection. Gating of the detector allows for mass selection and resonance-enhanced multi photon ionization (REMPI) can be used to selectively ionize. Resolving the velocity of the desorbing flux is achieved by using the ion-imaging technique with slice imaging. Scanning the delay between the detection and the molecular beam (MB) pulse, which initiates a reaction, yields the kinetic trace of the selected particle. In this work, I have chosen to study the VRK of the thermal desorption (TD) reaction of carbon monoxide, oxygen and ammonia from platinum. The results are compared to previous measurements and serve as a proof-of-concept for this new method. I have discovered that this method works especially well for slow reactions at low temperatures where traditional methods struggle because they measure the thermally desorbing flux, which simply is too weak if the reaction is slow. This allows the extension of the temperature range of CO TD kinetics towards lower temperatures, which shows Arrhenius-like behavior over a range of more than 150 K.

In principle, this method can be applied to chemical reactions on surfaces with more reactants as well, by dosing the surface with one adsorbate and initiating the reaction with a MB pulse of a different adsorbate. One could choose to measure the kinetic trace of the reactants or products. It should also be possible to record the kinetic trace of reaction intermediates, which are not stable in the gas phase, and therefore can not be measured in the TD flux. Although measuring the kinetic trace of reaction intermediates is beyond the scope of this work, I am able to show that it is possible to induce the desorption of O-atoms, which are unstable particles that play a role as reaction intermediate in many oxidation reactions. Important examples of catalytic oxidations are the CO oxidation, hydrogen oxidation and the Ostwald process. For those examples, the kinetic of the elementary steps are not entirely clear and are still in discussion to this day. Measuring kinetic traces of reaction intermediates with the LID-VRK method has the potential to provide invaluable information about the kinetics of elementary steps in catalytic reactions.

Acknowledgments

I want to thank Alec for the opportunity to carry out my PhD studies. I appreciate your ideas and constructive criticism, which was always fair and appropriate. I really like your style of leading this research group, where everybody is inspired by your passion for science.

I am grateful to Sven, for teaching me everything in the lab and how to work self-reliant. Your positive attitude makes everybody around you smile.

Thank you, Kai, for teaching me how to work with ion imaging and molecular beams. Also thank you for all fruitful discussions and meeting we had and for reviewing my dissertation.

I also would like to thank Tianli, for supporting me in the lab and continuing our joint project.

I would also like to give a special shoutout to our technicians, Tim and Reinhard, who helped us tremendously by designing and building our imaging system and molecular beam chamber.

A special thanks goes to the rest of the Wodtke group for the moral support and the laughs we had in the lab or at the lunch table.

I am very grateful for my mother Sabine for all the conversations and emotional support over the course of my whole life. I also want to thank my grandfather for his financial support during my academic studies and for being an inspiration for our whole family.

List of publications

Kai Golibrzuch, Sven Schwabe, Tianli Zhong, Kim Papendorf, and Alec M. Wodtke.
"Application of an Event-Based Camera for Real-Time Velocity Resolved Kinetics"
In: *Journal of Physical Chemistry A* (March 23, 2022). doi.org/10.1021/acs.jpca.2c00806.

Kim Papendorf, Kai Golibrzuch, Tianli Zhong, Sven Schwabe, Theofanis Kitsopoulos, Alec M. Wodtke. "Velocity-resolved laser-induced desorption for kinetics on surface adsorbates" In: *Chemistry - methods* (2022). Publication in process.

Contents

1	Introduction	17
2	Theory	19
2.1	Thermal desorption (TD) kinetics	19
2.2	Laser induced desorption (LID)	20
2.3	Competing Photon Induced Effects	23
3	Experiment	25
3.1	Vacuum chamber	25
3.2	Sample Holder	27
3.3	Surface preparation	28
3.3.1	Auger spectroscopy	28
3.3.2	Low energy electron diffraction (LEED)	29
3.4	Molecular beam (MB) setup	31
3.5	Laser setup	33
3.5.1	Desorption Laser	33
3.5.2	Detection Laser	34
3.6	Detection setup	35
3.6.1	Ion imaging	35
3.6.2	Slice imaging	36
4	Methods	39
4.1	MCP-Gate	40
4.2	Laser Delay	41
4.2.1	Density to flux conversion	41
4.2.2	Hyperthermal distributions	41
4.3	Nozzle Delay	42
4.3.1	Velocity-resolved kinetics (VRK)	42
4.3.2	LID-VRK	43
4.4	Repeller Delay	45
4.5	REMPI scans	47
4.6	Surface diffusion	48
4.7	Image Analysis	50
5	Results	53
5.1	Laser power correction	53
5.2	Molecular beam characterization	54
5.2.1	Opening delay	55
5.2.2	opening duration	55

5.2.3	Translational temperature	58
5.2.4	Rotational temperature	59
5.3	CO on platinum	60
5.3.1	CO dissociation	61
5.3.2	Adsorption of CO	63
5.3.3	LID rate constant	66
5.3.4	Internal energy of the LID flux	67
5.3.5	Kinetic energy of the LID flux	68
5.3.6	Laser pulse duration dependence	69
5.3.7	Laser fluence dependence	71
5.3.8	Desorption kinetics	73
5.4	Oxygen on platinum	77
5.4.1	Dissociation of Oxygen	77
5.4.2	Kinetic energy of the LID flux	79
5.4.3	Laser pulse duration dependence	81
5.4.4	Laser fluence dependence	81
5.4.5	Desorption kinetics	83
5.5	Ammonia on platinum	84
5.5.1	Dissociation of ammonia	84
5.5.2	Desorption kinetics	85
6	Discussion	87
6.1	The LID process	87
6.2	Kinetic measurements	88
6.3	Binding energy of CO on Pt(111)	90
6.4	Oxygen desorption kinetics	90
6.5	Reaction intermediates	91
6.6	Summary	91
A	Pixel to mm conversion	93
B	Kinetic traces	95
	Bibliography	99

List of Figures

2.1	Visualization of a Pt(332) stepped surface	19
2.2	Simulation of laser heating	22
3.1	Overview of the vacuum chamber	26
3.2	The sample holder	27
3.3	Example Auger spectra of contaminated and clean platinum	28
3.4	LEED pictures of Pt(111) and Pt(332)	30
3.5	The molecular beam chamber	31
3.6	The main chamber	33
3.7	Sketch of the imaging setup	37
4.1	Timing scheme of the experiment	39
4.2	Sketch of the MB pulse trajectory	45
4.3	Sketch of a model for diffusion on the surface after LID	48
4.4	Example LID images and profiles	51
5.1	Power law of the detection laser	53
5.2	Determination of the nozzle opening delay with delayed extraction.	55
5.3	Arrival time distributions of the MB pulse for several opening durations	56
5.4	Gauss fit parameters of the MB pulse for several opening durations	57
5.5	Velocity distributions of the MB pulses from both nozzles	58
5.6	Rotational temperature of the MB pulse for different conditions	59
5.7	REMPI scans of the (1,1) transition for the LID and TD flux	60
5.8	Raw images of the CO dissociation fragments	61
5.9	Overview of the CO dissociation	62
5.10	CO adsorption curve on Pt(111)	63
5.11	CO adsorption isotherms on Pt(111)	64
5.12	Isosteric heat of adsorption of CO on Pt(111)	65
5.13	Decay of surface coverage due to LID	66
5.14	REMPI spectra of the LID flux and the MB pulse	67
5.15	TOF, velocity and kinetic energy distribution of the CO LID flux	68
5.16	Laser pulse duration dependence of CO	69
5.17	REMPI spectra of CO for 2 different laser pulse durations	70
5.18	Laser fluence power laws of CO	71
5.19	Kinetic energy distributions of CO for several laser fluences	72
5.20	Hyperthermal shift of CO	72
5.21	Kinetic traces of CO desorption	73
5.22	CO desorption Arrhenius plots	74
5.23	Influence of the repetition rate on the steady state coverage	75

5.24	Raw images of O ₂ dissociation	78
5.25	Temperature dependence of the kinetic energy distribution of the O- atom LID flux	79
5.26	Laser pulse duration dependence of the oxygen	81
5.27	Laser fluence dependence of oxygen	82
5.28	Kinetic trace of oxygen atom desorption	83
5.29	MCP gate scans of ammonia	84
5.30	Kinetic traces of ammonia desorption	85
6.1	Comparison of CO desorption rate constants to literature	88
6.2	Comparison of NH ₃ desorption rate constants to literature	89
A.1	Raw image of the extractor grid	93
B.1	Kinetic traces of CO: Pt(332), (1,1) transition, PGV nozzle	95
B.2	Kinetic traces of CO: Pt(332), (1,1) transition, PGV nozzle, low rep- etition rates	95
B.3	Kinetic traces of CO: Pt(332), (0,0) transition, ELT nozzle	96
B.4	Kinetic traces of CO: Pt(332), (1,1) transition, ELT nozzle	96
B.5	Kinetic traces of CO: Pt(111), (1,1) transition, PGV nozzle	97

List of Tables

3.1	REMPI transitions	35
5.1	Characteristics of the MB pulses of both nozzles	54
5.2	Summary of obtained rotational and vibrational temperatures of CO	70
6.1	Comparison of CO Arrhenius parameters to literature	90

Abbreviations

CAD computer-aided design	25
ELT Even Lavie type	32
FWHM full-width at half-maximum	47
LEED low-energy electron diffraction	25
LID laser-induced desorption	3
LITD laser-induced thermal desorption	21
MB molecular beam	3
MCP multi-channel plate	35
MPI multi-photon ionization	34
PGV Parker General Valve	32
REMPI resonance-enhanced multi photon ionization	3
RGA residual-gas analyzer	25
ROI region of interest	50
TD thermal desorption	3
TPD temperature programmed desorption	82

TOF time-of-flight	40
UHV ultra-high vacuum	25
VMI velocity map imaging	35
VRK velocity-resolved kinetics	3

Chapter 1

Introduction

Heterogeneous catalysis is widely used on the industrial scale to produce important chemical compounds, e.g. the Haber-Bosch process and the Ostwald process to produce fertilizer for the agriculture. The critical reactions involve small gas molecules adsorbing on a metal catalyst surface and reacting in a Langmuir-Hinshelwood type mechanism. Understanding the kinetics of the elementary steps of the catalytic processes has been the goal of many scientists to this day. Measuring the kinetic rate constants of the elementary steps enables accurate simulations of reactions and predictions of new catalyst materials, which is vital to improve their efficiency. Obtaining reaction rate constants, usually involves measuring either the uptake rate of reactants or the formation rate of reaction products.

One important new method, that has been developed over the last years, is velocity-resolved kinetics (VRK). This state-of-the-art method measures the desorption rate of reaction products while resolving their velocity, simultaneously. The velocity contains additional information about the reaction processes and reaction site that have led to the formation of the products. This technique has helped to explain the mechanism of CO oxidation on platinum. This catalytic reaction has been studied extensively in the past[1, 2, 3, 4, 5, 6, 7] and was thought to be well understood. Nonetheless, VRK was used to show that the mechanism was not well understood that the bimodal kinetic energy distribution of the CO₂ products is due to the reaction at different active sites[8, 9, 10]. VRK was also applied to hydrogen oxidation[11] and ammonia oxidation[12] with great success.

In this work, I show that VRK can be combined with ultra-fast laser-induced desorption (LID) to measure surface reaction kinetics. Instead of recording the kinetic trace of the product flux, LID is used to directly probe the time-dependent coverage on the surface that has not desorbed yet. This enables the measurement of slow reactions or low temperatures, which are inaccessible to VRK, and possibly enables the measurement of reaction intermediate kinetics. The possibility of using LID to measure desorption kinetics was already shown by Ertl *et al.* [13], who also suggested its application to intermediates in catalytic reactions. Because of their highly reactive nature, intermediates only exist for a short period of time on the surface during the reaction. Recording their transient surface coverage dynamics is highly desirable to reveal the kinetics of the elementary steps that are involved. One important example reaction would be the oxidation of hydrogen on platinum, which is one of the most simple, yet extensively studied reaction in heterogeneous catalysis. The kinetics are fundamentally still not understood and can not be predicted by

theory[11]. Since this reaction involves OH-radical as intermediate, it would be a prime candidate to apply this new LID-VRK method to.

To understand how this method works, it is imperative to learn about LID. The general idea is that short laser pulses induce a rapid Laser heating during the time of the laser pulse on the surface with only little penetration depth[14, 15, 16]. Under this extremely high heating rate in the order of 10^{10} K s^{-1} , surface reactions that are favored under normal conditions are bypassed and the induced desorption is highly favored[17, 18]. Thus taking an instantaneous snapshot of the coverage of all adsorbates on the surface and transferring them into the gas phase where they can be detected and analyzed.

With the emergence of ultra-fast lasers, capable of producing fs-laser pulses, LID yields increased manifold. This required a new mechanism to explain this effect of the shorter pulses[19, 20, 21]. On the sub-ps timescale, the surface electrons and phonons are decoupled and the electrons reach temperatures and heating rates which are much higher than with ns-lasers. The hot electrons can couple to adsorbates and induce desorption[22, 23, 24, 25, 26]. Ultra-fast LID was studied extensively on platinum[27, 28, 29, 20, 21, 18, 30], paladium[19, 31, 32, 33] and copper[34, 35, 36, 37]. It is consensus that the desorption yield depends non-linearly on the laser fluence and also increases with shorter laser pulse length. The internal energy of the desorbing flux is hyperthermal, especially vibration is found to be highly excited. For the translational energy of the desorbing flux, different results can be found, ranging from thermal kinetic energy distributions to fast hyperthermal distributions. This shows that LID strongly depends on the system and the experimental conditions.

Chapter 2

Theory

This chapter will give a brief explanation of the theoretical background of thermal desorption (TD) kinetics and laser-induced desorption (LID). They are the central concepts for the new method which is presented in this work.

2.1 Thermal desorption (TD) kinetics

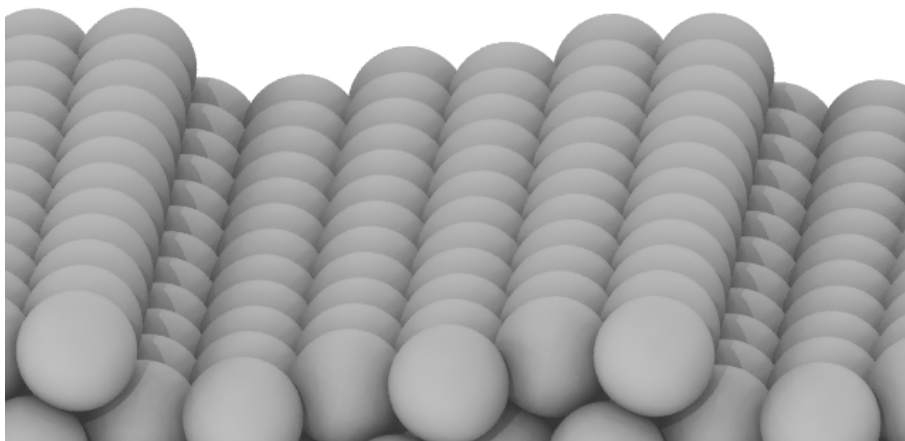


Figure 2.1: Visualization of a Pt(332) stepped surface.

A simple model for TD kinetics was developed by Serri *et al.* [38] for the desorption of NO from Pt(111) and can be applied to CO as well. It includes the diffusion on the terraces and between steps and terraces, as well as adsorption and desorption from the terrace. The concentration of adsorbates on surfaces is expressed as surface coverage θ :

$$\theta = \frac{\text{Number of adsorbates}}{\text{Number of surface atoms}} \quad (2.1)$$

in units of monolayers (ML). In the low coverage limit, the average distance between adsorbates is large and interactions between adsorbates can be neglected. Diffusion of CO on platinum is slow compared to other metal surfaces[39], but still fast compared to most other adsorbates[38]. Adsorption occurs predominantly on the terrace binding sites because of the high sticking probability for CO[4] and the low step density of Pt(111) in the order of 0.1 to 1 % which depends on small errors in the cutting angle in the manufacturing process. According to detailed balance, this implies that desorption also originates mainly from terrace sites. Therefore, adsorption and desorption from steps is neglected in this model. Regardless, steps play an important role in thermal desorption kinetics from single-crystal surfaces, even in small concentrations[38], because adsorbates often bind more strongly to step sites compared to terrace sites due to the lower coordination and higher reactivity of the metal atoms at the step[3]. To study the effect of steps, surfaces with a well-defined step density are used, which are produced by cutting a single crystal with a specific cutting angle. Pt(332) with a step density of 16.7 % is just one example of a high step density surface. It consists of hexagonal Pt(111) terraces which are 5 atoms wide and separated by single atomic steps which are visualized in Figure 2.1.

The crucial quantity which decides the nature of the desorption kinetics is the ratio between the coverage and the step density[38]. If the coverage is larger than the step density, the steps will be saturated quickly and most adsorbates will bind to the terrace binding sites[6]. Hence, the measured desorption rate will be dominated by desorption from the terrace sites, which is an elementary step of first order. If the dosed coverage is smaller than the step density, most adsorbates will bind to the step sites[38]. Then the measured rate constant is an effective rate constant, which consists of diffusion from the step to the terrace site and subsequent desorption from the terrace. Assuming that the diffusion is fast compared to the desorption, the desorption from terraces is the rate determining step. In both cases, the desorption would show a single exponential decay, each with a different desorption rate. Usually, the first case is observed on Pt(111) and the second case on a stepped surface like Pt(332). But if a Pt(111) surface with unusually high the step density is used, both desorption pathways can be observed simultaneously, resulting in a double exponential decay[7].

2.2 Laser induced desorption (LID)

To describe how photons can induce the desorption of adsorbates from metal surfaces, I will first describe the metal surface system itself and then the interaction with photons followed by introducing adsorbates to the system. The metal surface system can be divided into two subsystems, surface phonons and surface electrons and a separate temperature T_{ph} and T_{el} can be assigned to each subsystem[40, 41]. They couple and equilibrate with each other on a timescale of a few ps[25] and the surface phonons couple to the bulk phonons on a timescale of ms. Though, diffusion of hot electrons is much faster and accounts for the majority of the heat conductivity to the bulk[42].

When polished metal surfaces are exposed to photons in the visible to near-infrared region, most photons are reflected as the surface acts as a mirror, but a small portion of the light is absorbed. Photons are absorbed by the surface electrons, which disturbs the equilibrium. To reestablish the equilibrium, the energy is dissipated by

coupling to phonons or hot electron diffusion to the bulk. The macroscopic increase in the temperature of the sample is negligible because of the use of pulsed laser beams, which introduce less power over time into the sample compared to cw-lasers. The absorbed energy is dissipated into the bulk crystal, which has a large heat capacity and mass compared to the surface. Finally, the heat is transferred from the crystal to the sample holder and manipulator.

When introducing adsorbates to the metal surface, the coupling to the phonon and electron heat bath is on the ultra-fast timescale[25]. This coupling can induce desorption of the adsorbates from the metal surface by exciting the surface-adsorbate bond to a high vibrational state. Due to the fast coupling, direct adsorbate photo excitation is rarely observed on metal surfaces.

Phonon mediated desorption

With ns-lasers, the pulse duration is large compared to the coupling time between the electrons and phonons of just a few ps[25]. Hence, the electron and the phonon bath are always in equilibrium. Short laser pulses lead to an extremely fast increase of the surface phonon temperature, with a heating rate of 10^{10} K/s[43, 39, 21]. This rapid temperature rise can cause LID of adsorbates thermally by coupling of the excited phonons to the surface-adsorbate bond, which leads to vibrational ladder climbing[41] and eventually desorption. This process is often called laser-induced thermal desorption (LITD) [43, 44, 45, 13, 46].

Electron mediated desorption

To observe effects of direct electron mediated desorption, laser pulses with a duration shorter than the coupling time between electrons and phonons are necessary, which is achieved by using a fs-laser. The changes of T_{ph} and T_{el} caused by the laser pulse can be simulated by numerically with the formulas[48, 49]:

$$C_{\text{el}} \frac{dT_{\text{el}}}{dt} = \frac{d}{dx} \left(k_{\text{el}} \frac{dT_{\text{el}}}{dx} \right) - g(T_{\text{el}} - T_{\text{ph}}) + S(z, t) \quad (2.2)$$

and

$$C_{\text{ph}} \frac{dT_{\text{ph}}}{dt} = k_{\text{ph}} \frac{d^2 T_{\text{ph}}}{dx^2} + g(T_{\text{el}} - T_{\text{ph}}) \quad (2.3)$$

They describe the time evolution of T_{ph} and T_{el} with the specific heat capacities C , the thermal conductivities k and the electron-phonon coupling constant g . The first term describes the heat conductivity into the bulk perpendicular to the surface in x direction, and the second term describes the coupling from the electrons to the phonons. The last term, $S(z, t)$, is the laser pulse which couples the phonon energy to the electrons.

Figure 2.2 shows the result of a heat diffusion simulation of T_{ph} and T_{el} after a 110 fs laser pulse with 2.5 mJ cm^{-2} , which is indicated in blue. The initial temperature increase of T_{el} is very steep, which results in a heating rate in the order of 10^{16} K/s. For the first 5 ps, T_{ph} and T_{el} are out of equilibrium and the peak electronic temperature is much higher than the peak phonon temperature. This high peak electronic temperature corresponds to numerous excited electrons, also referred to as 'hot electrons', which couple to the adsorbate surface bond and can cause vibrational ladder climbing and subsequent desorption. The electron mediated

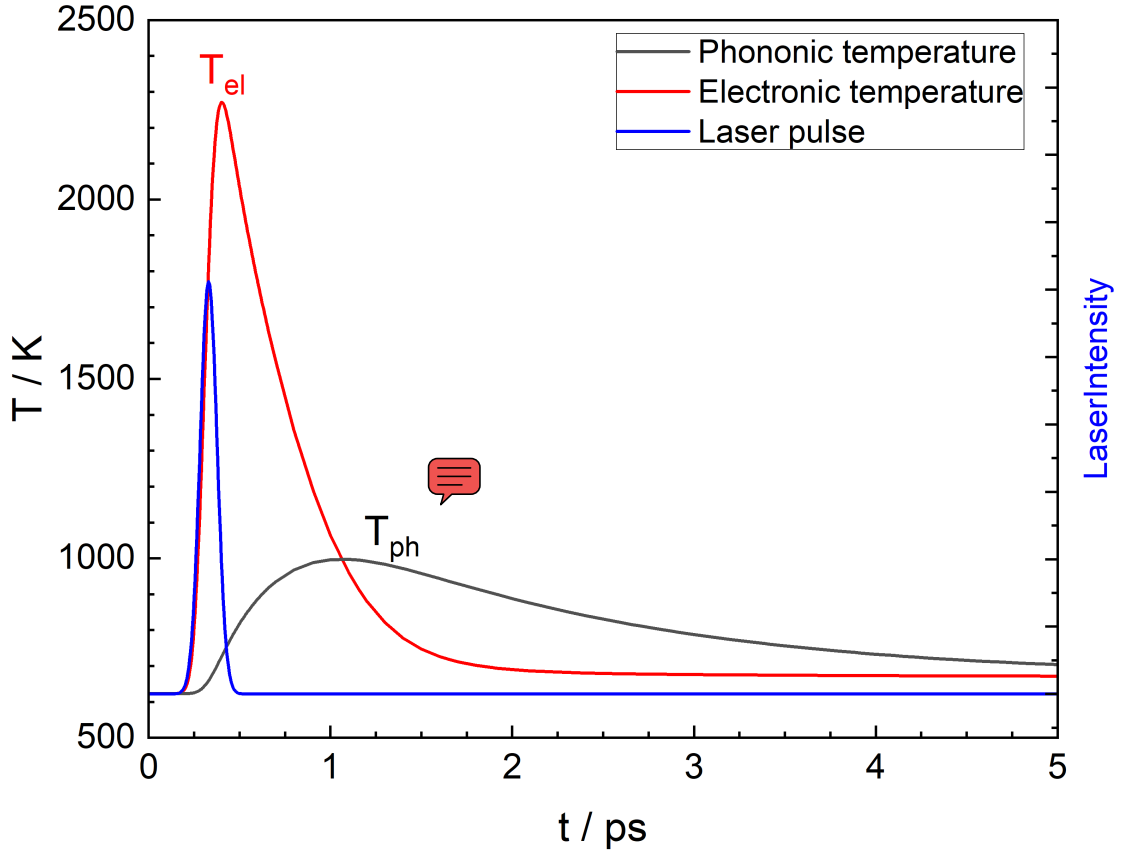


Figure 2.2: Simulation of T_{ph} and T_{el} on a platinum surface after a 110 fs laser pulse. The laser pulse is shown in blue to demonstrate the timescale. Typical experimental values $F_{\text{abs}} = 2.5 \text{ mJ cm}^{-2}$ and $T_{\text{S}} = 623 \text{ K}$ were used for the simulation. Optical constants from Werner *et al.* [47] were used.

desorption pathway does not replace the phonon mediated desorption, but occurs in addition to it and leads to an increase in total desorption yield. The desorption probability increases exponentially with the number of hot electrons, or peak T_{el} [24] respectively. Variation of the surface temperature changes the peak T_{el} but the effect is very small compared to the effect of the laser. Because of the exponential relationship between the desorption probability and T_{el} , the effect of T_{S} on the desorption yield is negligible. Hence, the rate constant of the LID process, k_{LID} , is approximately independent of T_{S} .

The electron mediated desorption mechanism is indicated by the nonlinear dependence of the desorption yield Y on the laser fluence F which is the pulse energy divided by the laser spot area on the surface:

$$Y \propto F^k \quad (2.4)$$

with a typical value for k of 2-8[40] compared to the approximately linear dependence $k \approx 1$ in the phonon mediated desorption (LITD)[13]. Also, the desorption yield increases with decreasing pulse duration, which is not the case for LITD. Typically, the rotational and vibrational temperature of the desorbing flux greatly surpass

the surface temperature and the velocity distribution is hyperthermal and does not follow a Maxwell-Boltzmann distribution[50, 37].

2.3 Competing Photon Induced Effects

When irradiating the sample with a laser beam, other possible energy pathways which compete with desorption must be considered. This includes ablation, adsorbate dissociation, -diffusion and chemical reactions between adsorbates[21]. Ablation has to be avoided because it leads to the destruction of the surface, which renders any data incomparable to previous data. To avoid ablation, using fs-laser pulses for ultra-fast LID is advantageous because less laser fluence is required to reach the same desorption yield as with LITD[18]. Under the extremely high heating rates in LID, the difference in the activation energy between desorption, diffusion, dissociation and chemical reactions becomes negligible, and the prefactor determines the desorption rate[18]. According to transition-state theory, the prefactor of a reaction increases exponentially with the entropy of the transition state. For desorption the transition state is further away from the surface which leads to a higher entropy than the competing pathways which all have a transition state close to the surface. Thus, desorption is the dominating process when illuminating a surface-adsorbate system with ultra-short laser pulses while the competing pathways are suppressed[18] and can be neglected. During this work, I did observe some fragmentation of CO, but it was not caused by the LID process on the surface(see Section 5.3.1). Laser induced diffusion has been reported on metals for atomic oxygen on Pt(111)[51] enabled by the very large binding energy of atomic oxygen. For the kinetic measurements in this work, laser induced diffusion can be neglected anyway, because it has no influence on the surface coverage.

Chapter 3

Experiment

All experiments were conducted in an ultra-high vacuum (UHV)-chamber, where the sample is dosed with the adsorbates and then exposed to a laser beam, which induces the desorption. The desorbing flux is ionized by a second laser beam and then detected. This chapter introduces the individual parts and aspects of the experiment.

3.1 Vacuum chamber

In order to perform surface science experiments, it is imperative to use UHV in the order of 10^{-10} mbar. The sample surface needs to stay clean for the time of the experiment and not be contaminated by background gas particles. Also, any interaction of the deployed gas with background gas is undesired. Ideally, only the adsorbate/surface system and possible reaction products of interest need to be considered, while any other particles are neglected.

The main chamber is pumped by a turbomolecular pump (Leybold, Turbovac 450i), backed by a second turbomolecular pump (Leybold, Turbovac SL80H). The UHV base pressure is measured with a hot-filament ion gauge to $6 \cdot 10^{-10}$ mbar. A residual-gas analyzer (RGA) (Stanford Research Systems, RGA 200) is used to monitor the partial pressures of the residual gases that constitute the background pressure.

The computer-aided design (CAD) drawing in Figure 3.1 gives an overview of the stainless steel UHV chamber. The apparatus consists of a surface cleaning chamber (2), the main chamber (3) and the imaging detection (5), which are connected vertically. The molecular-beam chamber (4) is connected horizontally to the main chamber and is presented in more detail in Section 3.4. The surface preparation chamber consists of an Ar ion gun (Specs, IQE 11/35), an Auger spectrometer (STAIB Instruments, ESA 100) and a low-energy electron diffraction (LEED) spectrometer (Specs, ErLEED 100). The surface cleaning procedure is described in Section 3.3. The main chamber holds the repeller grid and extraction grid of the detection setup (see Section 3.6) and the sample holder (see Section 3.2) which is connected to the manipulator (1). Calcium fluoride windows are installed on both sides of the main chamber for the entrance and exit of the two laser beams (see Section 3.5). These windows are sealed with O-rings and differentially pumped by a separate turbomolecular pump (Pfeiffer, HiPace 80). The ion gauge and the RGA are mounted on a T-piece which is connected to the main chamber.

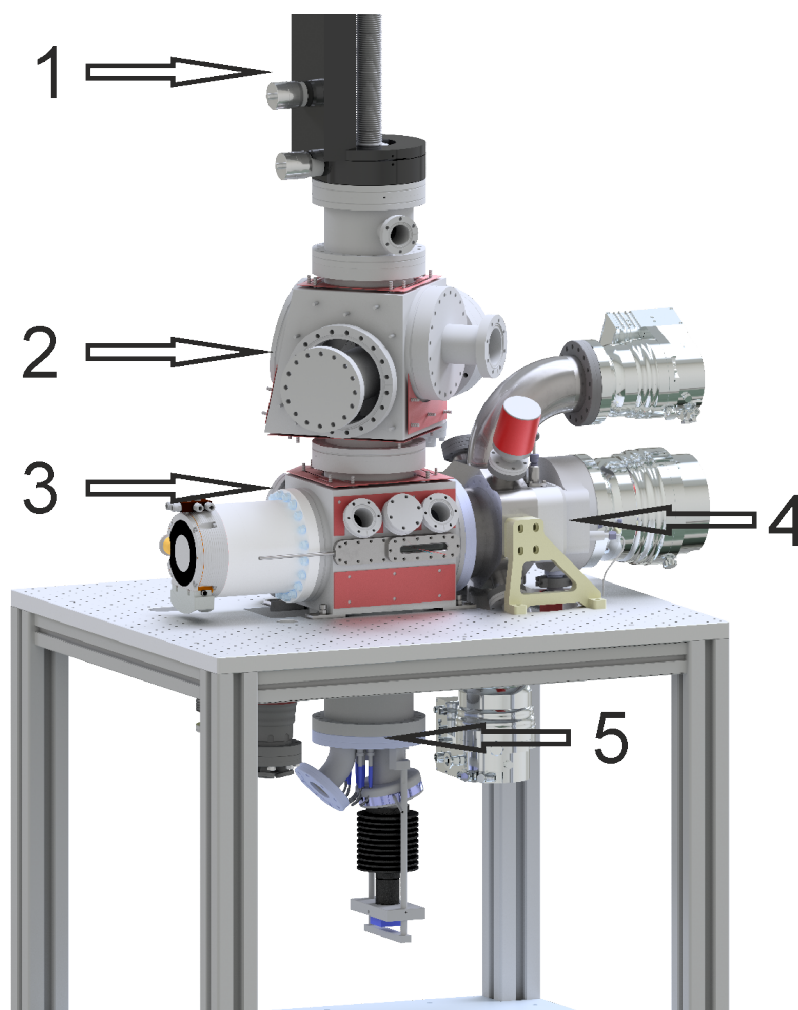


Figure 3.1: Overview of the vacuum chamber. The CAD drawing shows the vacuum chamber from the outside containing: manipulator (1) which is used to move the sample holder, surface preparation chamber (2), main chamber (3), Molecular beam chamber (4) and Imaging detection (5). The turbo-molecular pumps are attached on the sides of the chamber and below it.

3.2 Sample Holder

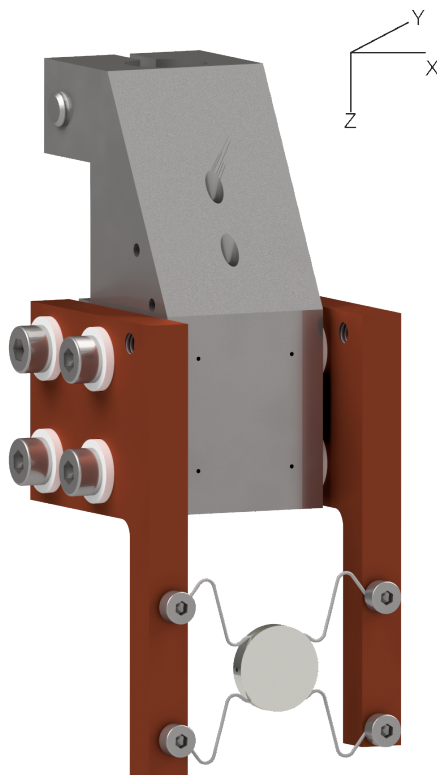


Figure 3.2: CAD 3D-model of the sample holder. It consists of the main body(gray), two copper arms(brown), two tungsten wires and the sample crystal.

The sample holder (see Figure 3.2) is connected at the top of the main body to a 4-fold axis manipulator (VACGEN, Scienta XY) which allows the sample to be moved between the surface preparation chamber and the main chamber. The sample can also be rotated around the z -axis (in the xy -plane, see Section 3.6.1) but the polar angle is fixed. A Pt(332) single crystal (MaTeck, one side polished, 0.1° accuracy, 10 mm diameter, 2 mm thickness) or a Pt(111) single crystal (MaTeck, one side polished, 0.1° accuracy, 10 mm diameter, 2 mm thickness) is mounted onto the sample holder and held by two tungsten wires.

A power supply (Elektro Automatik PSI5080, 640 W, 20A) provides a direct heating current up to 20.4 A which allows the sample to be heated resistivity up to 900°C . A proportional-integral-derivative (PID) controller is used to stabilize the sample at the desired temperature. The current is connected to the copper arms, which are electrically isolated from the main body. The two tungsten heating wires hold the sample in place and connect it to the copper arms, allowing the current to flow. The sample holder can also be cooled by water as cooling agent via a small pipe which is welded to the stainless-steel body. To monitor the surface temperature, T_s , a type-N thermocouple is attached to a small hole on the side of the sample. An addition type-N thermocouple is attached to the stainless-steel body to monitor the temperature of the sample holder itself.

3.3 Surface preparation

After installing a new sample, the surface is contaminated by large amounts of other elements and is cleaned for a longer period of time. The following cleaning cycle was employed and repeated daily until no more contaminants could be detected, but at least once per day.: First, the sample is sputtered by Ar^+ ions with 10 mA and 2 keV for 10 minutes. Then the sample is annealed at 1050 K in $5 \cdot 10^{-7}$ mbar oxygen for 20 minutes followed by annealing at 1100 K in UHV. During the annealing process, carbon contamination from the bulk diffuses to the surface. The oxygen removes the carbon contamination by oxidizing it to CO and CO_2 , which readily desorbs. The second annealing step removes any residual oxygen left on the surface. After the sample is cooled down the cleanness is verified by Auger spectroscopy and LEED which are both surface sensitive methods with only a few nm penetration depths.

3.3.1 Auger spectroscopy

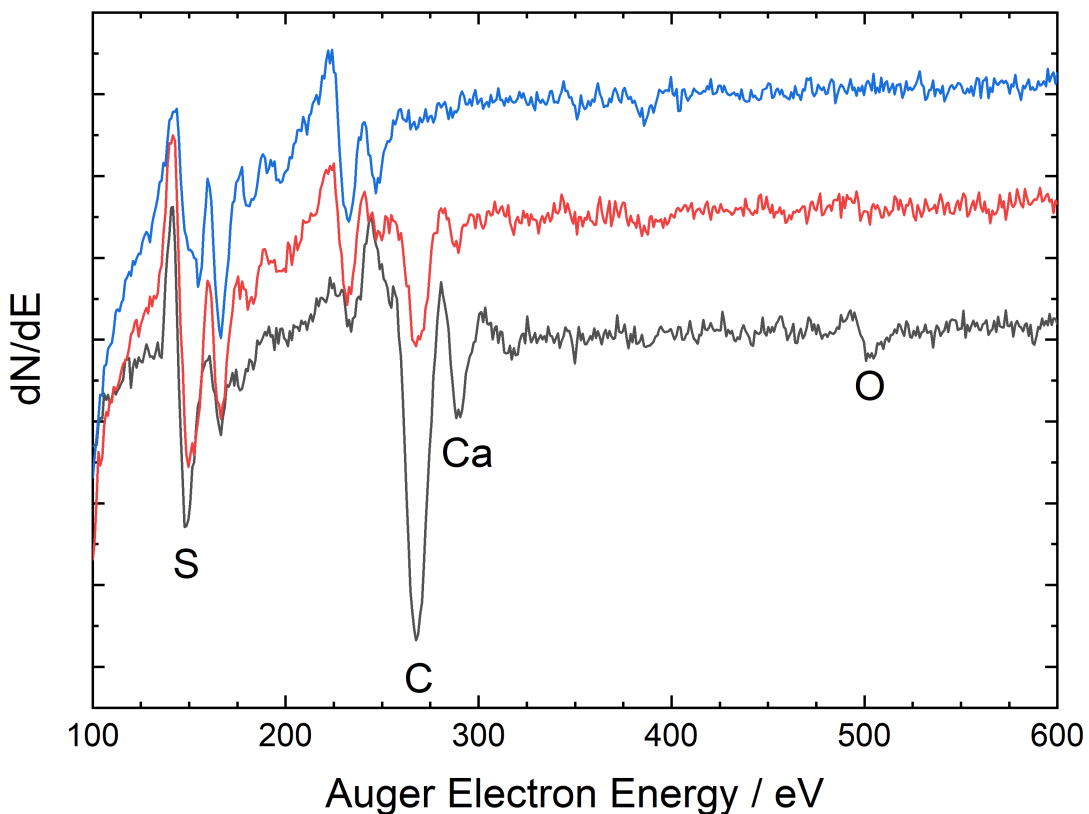


Figure 3.3: Example Auger spectra. Comparing a new sample before cleaning (black), the same sample after 9 cleaning cycles (red) and after several days of annealing in oxygen (blue). The peak positions of the most common contaminants are marked. Unmarked peaks belong to platinum.

Auger spectroscopy was used to detect small impurities on the surface. The Auger spectra were recorded with 3 kV energy with a detection limit of 1% and were compared qualitatively to literature spectra and analyzed quantitatively using tabulated element sensitivities[52].

Example spectra at different stages of the cleaning process of a new sample are shown in Figure 3.3. Before any cleaning, traces of sulfur (152 eV), calcium (291 eV) and oxygen (503 eV) as well as a lot of carbon (272 eV) were found. The sulfur peak overlaps with a peak of the platinum spectrum, but the amount of sulfur could be evaluated by comparing the relative intensities of the platinum peaks. After 9 cleaning cycles, only C remained as contamination on the surface. After several days of annealing in oxygen, the C contamination was largely removed from the outer region of the bulk and the spectrum of bare platinum was recorded.

In the daily inspection, the peak positions of carbon and oxygen were the main indicators of the surface's purity and other contaminants were not observed again. The emergence of weak peaks of the platinum surface at 357 eV and 390 eV were also helpful indicators, since they only appear if the surface cleanness is good. Usually, the carbon contamination is below the detection limit, after one cleaning cycle.

3.3.2 Low energy electron diffraction (LEED)

LEED is a technique to measure the diffraction pattern of single crystal surfaces. It is surface sensitive because the penetration depth of the electrons into the crystal is very small due to their low kinetic energy. The electron beam is collimated onto the surface where the electrons are diffracted. The pattern of scattered electrons is visualized on a phosphor screen. A simple charge-coupled device (CCD) camera is employed to take an image of the diffraction pattern on the phosphor screen. Figure 3.4 displays the LEED diffraction patterns of Pt(111) and Pt(332). The bottom image of Pt(111) shows the hexagonal pattern of the (111) terraces, and the bottom image of Pt(332) shows that the spots of the (111) terraces are split into doublets due to the regular pattern of the steps[53].

The diffraction pattern is useful for a qualitative evaluation of the surface quality. The clarity of the diffraction spots is an indicator for surface contamination because they break the high symmetry of the single crystal surface structure. Hence, the diffraction spots blur out and eventually disappear with increasing degree of impurities. The qualitative evaluation of the diffraction pattern is part of the daily inspection to ensure clean and stable conditions for the sample.

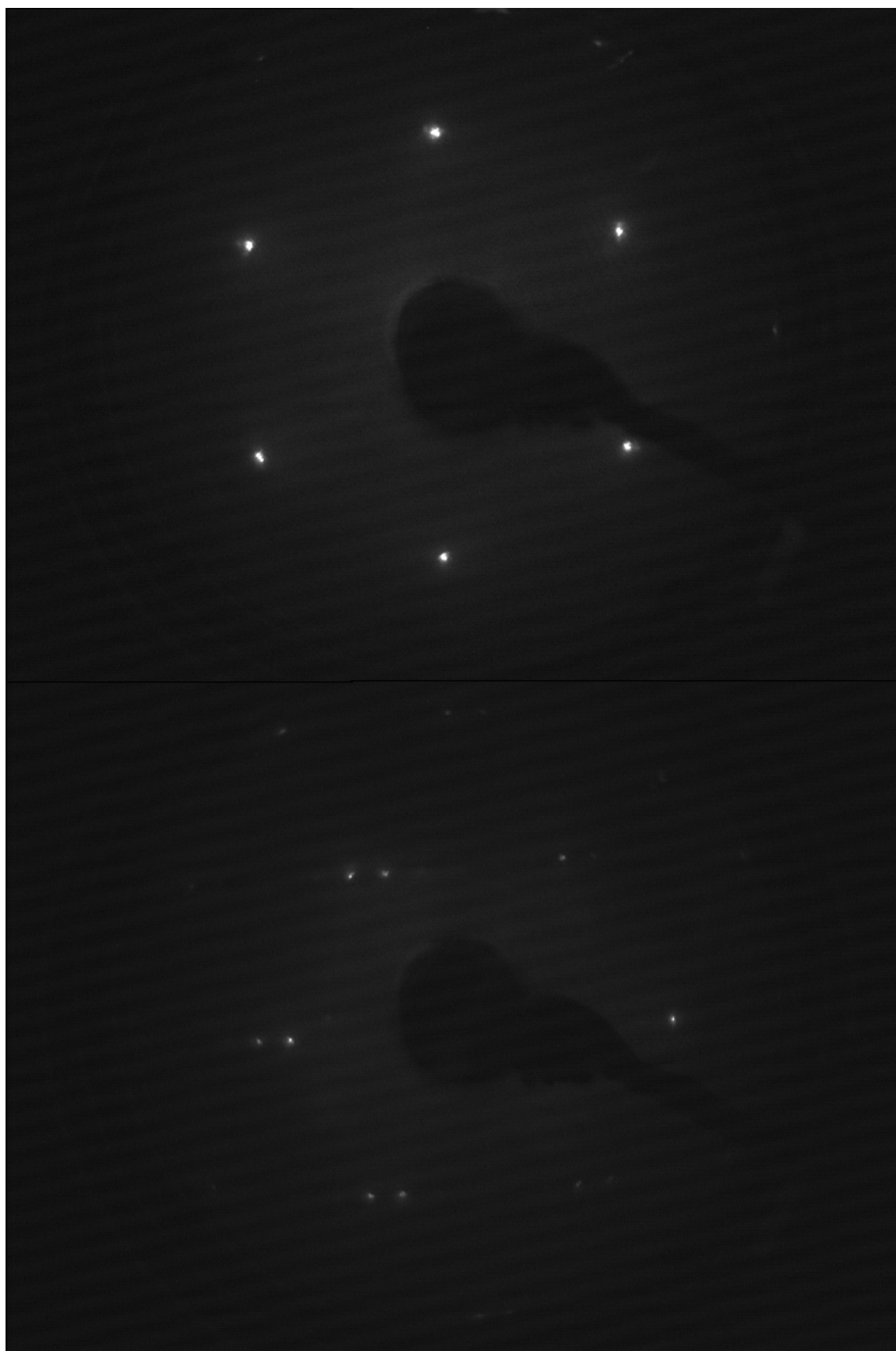


Figure 3.4: Pictures of the LEED diffraction pattern of Platinum. Pt(111) in the top panel and Pt(332) in the bottom panel. Taken with 234 eV and 242 eV electron kinetic energy, respectively.

3.4 Molecular beam (MB) setup

To dose the sample with adsorbates two different methods were used in this work. The first and simplest one is to leak a constant amount of gas molecules into the UHV-chamber, where the leakage rate and pumping rate will result in an equilibrium pressure. From the pressure p and the dosing time t_{dose} the dose D can be calculated by:

$$D = p \cdot t_{\text{dose}} \quad (3.1)$$

which is usually expressed in Langmuir ($1\text{L} = 1.33 \cdot 10^{-6}$ mbar s) where 1 L corresponds to one full monolayer, assuming a sticking probability of 1. With a typical pressure of 10^{-7} to 10^{-6} mbar one monolayer is reached within seconds and any vacancies on the surface due to desorbing molecules are quickly replenished. Therefore, experiments with a constant dosing through the leak valve operate in the high-coverage limit.

Alternatively, a MB pulse is used for dosing the surface with adsorbates. The gas molecules are stored under a backing pressure behind a valve. When a trigger is sent to the nozzle, there is a delay, t_0 , before the valve starts to open for the opening duration t_{open} . Upon opening, the molecules rapidly expand inside the source-chamber due to the pressure gradient. The expansion cools the internal degrees of freedom, which leads to very narrow translational - and rotational distributions, while also increasing the velocity in the direction away from the nozzle. But for small molecules the vibration cooling is not very efficient and therefore less important. Furthermore, the effective velocity of the MB pulse can be adjusted by seeding the beam in lighter or heavier carrier gases.

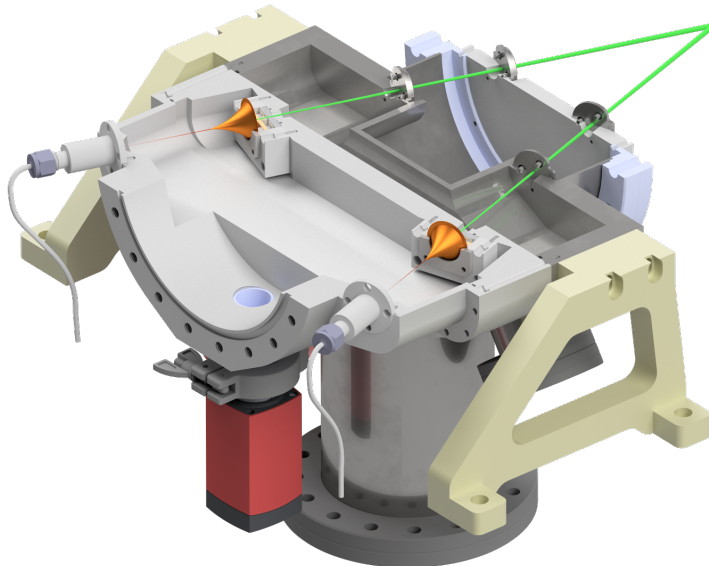


Figure 3.5: Cut through the CAD 3D-model of the MB chamber. Following the MB paths (light green lines) from left to right: Source chamber, first and second differential pumping stage, which are separated by skimmers (orange) and pinholes. The sample is placed in the crossing point of the two beams. The distance from the nozzle to the sample, $d_{\text{S-N}}$, is 375 mm.

Two MB sources are available which use the same source chamber and differential pumping stages which are pumped by Turbo-molecular pumps (Pfeiffer, HiPace 700 and HiPace 400). The geometry of the MB chamber is shown in Figure 3.5. A 1 mm Skimmer is installed in the wall that separates the source chamber from the first differential pumping stage to extract a small solid angle of the MB pulse. The second differential stage is separated by pinholes which are 2 mm in diameter. Both molecular beam pulses hit the sample after a travel distance of $d_{S-N} = 375$ mm with an angle α of 19° with respect to the surface normal. A Parker General Valve (PGV) nozzle and a home-build Even Lavie type (ELT) nozzle[54] are used with a backing pressure of 2 bar each. The PGV nozzle produces MB pulses with a typical pulse duration of $300 \mu\text{s}$ while the ELT nozzle gives shorter pulses with a typical pulse duration of $150 \mu\text{s}$. The dose per MB pulse is larger when using the PGV nozzle.

To optimize the dose, the MB was used without seeding gas. The parameters of the MB were compromised between maximizing the dose per pulse and minimizing the pulse duration for temporal resolution. The adjusted parameters are the backing pressure, the opening duration t_{open} and the repetition rate f_{RR} of the nozzle.

3.5 Laser setup

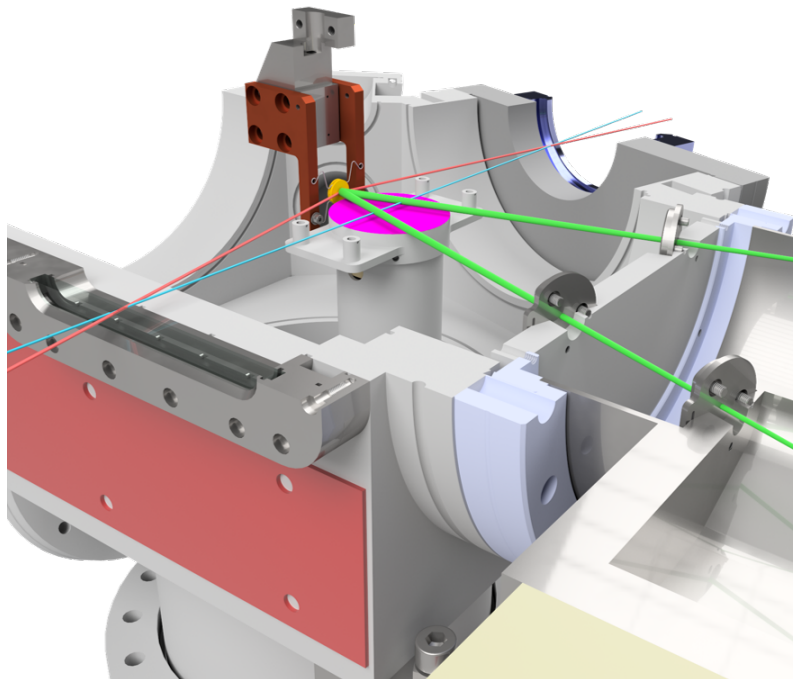


Figure 3.6: Cut through the CAD 3D-model of the main chamber. It shows the MB trajectories (light green lines, compare Figure 3.5), the LID laser beam path (red line) and the detection laser beam path (light blue line) relative to the sample (yellow). All beam pass through in between the extractor grid (magenta) and the repeller grid (not shown).

In this work, two different laser beams are utilized which are represented by the light blue (detection laser) and red line (desorption laser) in Figure 3.6 which shows the geometry of the laser beam paths relative to the sample and the molecular beam (MB) trajectories. The detection laser beam path lies parallel to the surface at a distance of 8 to 10 mm and the desorption laser hits the surface at an incidence angle $\beta \approx 70^\circ$ with respect to the surface normal.

3.5.1 Desorption Laser

The desorption laser beam is approximately Gaussian and horizontally polarized, parallel to the plane of incidence. It is focused mildly onto the surface by a lens ($f = 300$ mm) which is positioned at a distance $d \approx 220$ mm from the surface. The focus lies in between the sample and the laser exit window. It is undesirable to focus tightly because the number of irradiated adsorbates scales with the effective beam area on the surface, and also to avoid damage to the sample.

The laser fluence F is the time integrated flux of the laser radiation per unit area and is calculated from the pulse energy and the effective beam area:

$$F = \frac{E}{A_{\text{beam}}} \quad (3.2)$$

The effective beam area, A_{beam} , is calculated from the effective beam radius which is smaller than the Gaussian beam radius by a factor of $\sqrt{2}$. The Gaussian beam radii were measured with the knife-edge method to 2.2 mm and 2.0 mm. The focusing lens reduces A_{beam} in both dimensions while the incidence angle β increases the spot size only in one dimension:

$$A_{\text{beam}} = \pi r_1 r_2 \cdot \left(\frac{f-d}{f} \right)^2 / \cos \beta \approx 1.5 \text{mm}^2 \quad (3.3)$$

The absorbed fluence $F_{\text{m}}^{\text{athrmabs}}$ is the fraction of the fluence that is not reflected:

$$F_{\text{abs}} = F \cdot (1 - R) \quad (3.4)$$

The reflectance R of a polished platinum surface is 91 % [47] and is a function of the laser incident angle β , the surface temperature T_{S} and the polarization of the laser pulse. Additionally, the fluence was corrected for losses at the laser entrance window, which was measured to $\approx 6\%$.

The source for the laser pulses is a Ti:Sapphire laser (Coherent Libra, 800 nm, 100 fs, 1 kHz) which is pumped by a frequency doubled Nd:YLF laser (523 nm, 80 kHz). The pulse duration is variable by adjusting the compressor, which changes the frequency-chirping and is measured by an autocorrelator. It has been shown that the direction of the chirping (positive or negative) has no effect on desorption yield [30]. The optimized pulse duration reaches a minimum at 100 fs. The pulse energy E is adjusted to a level below the ablation threshold using a combination of a half-wave plate and a thin-film polarizer. The repetition rate is reduced to 50 Hz to match the repetition rate of the detection laser and the applied pulse energy is in the range between 100 and 300 μJ which is monitored and recorded during measurements. Usually, the fluctuations are less than 2% and any data with larger variation was discarded.

3.5.2 Detection Laser

Molecules in this work are detected by either non-resonant multi-photon ionization (MPI) or resonance-enhanced multi photon ionization (REMPI). REMPI is a very efficient ionization technique and quantum state specific, but is only applicable to some molecules. Non-resonant MPI is less efficient and ionizes all molecules and quantum states. Both ionization methods are nonlinear and require high laser intensities, which is achieved by tightly focusing the beam with a lens ($f=250$ mm).

REMPI detection is accomplished with a tunable dye laser (Sirah, Precision-Scan) pumped by the second harmonic of a Nd:YAG laser (Continuum Powerlite 8000, 50 Hz, 200 mJ). The dye laser is operated with Pyridine 1 (LDS 698) in Ethanol, with a nominal tuning range of 667-720 nm. After third-harmonic generation, the resulting wavelength lies in the UV-region at 222-240 nm with a pulse energy of 1-2 mJ and horizontal polarization. The pulse energy is monitored and recorded during the measurements and can vary by 5 to 10%. The cause for this large fluctuation is the phase matching of the fundamental and second harmonic wave in the third harmonic generation: Since the BBO crystal is not externally cooled, it heats up over time and needs to be rotated manually to optimize the phase matching. The relevant REMPI transitions that were used in this work are summarized in Table 3.1.

Particle	Transition	Wavelength	#Photons	Reference
CO	$B^1\Sigma_g^+ \leftarrow X^1\Sigma_g^+$	230 nm	(2+1)	Tjossem <i>et al.</i> [55]
O	$3p^3P_J \leftarrow 2p^3P_J$	226 nm	(2+1)	Bamford <i>et al.</i> [56]

Table 3.1: REMPI transitions relevant to this work.

For non-resonant MPI detection, the same Ti:Sapphire oscillator is used as for the desorption laser to seed a home-build regenerative amplifier which yields the 800 nm laser pulses with a variable delay between the detection laser and the desorption laser. For the ionization of CO and O-atoms REMPI was employed while for NH₃ non-resonant MPI was used. Molecular oxygen was ionized with the same UV laser wavelength as O-atoms, which lies in the Herzberg continuum[57].

3.6 Detection setup

The first step to detect desorbing particles is their ionization using the detection laser systems which were described in Section 3.5. The positively charged ions are directed and focused onto an electron multiplier detector, where the ion impact leads to an ejection of multiple electrons. The signal is further amplified by accelerating the ejected electrons onto another sheet, which can be repeated many times. This detection method has a high sensitivity capable of detection even single ions because the primary electrons are multiplied by many orders of magnitude and the resulting electron current can be recorded with an oscilloscope or visualized by a phosphor screen.

3.6.1 Ion imaging

The ion imaging technique was developed by Chandler and Houston[58] and has seen several improvements like velocity map imaging (VMI)[59] and slice imaging[60]. In this work, ion imaging is performed in spatial mode without VMI. The sketch of the ion imaging setup is shown in Figure 3.7 and depicts the coordinate system to describe the trajectories of the desorbing particles is defined in the lab frame: The xy -plane lies parallel to the repeller (2) and extractor grid (3), the x -axis normal to the surface (1), the y -axis parallel to the surface (1) and the z -axis along the flight tube (4). The blue line represents a desorption trajectory that is ionized and accelerated downwards by the repeller pulse (red vector). Together with the projected initial velocity, \vec{v}_{xy} (blue vector), they add up to the resulting trajectory (magenta line). The ion imaging system is based on the setup used previously by Harding *et al.* [61] and Harding [62].

The two parallel grids (Nickel, 41 mm diameter, 5 mm distance) are positioned between the sample and the molecular beam source in x-direction. The extractor grid is grounded while the repeller grid is connected to a high voltage pulser which switches between 0 V and +3 kV with a rise time of 80 ns and a fall time of several 100 μ s. When the repeller voltage is deactivated, the space between the grids acts as field-free region and when activated, a homogeneous electrical field is formed between the grids. The flight tube allows the ions a flight distance of $d_{\text{tube}} = 320$ mm from the extractor grid to the multi-channel plate (MCP) detector, which consists of two subsequent MCPs in chevron arrangement. A constant voltage of +900 V is applied

to the second MCP, while on the first MCP a voltage of -800 V is applied through a pulser with a variable pulse length up to 500 ns and a rise and fall time of 28 ns. The MCP detector records not only the number of ion impacts but also the position in the xy -plane where the impact occurred, which enables the spatial resolution of ion imaging. As phosphor screen, both P43 (545 nm, 1 ms decay time) and P47 (400 nm, 100 ns decay time) were used and biased by a constant high voltage of 4.3 kV. A 50 mm lens focuses the luminescent light onto a complementary metal-oxide semiconductor (CMOS) camera (LaVision, M-lite) and the data is processed via the DaVis software. The camera is operated at 5 Hz which results in a maximum exposure time t_{exposure} of 200 ms.

3.6.2 Slice imaging

The detection laser focus is positioned in front of the surface at the same y and z position as the laser beam spot. This maximizes the density of desorbing molecules in the detection laser focus because the maximum of the desorbing angular distribution is normal to the surface (x -direction). Desorbing trajectories with a velocity component in y -direction are still ionized because the detection laser focus is large along the propagation direction. But only desorbing trajectories with a very small velocity component in the z -direction are ionized because the detection laser focus is very small in this direction. Hence, from the 3-D desorbing Newton half sphere (orange cone) only a slice in the xy -plane is ionized (blue line). The width of the slice in z -direction is determined by the size of the laser beam spot on the surface, the size of the detection laser focus and the distance between them. In ion imaging the inverse Abel-transformation is often used to reconstruct the 3-D Newton sphere from the recorded image which is a 2-D projection. Since the detected slice is basically only two-dimensional, this transformation is not necessary, as in slice imaging[60].

Additionally to the slicing in space, the desorbing flux is also sliced in velocity space. By choosing the time delay between the two laser pulses, only a certain slice of the velocity distribution is ionized and detected. Higher or lower velocities miss the detection laser in x -direction and are therefore not ionized. The slicing immediately yields the velocity of the detected flux.

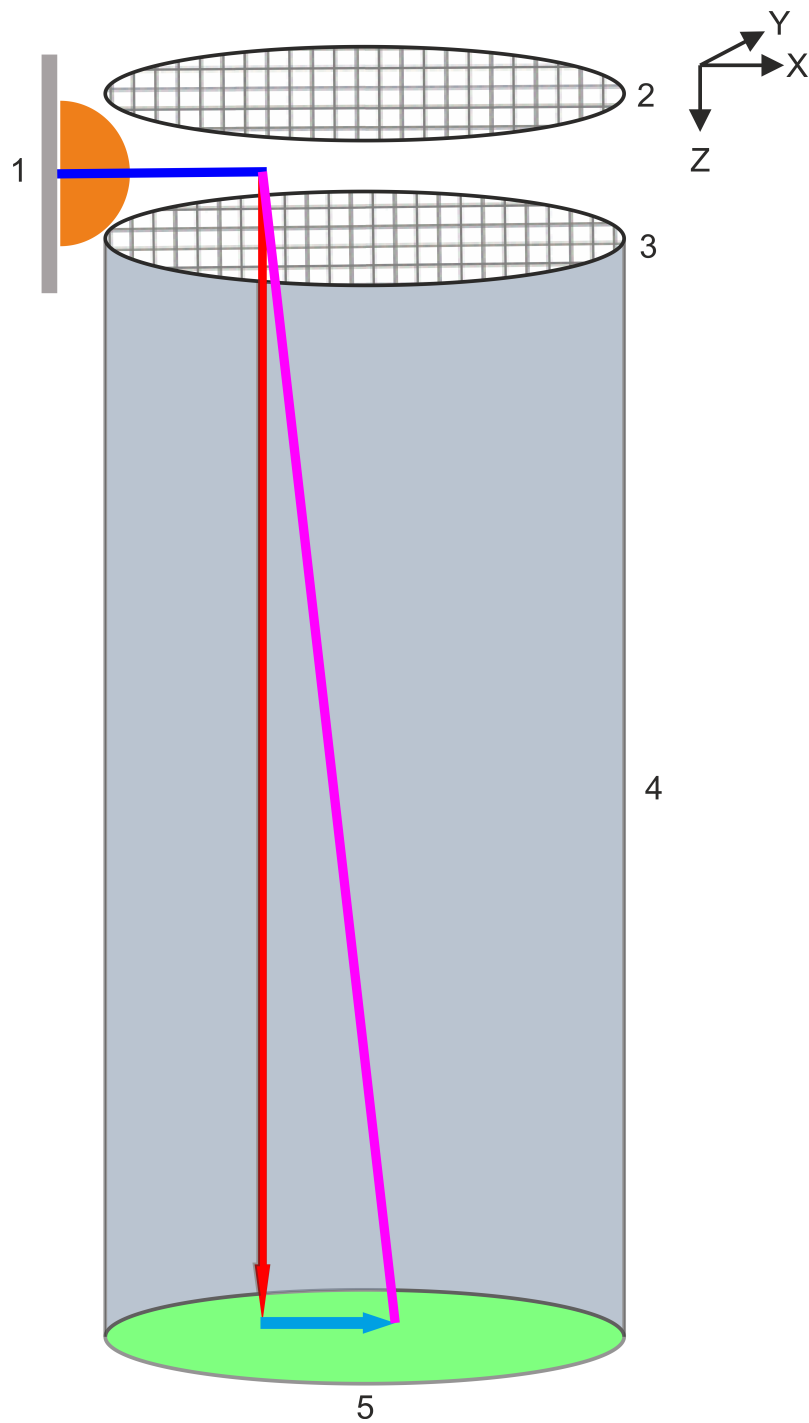


Figure 3.7: Sketch of the imaging setup showing the sample (1), repeller grid (2), extractor grid (3), flight tube (4) and MCP detector (5). Also depicted are the 3-D desorbing Newton half sphere (orange cone), Initial desorption trajectory \vec{v}_{xy} (blue line), trajectory after repeller pulse (magenta line), repeller pulse vector (red arrow) and projected initial trajectory vector (blue arrow).

Chapter 4

Methods

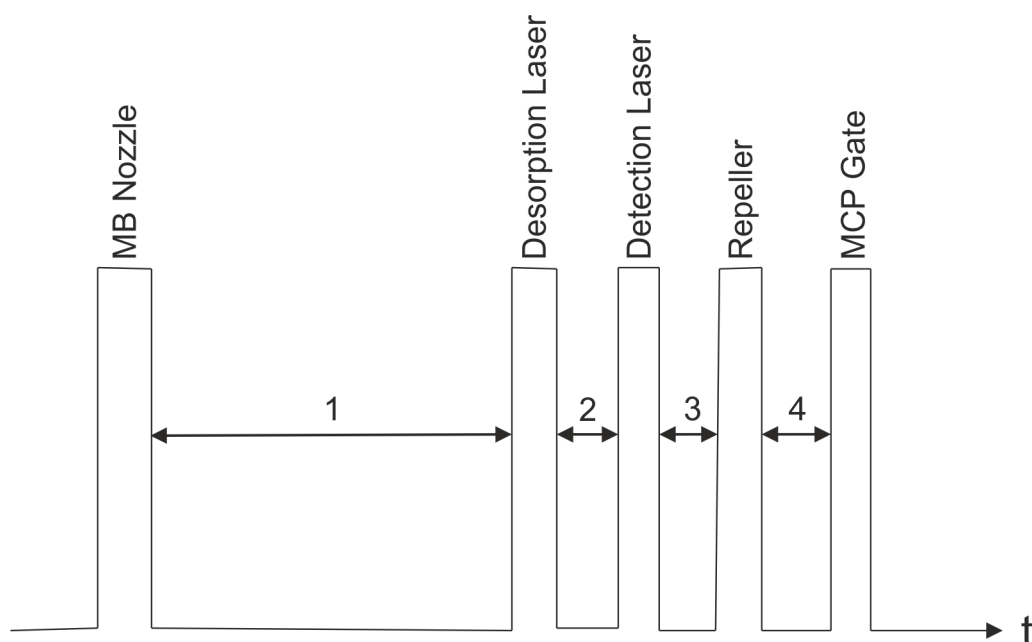


Figure 4.1: The timing scheme of the experiment consists of the pulses triggering the MB, the lasers and the detection. The delays between the pulses labeled 1 through 4 are called: Nozzle delay (1), Laser delay (2), Repeller delay (3) and MCP gate (4).

The timing scheme of relevant pulses in the experiment is shown in Figure 4.1. The desorption laser acts as the master clock, which all other pulses are referenced to. The detection laser pulse, repeller pulse and MCP gate pulse are synchronized to one another to ensure that changing one delay does not influence the others. All delays are configured with a delay generator (Berkley Nucleonics Corporation, Model 577) which can be controlled remotely by the DaVis software. This enables the synchronization of the delay scan with the camera recording the respective images. When the repetition rate of the nozzle f_{RR} is changed, as described in Section 3.4, then the repetition rate of the desorption laser, the repeller and the MCP gate are changed accordingly.

4.1 MCP-Gate

The acceleration a_z that the repeller voltage exerts on the ionized particles perpendicular to the xy -plane is derived by equating the Coulomb force F_C of the electric field $E = \frac{U}{d_{\text{grids}}}$ and Newton's second law of motion in z -direction F_z :

$$F_z = m \cdot a_z = q \cdot E = F_C \quad (4.1)$$

$$a_z = \frac{q \cdot E}{m} = \frac{q \cdot U}{m \cdot d_{\text{grids}}}, \quad (4.2)$$

with the charge of the particle q , the applied repeller voltage U , the distance between the grids d_{grids} and the mass of the ions m . The acceleration continues until the ions leave the electrical field through the bottom grid. The velocity trajectory results from vector addition of the initial velocity \vec{v}_{xy} and the velocity applied by the electric field, \vec{v}_z , which are perpendicular to each other (see red and blue arrow in Figure 3.7). \vec{v}_z is much larger than \vec{v}_{xy} , hence the resulting ion trajectory is predominantly going in z -direction. The velocity \vec{v}_z is given by:

$$\vec{v}_z = \vec{a}_z \cdot t_E, \quad (4.3)$$

with the time the ions spend inside the electric field, t_E . This time is calculated by integrating over the flight distance z and the time-of-flight (TOF) t between the grids:

$$\int_{z_{\text{start}}}^{z_{\text{end}}} dz = \int_0^{t_E} \vec{v}_z dt = \int_0^{t_E} \vec{a}_z \cdot t_E dt \quad (4.4)$$

$$z_{\text{end}} - z_{\text{start}} = \Delta z = \frac{\vec{a}_z \cdot t_E^2}{2} \rightarrow t_E = \sqrt{\frac{2 \cdot \Delta z}{\vec{a}_z}} \quad (4.5)$$

The z -coordinates, z_{start} and z_{end} , at the start and end of t_E , can also be expressed as relative z position $z_{\text{rel}} = \Delta z / d_{\text{grids}}$. Inserting Equation (4.5) into Equation (4.3) yields the velocity in z -direction:

$$\vec{v}_z = \sqrt{2 \cdot \Delta z \cdot \vec{a}_z} = \sqrt{2 \cdot \Delta z \frac{q \cdot U}{m \cdot d_{\text{grids}}}} = \sqrt{2 \cdot z_{\text{rel}} \cdot U \frac{q}{m}} \quad (4.6)$$

Which equates to 102 km s^{-1} for CO and 136 km s^{-1} for O-atoms. The velocity stays constant after the ions leave the electric field. The gating of the front MCP allows only a certain range of flight times t_z to be detected:

$$t_z = \frac{d_z}{\vec{v}_z} = d_z \cdot \sqrt{\frac{1}{2 \cdot z_{\text{rel}} \cdot U} \cdot \frac{m}{q}} \propto \sqrt{\frac{m}{q}} \quad (4.7)$$

with the total flight distance which is approximately equal to the length of the flight tube d_{tube} (see (3) in Figure 3.7):

$$d_z = \Delta z + d_{\text{tube}} \approx d_{\text{tube}} \quad (4.8)$$

Equation (4.7) shows how the MCP-Gate delay serves as a mass selector with $t_z \propto \sqrt{m/q}$. When comparing the theoretical values for the MCP-Gate delay with measurements $z_{\text{rel}} = 0.6$ can be determined. This means that the detected xy -slice is ionized at a z -position close to the center between the grids.

Assuming only single charged ions, the mass resolution is given by the ratio of t_z and the pulse width of the MCP gating pulse τ_{gate} :

$$\frac{m}{\Delta m} = \frac{t_z}{\tau_{\text{gate}}} = \frac{d_{\text{tube}}}{\tau_{\text{gate}}} \cdot \sqrt{\frac{1}{2 \cdot z_{\text{rel}} \cdot U}} \cdot \frac{m}{q} \quad (4.9)$$

Resolving $\Delta m \leq 1$ amu is possible by adjusting τ_{MCPGate} and the applied repeller voltage U .

4.2 Laser Delay

4.2.1 Density to flux conversion

In slice imaging the detected signal is proportional to the density of the desorbing molecules, but in kinetics the flux of the desorbing molecules is used. Therefore, the measured density $D(\theta, T_S)$ is converted to flux $\Phi(\theta, T_S)$ by multiplying it with the velocity of the corresponding molecule:

$$\Phi(\theta, T_S) = D(\theta, T_S) \cdot v_{xy} = D(\theta, T_S) \cdot \frac{d_{\text{Laser}}}{t_{\text{Laser}}} \quad (4.10)$$

with the laser delay t_{Laser} and the distance d_{Laser} between the desorption and detection laser.

In ion imaging, the images contain the information about the velocity. Velocity map imaging[59] is often applied to increase the velocity resolution. For the LID signal, the velocity is known from the slicing of the velocity distribution (see Section 3.6.1). The detected slice has almost constant velocity and is only broadened by the width of the detection laser focus in x -direction. The length of the detection laser focus in y -direction limits the desorption angle in the xy -plane to $< 20^\circ$ with respect to the surface normal, which renders the velocity difference between the center and the edges of the detected signal in y -direction to $< 5\%$.

4.2.2 Hyperthermal distributions

By varying t_{Laser} at a constant d_{Laser} different slices of the velocity distribution are sampled. Hence, a scan of the laser delay directly yields the TOF distribution of the LID flux, $\Phi(\theta, T_S)$, which can be converted to the velocity distribution and the kinetic energy distribution. To fit the TOF distributions, a hyperthermal distribution function is used:

$$\Phi(t)dt = 4\pi \left(\frac{m}{2\pi k_B T_S} \right)^{3/2} \frac{d_{\text{Laser}}^4}{t_{\text{Laser}}^5} \cdot \exp \left(\frac{-m(d_{\text{Laser}}/t_{\text{Laser}} - \Delta v)^2}{2k_B T_S} \right) dt \quad (4.11)$$

with the hyperthermal shift Δv . The function is set up so that for $\Delta v \rightarrow 0$ the hyperthermal distribution converts to the Maxwell-Boltzmann distribution.

By replacing $t_{\text{Laser}} = d_{\text{Laser}}/v$ and dt using the Jacobian:

$$\frac{dt}{dv} = \frac{d}{dv} \left(\frac{d_{\text{Laser}}}{v} \right) = \frac{d_{\text{Laser}}}{v^2} = \frac{t_{\text{Laser}}}{v} \quad (4.12)$$

the TOF distribution can be converted to the velocity distribution:

$$\Phi(v)dv = 4\pi \left(\frac{m}{2\pi k_B T} \right)^{3/2} v^3 \cdot \exp \left(\frac{-m(v - \Delta v)^2}{2k_B T} \right) dv. \quad (4.13)$$

Similarly, replacing $t = \sqrt{\frac{md_{\text{Laser}}^2}{2E}}$ and dt with the respective Jacobian:

$$\frac{dt}{dE} = \frac{d}{dE} \left(\sqrt{\frac{md_{\text{Laser}}^2}{2E}} \right) = \sqrt{\frac{md_{\text{Laser}}^2}{8E^3}} = \frac{d_{\text{Laser}}}{mv^3} = \frac{t}{mv^2} \quad (4.14)$$

yields the kinetic energy distribution:

$$\Phi(E)dE = \sqrt{\frac{1}{m\pi}} \left(\frac{2}{k_B T} \right)^{3/2} E \cdot \exp \left(\frac{-m \left(\sqrt{2E/m} - \Delta v \right)^2}{2k_B T} \right) dE. \quad (4.15)$$

4.3 Nozzle Delay

When performing kinetic desorption measurements, the aim is to obtain the kinetic trace, which is a recording of the desorbing flux as a function of time. This is achieved by varying the nozzle delay and recording the flux at different points in time before and after the surface was dosed by the MB pulse. In this section I will explain the conventional VRK method first and then the additions and differences of the LID-VRK method.

4.3.1 Velocity-resolved kinetics (VRK)

This technique has been developed in recent years by applying Ion imaging and VMI to surfaces to measure kinetics[61, 63]. The sample is held at an elevated T_S so that all molecules desorb and a clean surface is restored before the next molecular beam pulse arrives. This procedure ensures steady-state conditions in the low coverage limit. Variation of the time delay between the opening of the MB pulse and the detection laser pulse allows the recording of the time-dependent desorption flux, Φ_{TD} , i.e. the kinetic trace.

For first order reactions, the TD flux is given by:

$$\Phi_{\text{TD}}(\theta, T_S) = -\frac{d\theta}{dt} = k_D(T_S) \cdot \theta \quad (4.16)$$

with the rate constant k_D . Integration yields the solution of the differential equation:

$$\theta = \theta_0(t) \exp(-k_D(T_S) \cdot t) \quad (4.17)$$

which can be plugged into Equation (4.16):

$$\Phi_{\text{TD}}(\theta, T_S) = -\frac{d\theta}{dt} = k_D(T_S) \cdot \theta_0(t) \exp(-k_D(T_S)t) \quad (4.18)$$

The initial coverage, θ_0 , is deposited over a period of time with a MB pulse. Hence, $\theta_0(t)$ is a time-dependent distribution. This dosing function is modeled by the sum of two Gaussian functions:

$$\theta_0(t) = a_1 \cdot \exp \left(-\frac{(t - t_1 - t_0)^2}{w_1^2} \right) + a_2 \cdot \exp \left(-\frac{(t - t_2 - t_0)^2}{w_2^2} \right) \quad (4.19)$$

with the parameters: the amplitudes a_1 and a_2 , the widths w_1 and w_2 and the time shift t_1 and t_2 of each Gaussian. The whole function is shifted by t_0 which is the delay of the valve opening (see Section 5.2.1).

The equation for the flux (Equation (4.18)) contains two time-dependent functions, the dosing function θ_0 (Equation (4.19)) and the exponential decay (Equation (4.17)). The convolution of the two time-dependent functions is calculated in similar manner as Golibrzuch *et al.* [7]. The result of the convolution is used to fit the kinetic traces and extract the rate constant k_D .

$$\begin{aligned} \Phi_{\text{TD}} = \frac{\sqrt{\pi}k_D}{2} & \left[a_1 w_1 \exp\left(\frac{w_1^2 k_D^2}{4} - k_D(t - t_1 - t_0)\right) \operatorname{erfc}\left(\frac{w_1 k_D}{2} - \frac{t - t_1 - t_0}{w_1}\right) \right. \\ & \left. + a_2 w_2 \exp\left(\frac{w_2^2 k_D^2}{4} - k_D(t - t_2 - t_0)\right) \operatorname{erfc}\left(\frac{w_2 k_D}{2} - \frac{t - t_2 - t_0}{w_2}\right) \right] \quad (4.20) \end{aligned}$$

VRK is typically restricted to a relatively small temperature range, where the temporal width of the MB pulse is the limiting factor for high temperatures. The high temperature limit has been pushed higher by the improved design of the ELT nozzle, which enables very short MB pulses with large peak intensity. Equation (4.16) shows that the flux $\Phi_{\text{TD}}(\theta, T_S)$ is directly proportional to the rate constant $k_D(T_S)$, which is the limiting factor for low temperatures. The rate constant $k_D(T_S)$ decreases exponentially with decreasing temperature. This can be described with the Arrhenius equation:

$$k_D(T_S) = A \cdot \exp\left(\frac{-E_D}{k_B \cdot T_S}\right) \quad (4.21)$$

with the activation energy of desorption E_D and the Arrhenius-prefactor A . Therefore, the measured flux $F_{\text{TD}}(\theta, T_S)$ also decreases exponentially with decreasing temperature. Additionally, the TD signal often overlaps with the direct scattering component, which has to be taken into account.

4.3.2 LID-VRK

This new method expands on VRK by combining it with ultra-fast LID techniques[64] in order to measure thermal desorption kinetics. The LID-VRK method introduces a second laser beam pulse which illuminates the sample surface and induces the desorption process photochemically. Hence, the point in time when the detected molecules left the surface is very well-defined. The general idea is that instead of measuring the TD flux, LID directly probes the coverage θ that is left at the surface and has not desorbed yet. The measured LID flux $\Phi_{\text{LID}}(\theta, T_S)$ is then given by:

$$\Phi_{\text{LID}}(\theta, T_S) = k_{\text{LID}} \cdot \theta \quad (4.22)$$

which is very similar to Equation (4.16). The key difference is that the rate constant k_{LID} is not a function of T_S and only depend on the properties of the desorption laser pulse. The TD rate constant k_D is extracted from the data by inserting the solution of the first order TD kinetics (Equation (4.17)) into Equation (4.22) to describe the time-evolution of the coverage before the LID pulse. The resulting expression:

$$\Phi_{\text{LID}}(\theta, T_S) = -\frac{d\theta}{dt} = k_{\text{LID}} \cdot \theta_0(t) \exp(-k_D(T_S)t) \quad (4.23)$$

is solved as described in Section 4.3.1. The solution:

$$\begin{aligned} \Phi_{\text{LID}} = \frac{\sqrt{\pi}k_{\text{LID}}}{2} & \left[a_1 w_1 \exp\left(\frac{w_1^2 k_{\text{D}}^2}{4} - k_{\text{D}}(t - t_1 - t_0)\right) \operatorname{erfc}\left(\frac{w_1 k_{\text{D}}}{2} - \frac{t - t_1 - t_0}{w_1}\right) \right. \\ & \left. + a_2 w_2 \exp\left(\frac{w_2^2 k_{\text{D}}^2}{4} - k_{\text{D}}(t - t_2 - t_0)\right) \operatorname{erfc}\left(\frac{w_2 k_{\text{D}}}{2} - \frac{t - t_2 - t_0}{w_2}\right) \right] \quad (4.24) \end{aligned}$$

is used to fit the measured kinetic traces of the LID signal and extract the rate constant k_{D} . It differs from Equation (4.20) only by the replacement of k_{D} by k_{LID} in the prefactor. This seemingly small difference has a large impact on the temperature dependence of the flux because k_{LID} is not a function of T_{S} . This enables measurements of the desorption kinetics at much lower temperature than in conventional VRK experiments.

However, the low temperature limit is still restricted by $k_{\text{d}}(T_{\text{S}})$, but differently than in VRK: To ensure that the desorption conditions are in the low coverage limit, the nozzle repetition rate f_{RR} must be adjusted so that all molecules have desorbed before the next nozzle pulse arrives at the surface. Otherwise, the coverage will start to build up overtime and an equilibrium coverage is established. The deciding factor between the case of low coverage and steady-state coverage buildup is the relation between the modulation time $t_{\text{mod}} = f_{\text{RR}}^{-1}$ and the adsorption lifetime $\tau = k_{\text{D}}^{-1}(T_{\text{S}})$. Adjusting the repetition rate according to each T_{S} so that the relation is at least three:

$$\frac{t_{\text{mod}}}{\tau(T_{\text{S}})} = \frac{k_{\text{D}}(T_{\text{S}})}{f_{\text{RR}}} \geq 3 \quad (4.25)$$

ensures that the total coverage on the surface is below 5% of the initial coverage before the next MB pulse. With decreasing T_{S} and f_{RR} , the measurement time must increase to maintain the same signal-to-noise ratio. Hence, theoretically, the measurement of low temperature desorption kinetics is only limited by measuring time.

4.4 Repeller Delay

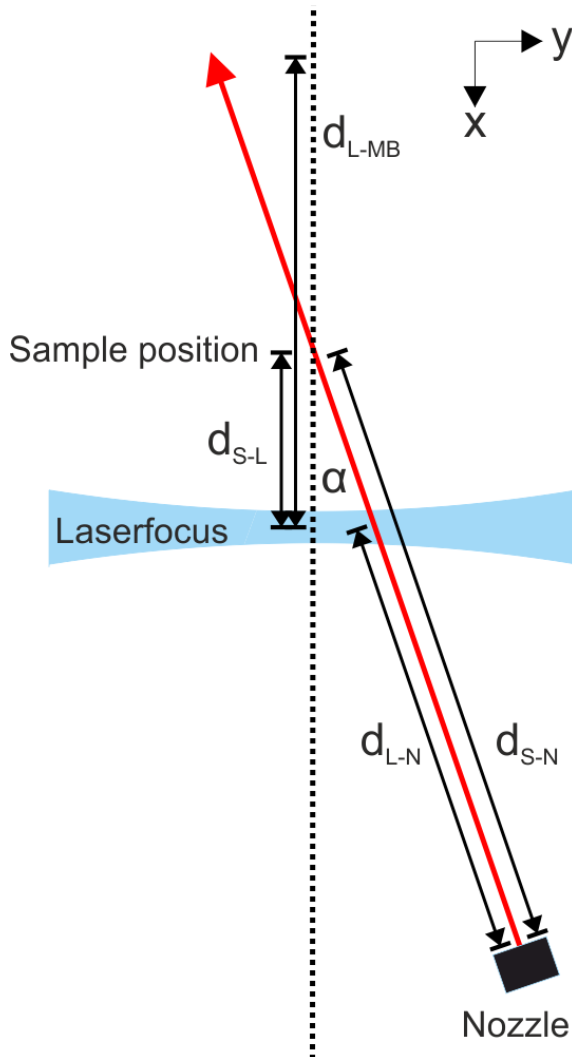


Figure 4.2: Sketch of the geometry of the MB pulse trajectory without the sample being in position. The red arrow is the MB trajectory and the dotted line marks the surface normal. The distances from the sample position to the nozzle, $d_{S-N} = 375$ mm, and to the detection laser focus, $d_{S-L} = 8-10$ mm, are known. The distances from the laser focus to the nozzle (d_{L-N}) and to the detected signal (d_{L-MB}) are calculated.

The repeller pulse can be either be activated synced with the detection laser or delayed. The delayed extraction allows the ions to travel further in the xy -plane with \vec{v}_{xy} inside the field-free region. This improves the signal-to-noise ratio and the contrast between LID and TD signal. Delayed extraction reduces the width of the whole ionized slice in z -direction, which reduces noise from background gas because it is isotropic. Since the TD flux originates from the whole surface area, a large range of trajectories with a velocity component in z -direction is ionized. These trajectories can be gated away by the MCP and are not detected if the extraction is delayed. The acLID, on the other hand, originates only from the laser beam spot, which is very narrow in z -direction. Therefore, the ionized LID flux has only little velocity component in z -direction and therefore the majority is detected. Another

advantage of prolonging the total TOF_{xy} is to separate the thermally desorbing flux from the LID flux in space. The cause of the separation is the large difference in velocity, which results in a different distance from the surface on the image. This effect is enlarged by a longer total TOF_{xy} (see Figure 4.4).

Scanning of the repeller delay is useful to determine the opening delay of the valve t_0 (see Section 3.4) in MB characterization experiments which are performed without the sample present. Figure 4.2 shows the geometry of this experiment for the PGV nozzle which is mirror-inverted identical to the geometry with the ELT nozzle. The sample position is used here only as a reference point, because it marks the intersection of both the MB pulses. The MB pulse is directly ionized by the detection laser after a specific nozzle delay, t_{MB} , which slices the velocity distribution by only ionizing particles which have taken this time to travel the distance from the nozzle to the laser focus $d_{\text{L-N}}$. To calculate $d_{\text{L-N}}$, the known distances from the sample to the nozzle, $d_{\text{S-N}} = 375$ mm, and from the sample to the laser focus, $d_{\text{S-L}} = 8 - 10$ mm, are used:

$$d_{\text{L-N}} = d_{\text{S-N}} - \frac{d_{\text{S-L}}}{\cos \alpha} \quad (4.26)$$

The velocity of the selected slice along the MB propagation direction is calculated with:

$$v_{\text{MB}} = \frac{d_{\text{L-N}}}{t_{\text{MB}} - t_0} \quad (4.27)$$

To obtain t_0 , the velocity is measured by scanning the repeller delay allowing the ions to travel some distance in the x-y plane after ionization. The experiments yield the distance of the MB pulse from the laser focus $d_{\text{L-MB}}$ in x -direction, which is plotted against the repeller delay. The slope of a linear fit directly yields the velocity in x -direction \vec{v}_x , which can be transformed into \vec{v}_{MB} :

$$\vec{v}_{\text{MB}} = \frac{\vec{v}_x}{\cos \alpha} \quad (4.28)$$

Inserting the velocity from Equation (4.28) into Equation (4.27) yields t_0 :

$$t_0 = t_{\text{MB}} - \frac{d_{\text{L-N}} \cdot \cos \alpha}{\vec{v}_{\text{MB}}} \quad (4.29)$$

4.5 REMPI scans

CO was ionized using the (2+1)REMPI scheme via the $B^1\Sigma^+$ -state. The strongest transitions are the Q-bands of (0,0) transition at 230.105 nm and (1,1) transition at 230.265 nm which have very similar Franck-Condon factors near unity[65]. When using linear polarized light, the intensity of the Q-bands is amplified by a factor of at least 200 compared to circular polarized light[55] which makes the O- and S-branches very weak in comparison. Higher vibrational states in the $B^1\Sigma^+$ -states are known to lead to pre-dissociation[65] and could not be observed.

The REMPI spectra are fitted by the sum of Lorentzian peak functions for $J = 0 - 50$:

$$\Phi(\lambda) = \sum_J \frac{A}{1 + ((\lambda - \lambda_J)/w)^2} \cdot 2(J + 1) \exp\left(\frac{-E_{\text{rot}}}{k_B T_{\text{rot}}}\right) \quad (4.30)$$

with an amplitudes factor A , the calculated transition wavelengths of each J-state λ_J [66], the full-width at half-maximum (FWHM) $2w$ and the rotational Energy E_{rot} which is given by:

$$E_{\text{rot}} = B_e J(J + 1) - D_e J^2(J + 1)^2 \quad (4.31)$$

with the rotational constants B_e and D_e of the B-state[66]. The rotational temperature T_{rot} is obtained as parameter from the fit. The vibrational temperature T_{vib} is calculated from integrating over the whole spectrum and comparing $v = 0$ to $v = 1$.

$$\frac{N_v}{N_0} = \exp\left(\frac{-E_v}{k_B T_{\text{vib}}}\right) \quad (4.32)$$

Oxygen atoms were detected with (2+1)REMPI in the 3P_2 state. The $3p^3P_J \leftarrow 2p^3P_J$ transition single-photon wavelengths are 226.232 nm, 226.065 nm and 225.657 nm for 3P_0 , 3P_1 and 3P_2 , respectively.

4.6 Surface diffusion

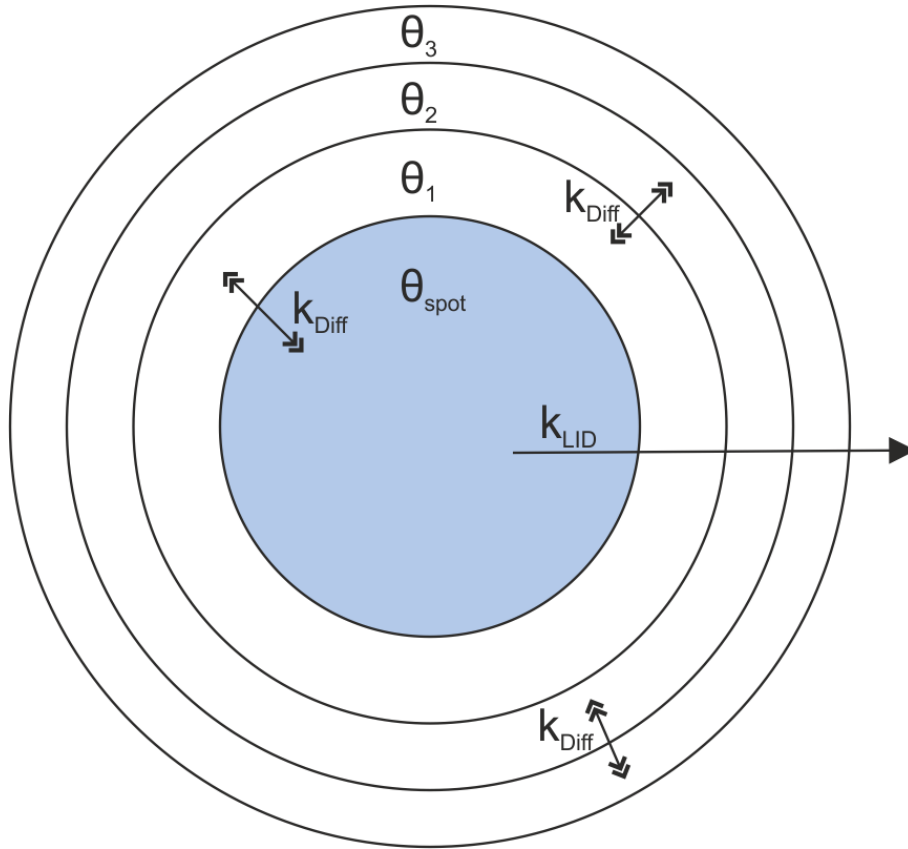


Figure 4.3: Sketch of diffusion model. LID only occurs inside the desorption laser spot, which is colored in light blue. Surface diffusion occurs between each ring and between the laser spot and the first ring with the same diffusion rate. The concentration gradient points for the outside towards the center.

To determine the LID rate constant k_{LID} , the LID flux after dosing was monitored for a period of time. The repetition rate f_{RR} of the experiment was tuned to the rate of the camera (5 Hz) to acquire images with the best temporal resolution of one laser shot per image. The decay is biexponential because of the diffusion of CO on platinum[39]. After the desorption laser pulse has reduced the coverage inside the laser spot, CO molecules from just outside diffuse into the laser spot and replenish the desorbed coverage partially[67]. Subsequently, CO molecules from further away diffuse towards the outside of the laser spot and so forth. A radial coverage gradient is established, with a net flux from the edge of the sample towards the center of the laser spot. Figure 4.3 shows a sketch of this simple model: The laser spot is assumed to be circular with the radius, r_{spot} , and the outside of the laser spot was modeled as rings with equal surface area as the laser spot. The Gaussian shape of the laser pulse is neglected for direct comparison to experiment because the experiment cannot distinguish the origin positions of desorbing molecules. Only the LID flux

averaged over the laser spot area is observed. The kinetic rate equations:

$$\begin{aligned}
 \frac{d\theta_{\text{spot}}}{dt} &= -k_{\text{LID}}\theta_{\text{spot}} + k_{\text{Diff}}\theta_1 - k_{\text{Diff}}\theta_{\text{spot}} \\
 \frac{d\theta_1}{dt} &= -2 \cdot k_{\text{Diff}}\theta_1 + k_{\text{Diff}}\theta_{\text{spot}} + k_{\text{Diff}}\theta_2 \\
 \frac{d\theta_2}{dt} &= -2 \cdot k_{\text{Diff}}\theta_2 + k_{\text{Diff}}\theta_1 + k_{\text{Diff}}\theta_3 \\
 &\dots
 \end{aligned} \tag{4.33}$$

are solved numerically with the Euler method, and the time is expressed in units of number of laser shots. The numerical solution is fitted to the data, yielding the two fitting parameters k_{LID} and k_{Diff} . The obtained diffusion rate possibly consists of thermal diffusion and laser-induced diffusion[51, 68]. TD can be included in the model by introducing an additional desorption path for each position inside and outside the laser spot, but this can be neglected for room temperature measurements.

4.7 Image Analysis

Individual images are not stored separately, but they are summed up, and only the summed image is stored. The reason for this is just to reduce the amount of data stored since the size of each image is 9.2 MByte which does not scale up with the number of summed images N_{sum} . When scanning a delay, the number of summed images, N_{sum} , is typically between 50 and 200 images for each data point of the scan. All recorded images are stored as raw data, and they consist of a matrix with the x and y pixel coordinates with the brightness of the pixel as a value. For analysis, the images are imported into Python or MATLAB(R2021b). Generally, two methods for the analysis of the images were used: The simplest one is choosing a region of interest (ROI) and summing up all brightness values of the pixels inside the ROI. For the analysis, one ROI is placed onto the signal of interest and another one is placed next to the signal and is used for background subtraction. The second method is taking a profile in x -direction by summing up all the brightness values in the y -dimension for each x -position. The signal of each image is normalized by dividing by the number of laser shots, N_{shots} , which is given by:

$$N_{\text{shots}} = N_{\text{sum}} \cdot f_{\text{RR}} \cdot t_{\text{exposure}} \quad (4.34)$$

with the camera exposure time t_{exposure} and the repetition rate of the experiment f_{RR} .

If necessary, a correction for background gas signal is applied by subtraction of a polynomial fit from the profile. Typical images and profiles are shown in Figure 4.4 which incorporates the LID signal and the TD signal. The LID signal is identified by the distinctive low width along the x -direction and the large distance from the surface, which is due to the high velocity and the velocity slicing. On the other hand, the TD signal has a broad distribution in all directions, is closer to the surface which means slower velocities and has a large dependence on T_{S} . This separation on the image allows the LID signal to be analyzed with minimal interference of the TD signal. Contributions of direct scattering are also not expected since they overlap with the TD signal.

At 573 K the TD signal is not observed, while the LID signal is very strong due to the high coverage. The profile is fitted by a single Gaussian function:

$$g(x) = A \cdot \exp\left(-\frac{(x - x_0)^2}{2w^2}\right) \quad (4.35)$$

which yield the center position x_0 , amplitude A and width w from which the FWHM is calculated:

$$FWHM = 2\sqrt{2 \ln 2} \cdot w \quad (4.36)$$

From the Gaussian-fit parameters the integral of the Gaussian is given by:

$$I(g) = \int_{-\infty}^{\infty} g(x) dx = \sqrt{2\pi} \cdot w \cdot A \quad (4.37)$$

which is proportional to the density of molecules that were desorbed.

At 693 K, the TD signal is observed and partially overlaps with the LID signal. Therefore, two Gaussian functions (Equation (4.35)) are used to fit both the TD signal and the LID signal together.

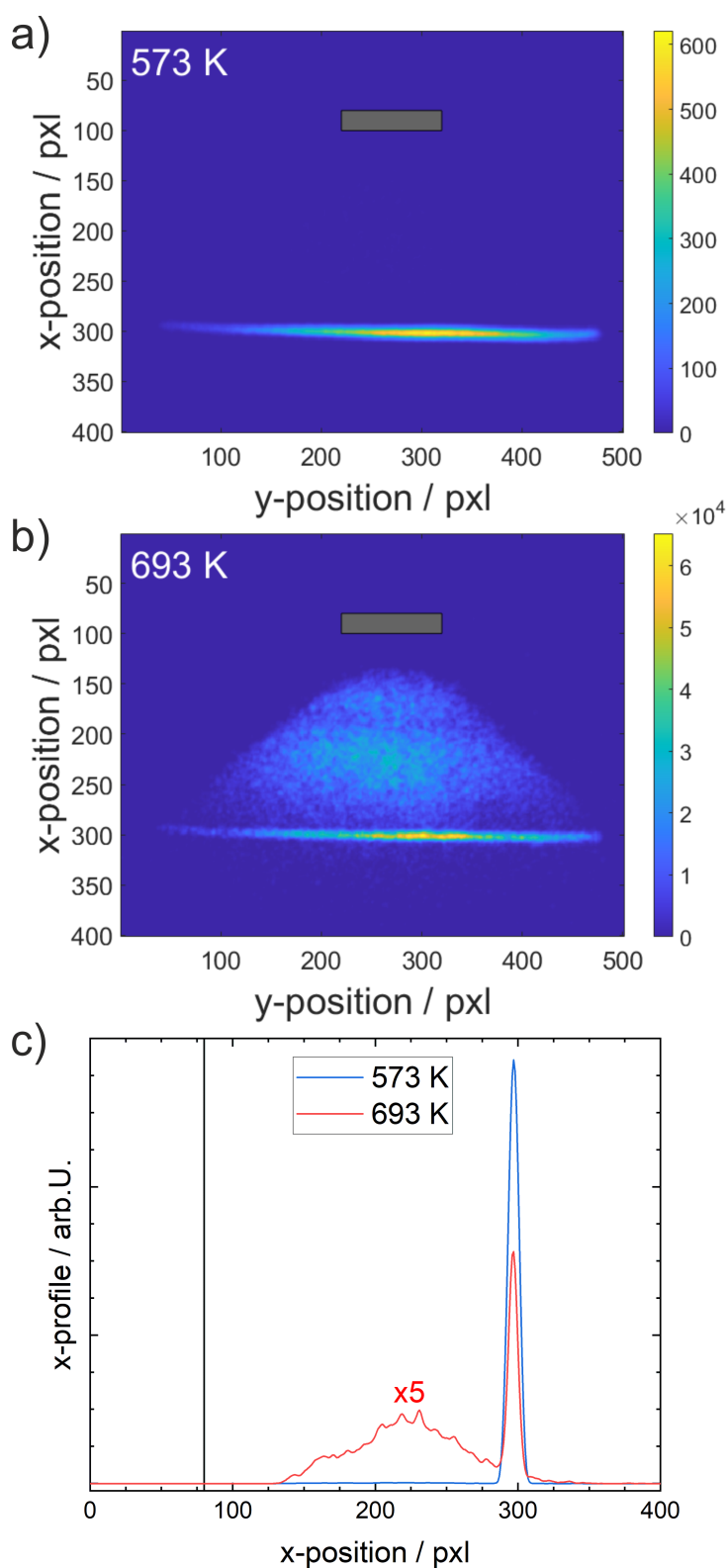


Figure 4.4: Example images of CO LID from Pt(332). Panel (a) shows the LID signal at 573 K and panel (b) at 693 K. The position and size of the sample is illustrated by the gray bar in the top of the image. Panel (c) shows the resulting profiles along the x -direction for both temperatures, with the high temperature profile scaled up by a factor of 5 for better comparison. The vertical black line represents the position of the sample.

Chapter 5

Results

5.1 Laser power correction

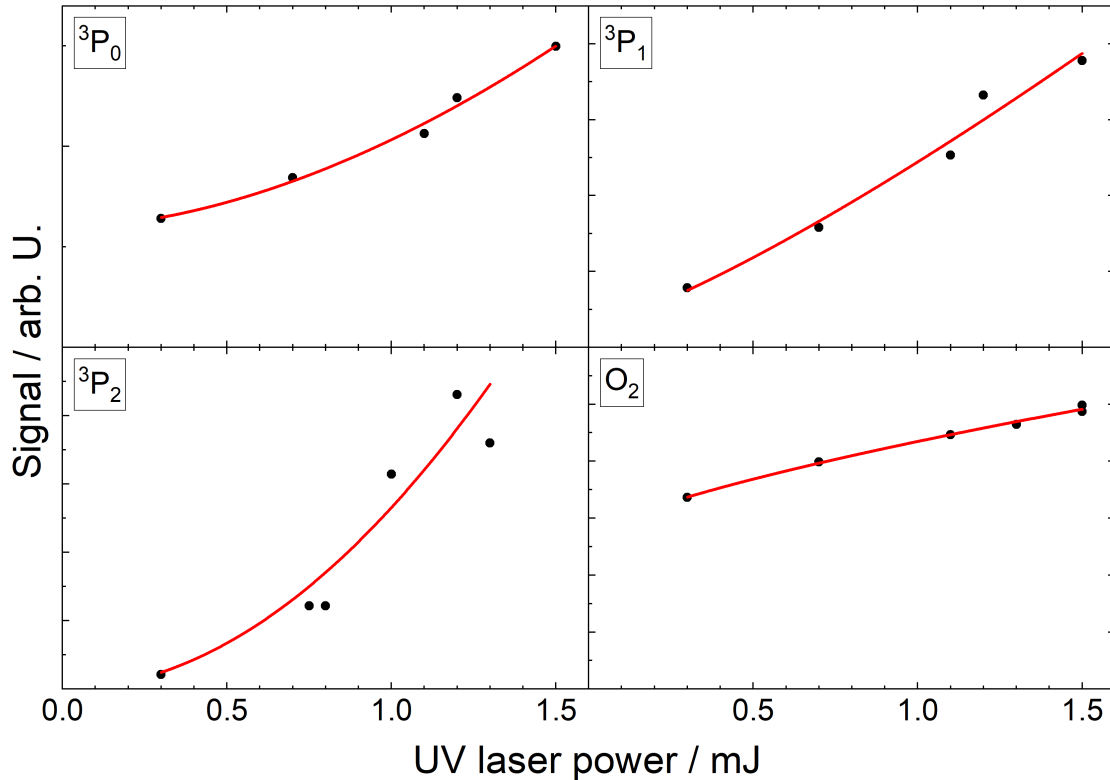


Figure 5.1: Detection laser power law of $4 \cdot 10^{-7}$ mbar O_2 background gas. The data points are ROI intensities and the red lines are power law fits. Each panel represents an atomic state or molecular oxygen.

To compensate the relatively large fluctuations of the REMPI laser power (see Section 3.5.2), the data was corrected by dividing by the laser power. This allows the comparison of data which were measured with a different laser power. The power law factor k was determined by measuring the LID flux Φ as a function of the UV laser power P and fitting it with a power law:

$$\Phi \propto P_{UV}^k \quad (5.1)$$

Figure 5.1 shows the power law measurements for oxygen, which is partially dissociated by the detection laser pulse. The dissociation of oxygen will be examined in Section 5.4.1. All three states of the atomic ground state ^3P are observed in addition to molecular oxygen. State selection of the atomic oxygen is achieved by tuning the detection laser to the respective wavelength, and the molecular oxygen is separated by mass selection via the MCP gate delay and ionized non-resonantly at the wavelength of the $^3\text{P}_2$ transition. For atomic oxygen the scaling power factors are fitted to 1.8 ± 0.4 , 1.2 ± 0.6 and 2.0 ± 0.5 for $^3\text{P}_0$, $^3\text{P}_1$ and $^3\text{P}_2$, respectively. The average value of 1.67 agree well with the value for a saturated (2+1)REMPI process of 3/2[69]. The slightly higher value might reflect the fact that the O-atoms are created by photo-dissociation of O_2 prior to the REMPI process. For molecular oxygen, the measured scaling power factor is only 0.7 ± 0.2 (see bottom right panel of Figure 5.1).

5.2 Molecular beam characterization

The MB is characterized by ionizing and detecting the CO MB beam without the sample present. At the wavelength of the $B^1\Sigma_g^+ \leftarrow X^1\Sigma_g^+(1,1)$ Q-head, no signal of the MB pulse could be observed. Hence, the MB characterization measurements utilize only the $B^1\Sigma_g^+ \leftarrow X^1\Sigma_g^+(0,0)$ Q-head wavelength. Table 5.1 summarizes the obtained MB characteristics of the two nozzles. Because of the large distance between nozzle and surface, $d_{\text{S-N}} = 375$ mm, the opening of the nozzle does not cause a measurable pressure rise in the main chamber. Hence, the dose was estimated with the pressure rise in the source chamber and $d_{\text{S-N}}$.

	PGV nozzle	ELT nozzle
$t_{\text{open}} / \mu\text{s}$	220	20
FWHM / μs	380	135
$\hat{v} / \text{m s}^{-1}$	500	620
$t_0 / \mu\text{s}$	260	150
$T_{\text{Trans}} / \text{K}$	48	7.7
$T_{\text{Rot}} / \text{K}$	79	82

Table 5.1: MB characteristics with pure CO. Comparing the results of the two different nozzles for the suitable opening durations: FWHM, most probable velocity, opening time, dose and rotational temperature.

5.2.1 Opening delay

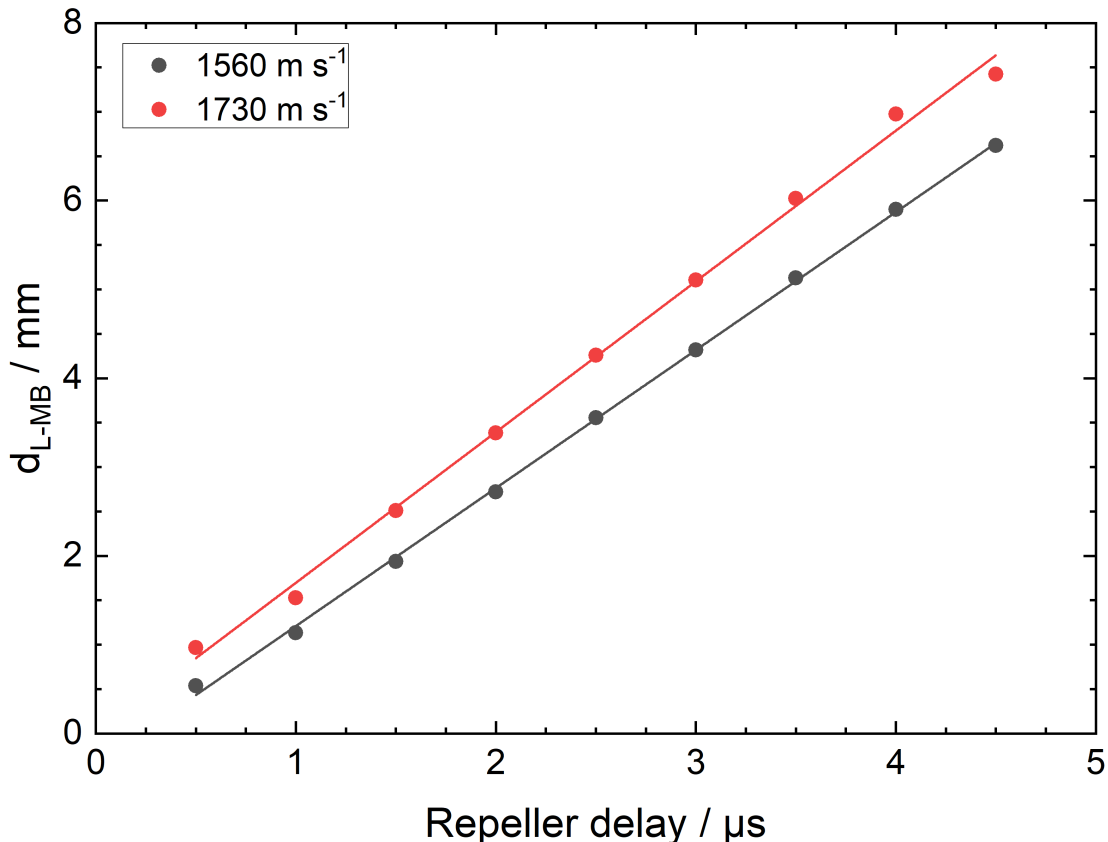


Figure 5.2: Distance of the MB pulse from the laser focus along the x-direction, d_{L-MB} , after ionization and delaying the repeller pulse. The PGVnozzle is used with a seeded beam of 2.5% CO in helium. The lines are linear fits to the data for two different velocity slices.

The method to obtain the opening delay of the nozzles was explained in Section 4.4. The distance between the laser focus and the detected MB pulse is plotted against the repeller delay in Figure 5.2. The resulting values for t_0 are $360 \pm 60 \mu\text{s}$ and $150 \pm 10 \mu\text{s}$ for the PGV and ELT nozzle, respectively.

5.2.2 opening duration

To find the optimal opening duration of both nozzles, the arrival time distribution of the MB pulse was measured for several values of t_{open} . The results are shown in Figure 5.3, for the PGV nozzle in the top panel and the ELT nozzle in the bottom panel. They were fitted with a single Gaussian and the fit parameters are plotted in Figure 5.4 against the opening duration. The amount of gas per pulse correlates with the integral in panel (a), which increases linearly. For the ELT nozzle, the integral saturates above $t_{\text{open}} = 22 \mu\text{s}$, which indicates collisions in the MB beam. Another indication for this is that the arrival time distribution of $t_{\text{open}} = 24 \mu\text{s}$ in the bottom panel of Figure 5.3 appears like two different peaks. For the PGV nozzle, this limit has not been reached yet at $t_{\text{open}} = 300 \mu\text{s}$, but probably would occur at longer opening durations. The most probable MB beam velocities, which

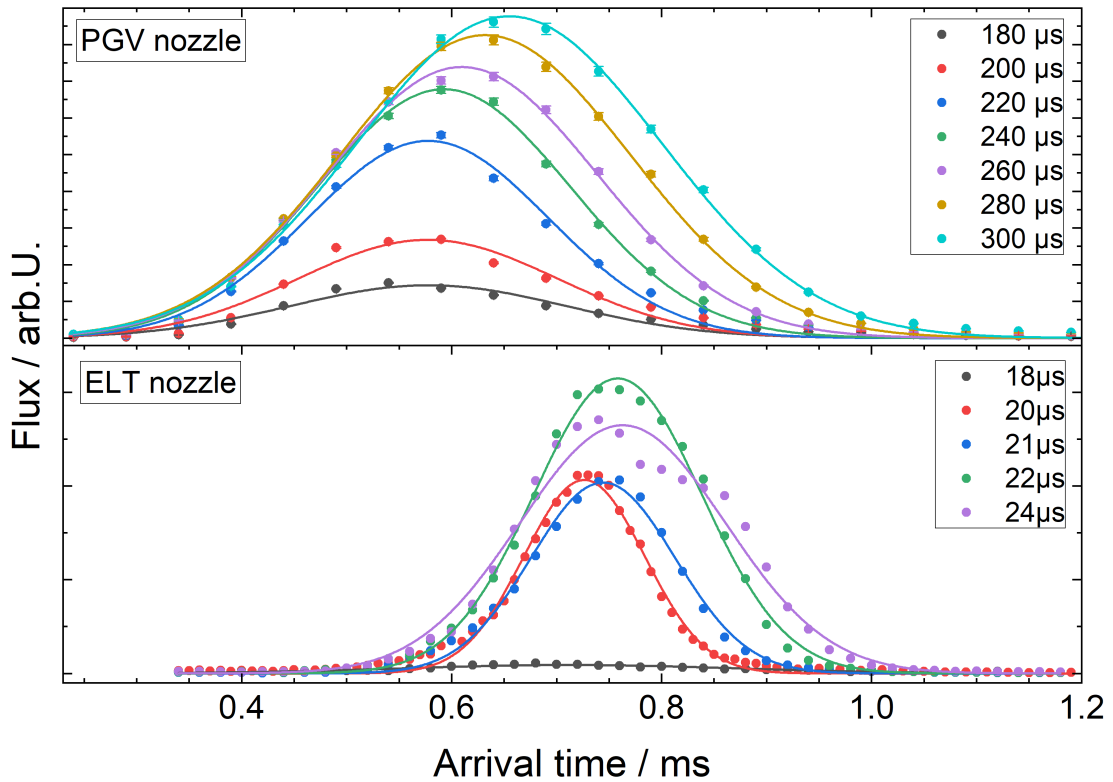


Figure 5.3: Arrival time distribution of the incident MB pulse. The top panel shows the results of the PGV nozzle for values of the opening duration from $180\ \mu\text{s}$ to $300\ \mu\text{s}$. The bottom panel shows the results of the ELT nozzle with an opening duration from $18\ \mu\text{s}$ to $24\ \mu\text{s}$. The lines are single Gaussian fits to the data. Both nozzles were operated with 2 bar of pure CO.

are plotted in panel (b) of Figure 5.4, are constant at short opening duration. This indicates that t_{open} is too short, and the valve does not open fully. For longer opening duration, the velocity decreases linearly due to more molecules passing through the valve shortly after the main pulse. Hence, the velocity distribution of the pulse broadens asymmetrically and shifts towards lower velocity. This broadening and shift is already apparent in the arrival distributions in Figure 5.3. The same broadening is displayed in panel (c) of Figure 5.4. For both nozzles, there clearly is an optimal opening duration at the minimum FWHM which coincides with the maximum t_{open} before the velocity decline. The optimal opening durations are $20\ \mu\text{s}$ and $220\ \mu\text{s}$ for the ELT and the PGV nozzle, respectively.

In comparison, the ELT nozzle operates with a much shorter opening duration, produces pulses with a shorter FWHM and a slightly lower velocity compared to the PGV nozzle.

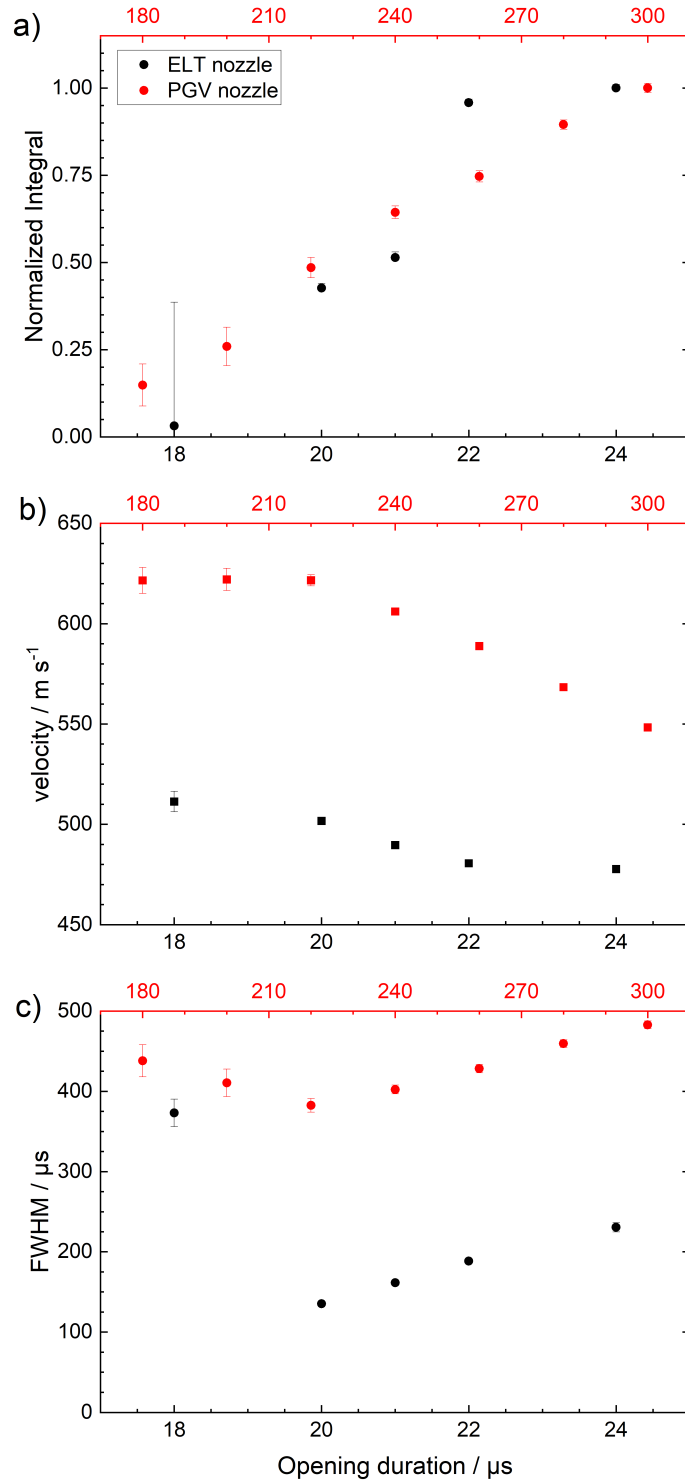


Figure 5.4: Parameters obtained from the Gaussian fits in Figure 5.3 with several opening durations. The ELT nozzle is colored in black corresponding to the bottom axis and the PGV nozzle is colored in red corresponding to the top axis. Panel (a) shows the integrals, which were normalized to the maximum value for comparison. Panel (b) shows the most probable velocity and panel (c) shows the FWHM.

5.2.3 Translational temperature

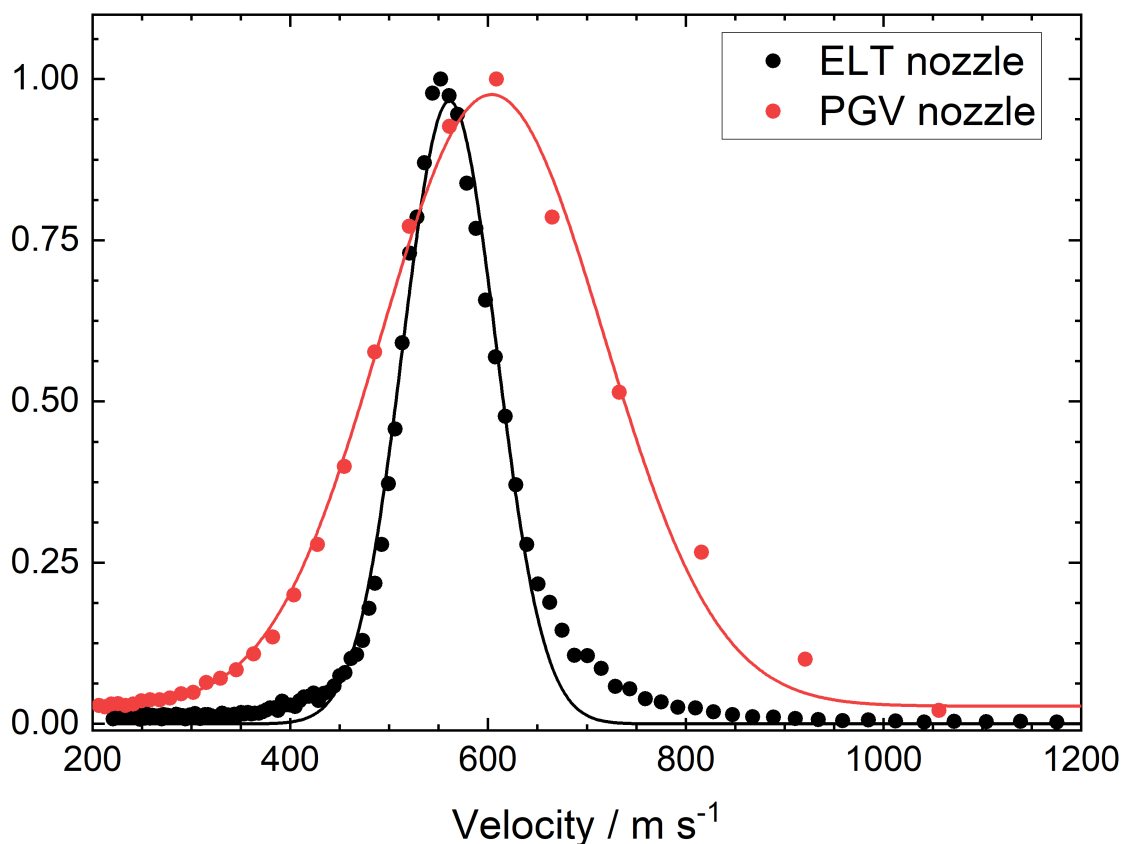


Figure 5.5: Normalized velocity distributions of the ELT nozzle (black) and the PGV nozzle (red). The opening duration was set to the respective optimal time. Both nozzles were operated with 2 bar of pure CO. The lines are hyperthermal distribution fits (Equation (4.13)).

To obtain the translational temperature of the MB pulses, The velocity distributions, with the optimal opening duration, are shown in Figure 5.5. They are hyperthermal because of the MB expansion acceleration, therefore they were fitted with the hyperthermal distribution function (Equation (4.13)). They fit the data reasonably well, despite some deviates in the high velocity tail. The resulting translational temperatures are 7.7 ± 0.3 K and 48 ± 3 K for the ELT and the PGV nozzle, respectively.

5.2.4 Rotational temperature

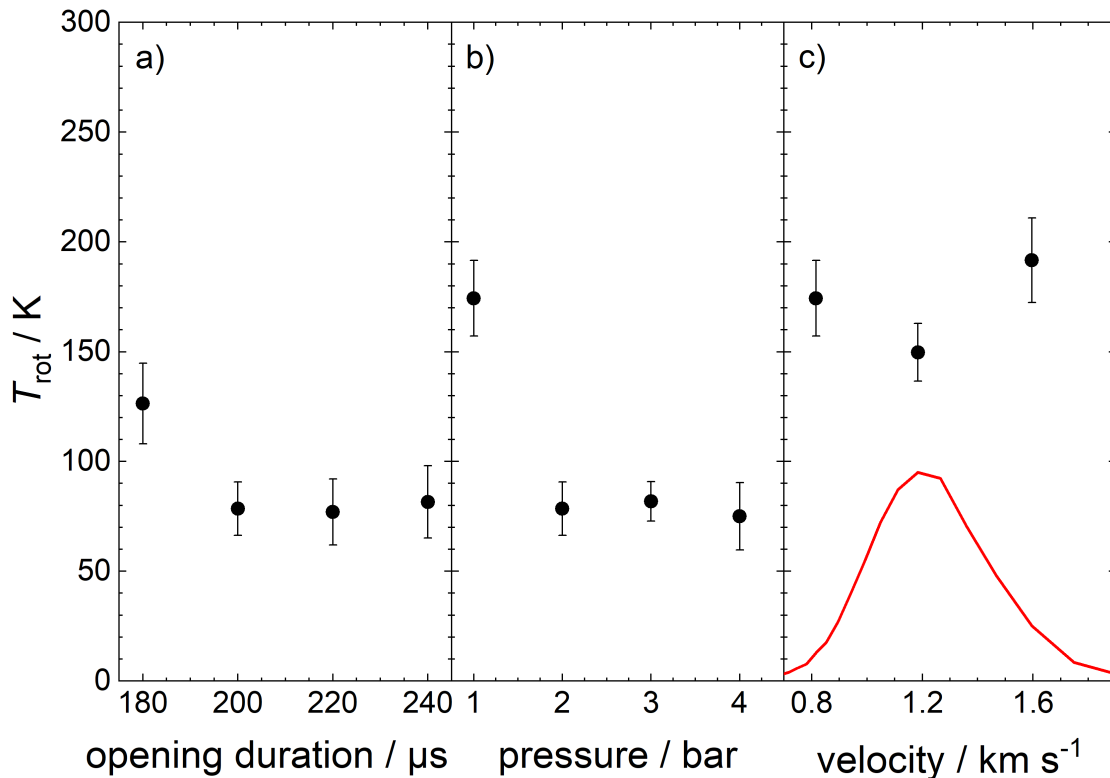


Figure 5.6: Rotational temperatures of the incident MB as a function of the nozzle parameters. Panel (a) shows the dependence on the opening duration, panel (b) on the backing pressure and panel (c) shows the results for different velocity slices with $p = 1$ bar. The velocity distribution is shown as a red line for comparison. The PGV nozzle was used with 7.5% CO seeded in helium.

The rotational temperature T_{rot} of the MB pulse was determined under various conditions to find the optimal parameters for the nozzle. The results in Figure 5.6 show that the rotational cooling is suboptimal, but T_{rot} is stable under most conditions. The rotational temperature increases if the opening time is too short (see panel (a)) or the operation pressure is too low (see panel (b)). Panel (c) shows that T_{rot} is constant within the error bars over the whole velocity distribution. The best rotational temperatures are 88 ± 4 and 79 ± 3 for the ELT and the PGV nozzle, respectively.

5.3 CO on platinum

The main system that was studied is the CO desorption from Pt(332). For comparison, the kinetic measurements were repeated on Pt(111) to study the effect of steps. The desorption of CO from platinum should be a good benchmark system for the LID-VRK method.

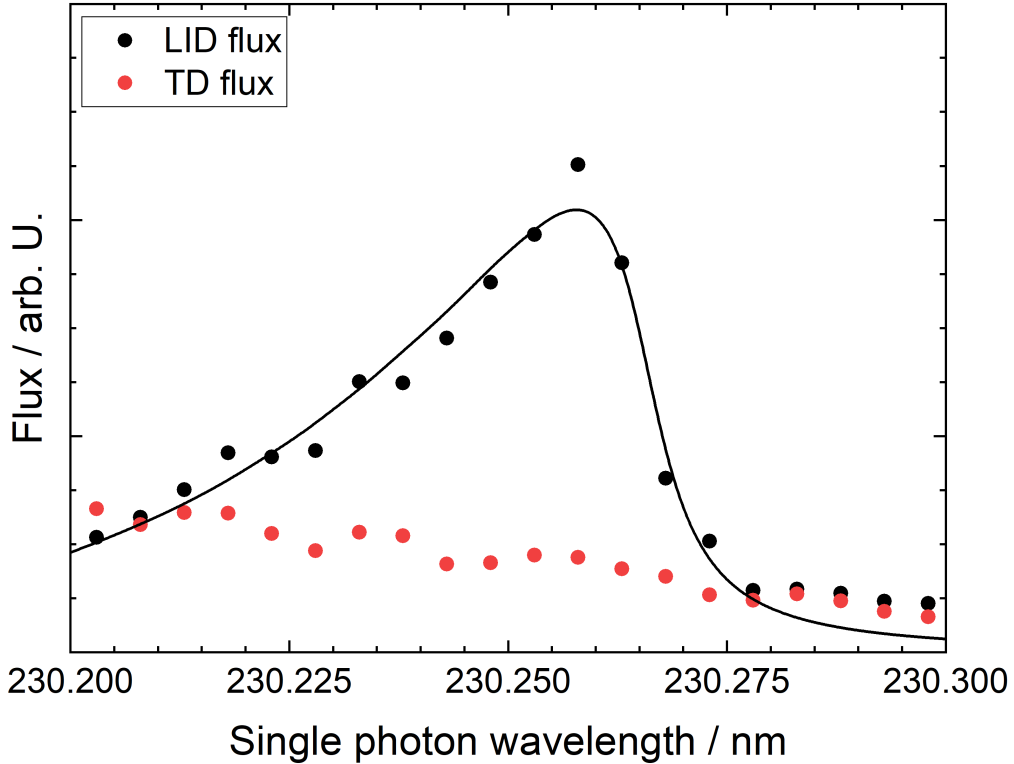


Figure 5.7: REMPI scans of the $B^1\Sigma_g^+ \leftarrow X^1\Sigma_g^+(1,1)$ Q-band of the CO in the LID flux (black dots) and in the TD flux (red dots). The Pt(332) surface was held at $T_S = 623$ K. The black line is the fit to the LID flux according to Equation (4.30). The TD flux is suppressed by delaying the extraction by $2.5 \mu\text{s}$.

Figure 5.7 compares the LID flux with the TD flux at the wavelength of the $B^1\Sigma_g^+ \leftarrow X^1\Sigma_g^+(1,1)$ Q-band. The TD flux is suppressed by using delayed extraction, which leads to good contrast. Unless stated otherwise, the wavelength of the $B^1\Sigma_g^+ \leftarrow X^1\Sigma_g^+(1,1)$ Q-head was chosen for the following measurements.

5.3.1 CO dissociation

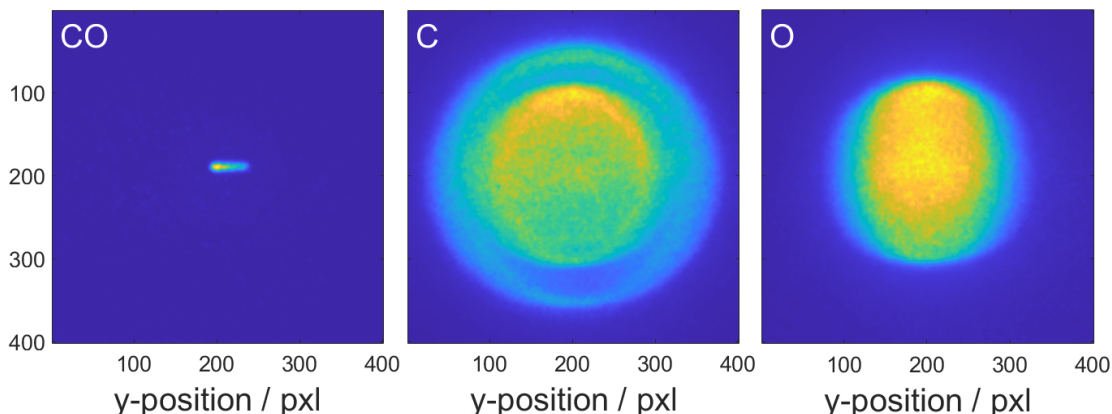


Figure 5.8: Raw images of CO and its fragments, C and O, in the incident MB beam. The CO is dissociated by the UV REMPI laser.

Studies of CO photo-dissociation have been done extensively[70, 71, 72]. CO fragments were found in the desorbing flux with m/q matching C^+ and O^+ ions when using the REMPI detection laser. Figure 5.8 shows the raw images of the CO MB beam and the dissociation fragments. The large area of the C^+ and O^+ fragments in the images in show a high kinetic energy release from the dissociation. Panel (a) in Figure 5.9 shows the MCP gate scan of the incidence MB beam. Three peaks were found, which can be assigned to C, O, and CO using Equation (4.7). The values of the respective MCP gate fit very well to masses of 12, 16 and 28 amu, respectively. The signal of both fragments clearly shows resonance with the CO $B^1\Sigma_g^+ \leftarrow X^1\Sigma_g^+(0,0)$ Q-band, as shown in panel (b). The signal of both fragments scales almost linearly with the REMPI laser power, which is apparent from panel (c). Panel (d) shows the branching ratio of the fragments, depicting which fragment is ionized in the dissociation process. At low laser power, the dissociation preferably leads to O^+ ions and neutral C fragments with the ratio of 3:1. With higher laser power, this preference diminishes, and the fraction approaches a ratio of 1:1.

No evidence for fragmentation was found when using the non-resonant MPI detection laser. This analysis clearly shows that the origin of the observed dissociation is the CO REMPI process[65] in the gas phase and not the LID process on the surface.

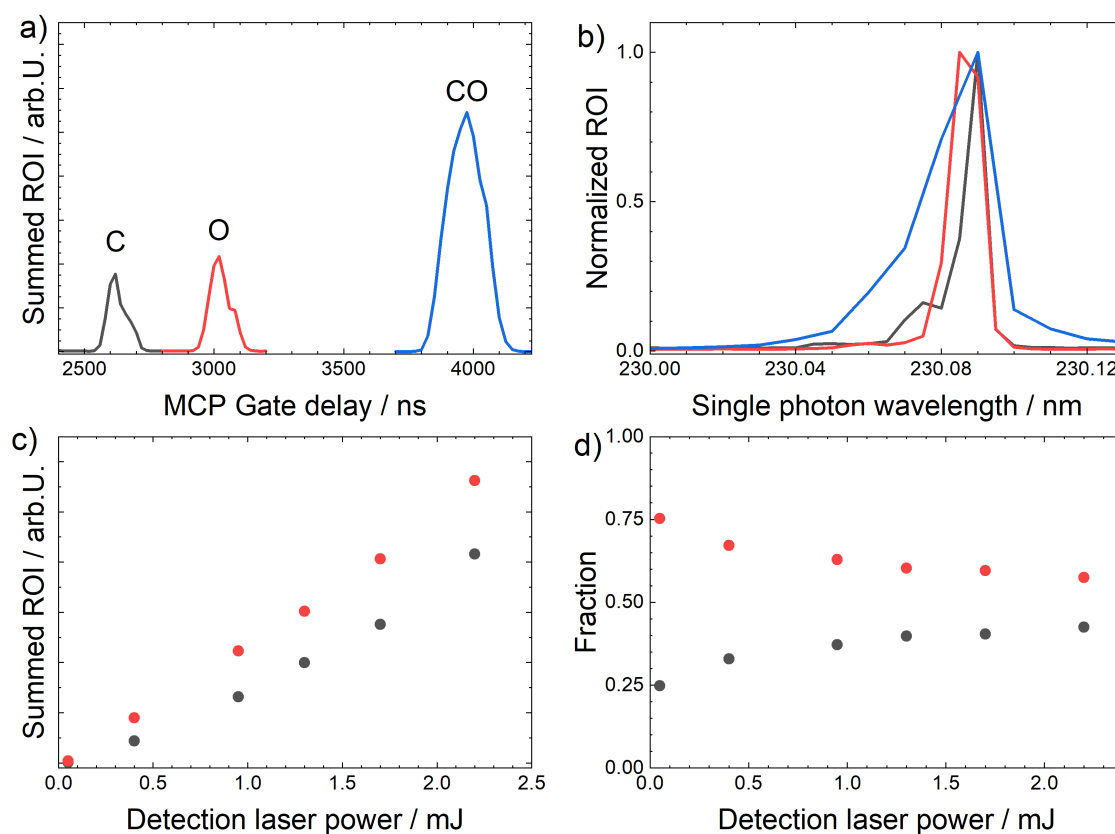


Figure 5.9: Overview of the observed CO dissociation: Panel (a) shows the MCP gate scan of CO and its fragments, panel (b) shows the corresponding normalized REMPI spectra, panel (c) shows the dependence of the fragmentation on the detection laser power and panel (d) shows the fraction of C and O in the detected fragments. C fragments are always drawn in black, O fragments in red and CO molecules in blue. The measurements involved only the incident MB pulse.

5.3.2 Adsorption of CO

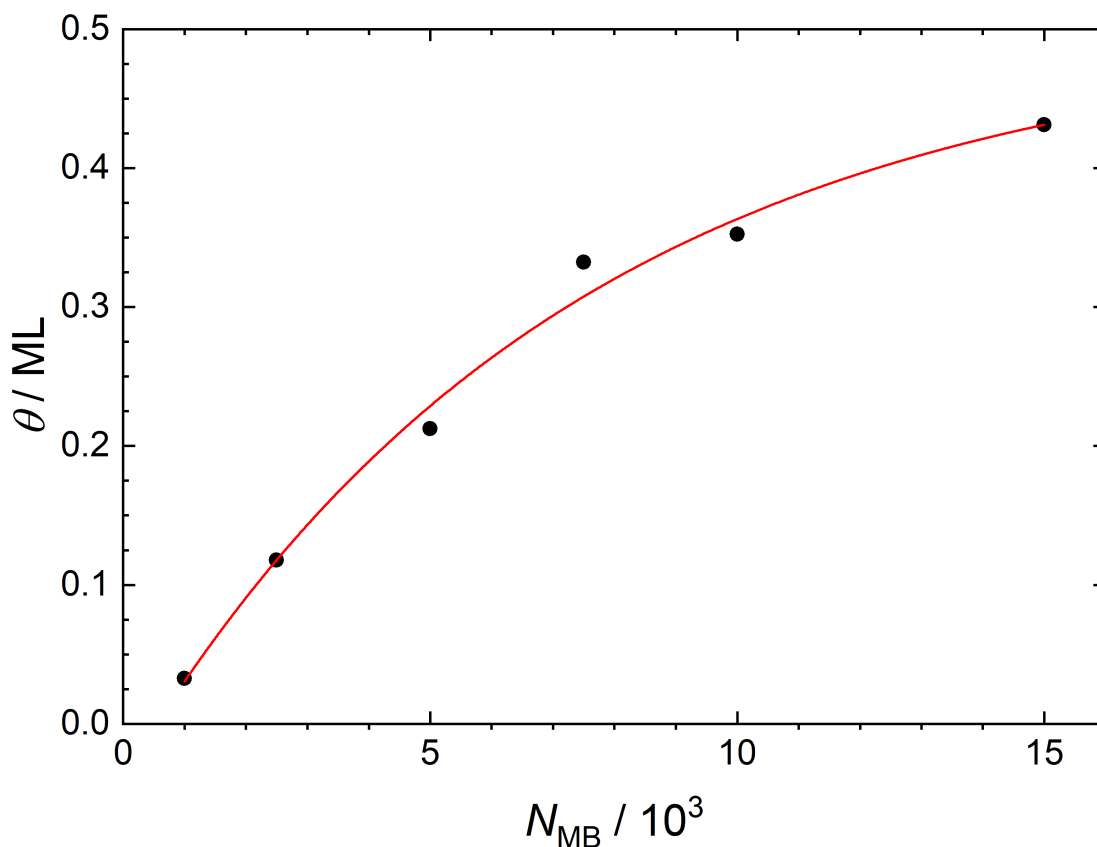


Figure 5.10: Pt(111) Adsorption curve measured by MB dosing at a surface temperature of 300 K. The data points correspond to the measured initial LID flux for doses from 2500 to 15000 MB pulses. The red line is the asymptotic fit to the data. The LID flux is calibrated to the coverage by assigning the asymptotic value to a coverage of 0.5 ML.

To quantify the coverage that is dosed with each MB pulse, the sample was dosed with a set number of pulses of a pure CO beam. Then the sample was exposed to the desorption laser and the decay of the LID flux was recorded for each laser shot. Afterwards, the sample was annealed to a high temperature to remove any residual CO before dosing again. This was repeated from 2500 up to 15000 MB pulses. The initial LID flux of each measurement is proportional to the coverage that was dosed. In Figure 5.10 the initial coverage is plotted against the number of MB pulses and fitted with an asymptotic fit function. The asymptotic value was assigned to the maximum coverage of 0.5 ML and the LID flux was scaled accordingly.

Adsorption isotherms were measured under steady state conditions with LID and are shown in the top panel of Figure 5.11. The sample is held at a constant temperature and is dosed with a constant pressure of CO. The repetition rate of the desorption laser and the detection was reduced to 5 Hz. This allows the surface to equilibrate with the gas phase after the equilibrium is disturbed by the LID. Assuming that the equilibrium is reestablished in the 200 ms before each laser shot, the LID flux is proportional to the steady-state coverage. The Isotherms were measured at a

temperature above 430 K because at lower temperatures the equilibration was too slow for this assumption to hold.

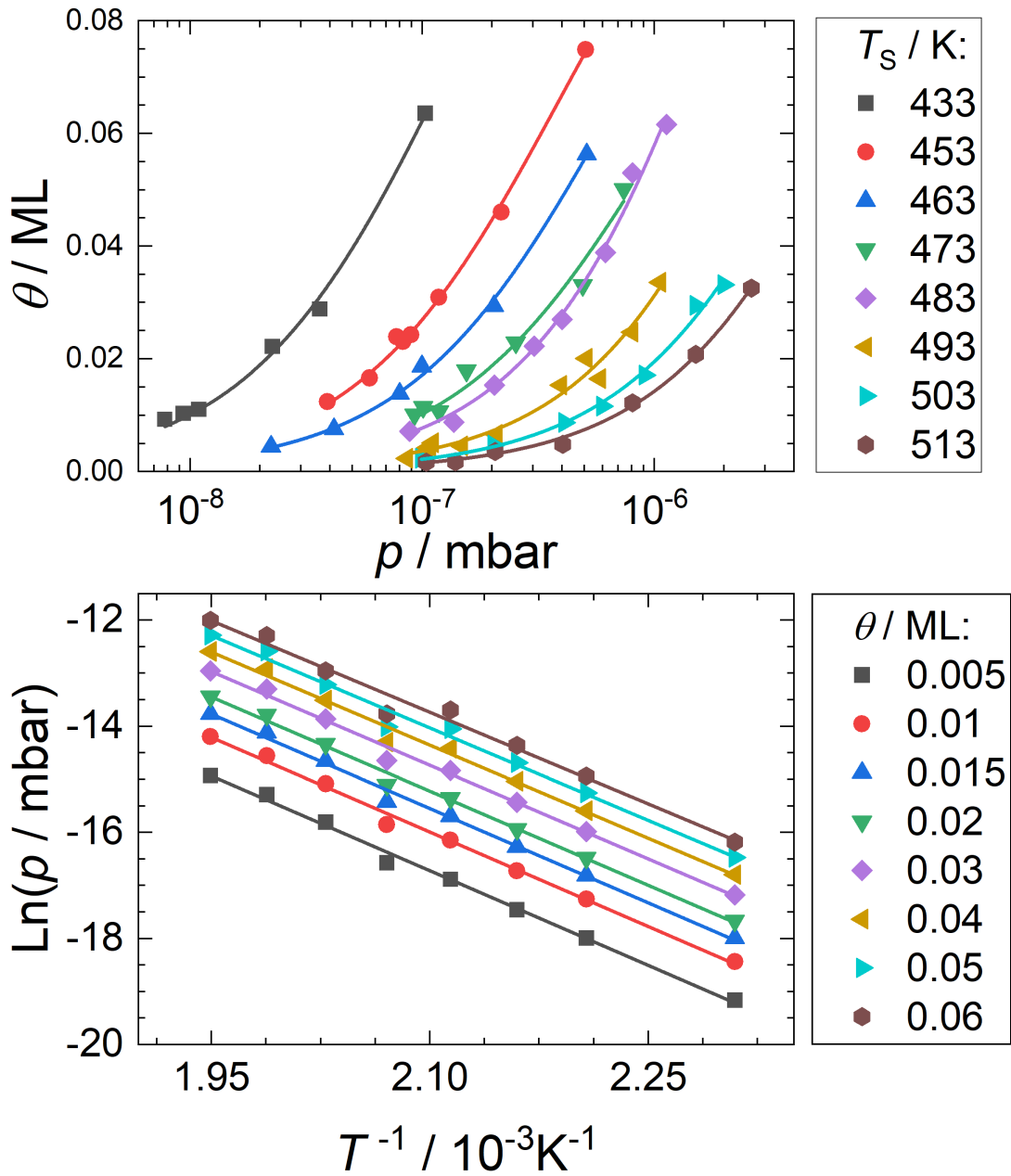


Figure 5.11: Measured adsorption isotherms of CO on Pt(111) are shown in the top panel. For clarity, the pressure is plotted on a logarithmic scale. The lines are Langmuir isotherm fits to the data. The bottom panel shows a selection of isosteres taken as horizontal lines from the top panel. The lines are linear fits to the data.

The isotherms were fitted with the Langmuir adsorption model:

$$\theta = \theta_{\max} \frac{K \cdot p}{1 + K \cdot p} \quad (5.2)$$

with the equilibrium constant K and the pressure p . The Langmuir model assumes the heat of adsorption, ΔH_{Ad} , to be independent of coverage, which is known to be

wrong for CO on platinum [73]. ΔH_{Ad} decreases with coverage because of interactions between adsorbates. But this simple model describes the data well because only the low coverage region was probed. This shows that the approximations of the Langmuir model are valid for CO on platinum in the low coverage limit.

The Langmuir adsorption model is used only as approximate interpolation of the data. Adsorption isosteres are obtained by selecting several horizontal lines in the top panel of Figure 5.11 with constant coverage. They are then fitted with the thermodynamic Clausius-Clapeyron equation:

$$\frac{d\ln(p)}{dT^{-1}} = -\frac{\Delta H_{\text{Ad}}}{k_{\text{B}}} \quad (5.3)$$

The isosteric heat of adsorption is obtained from the slope of the linear fits, which are shown in the bottom panel of Figure 5.11. In the low coverage limit, ΔH_{Ad} decreases steadily with increasing coverage, as shown in Figure 5.12. The decrease is only 3% for the first 0.05 ML of CO, which is in the order of the error bars. This warrants the assumptions of the Langmuir model at these low coverages. Extrapolating to zero coverage yields $\Delta H_{\text{Ad}} = 1.03 \pm 0.03$ eV.

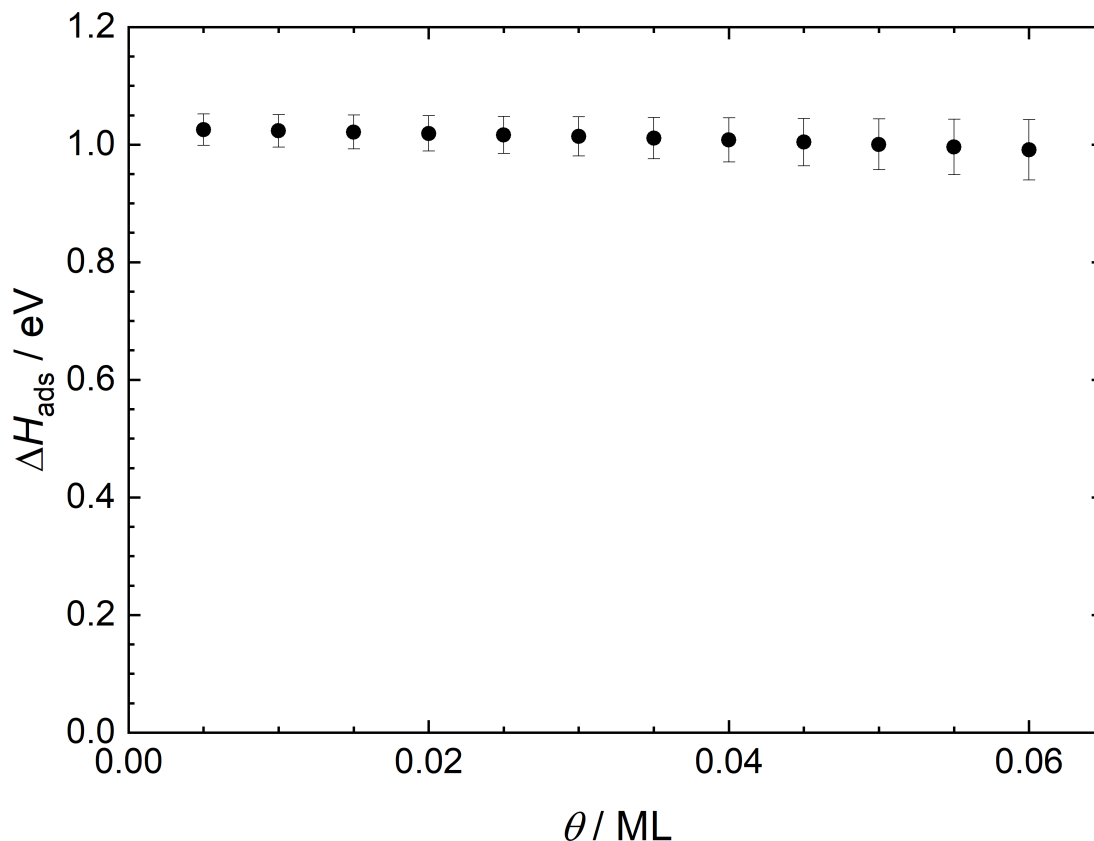


Figure 5.12: Resulting isosteric heat of adsorption of CO on Pt(111) at low coverage. For the first 0.05 ML, the decrease is only 3%.

5.3.3 LID rate constant

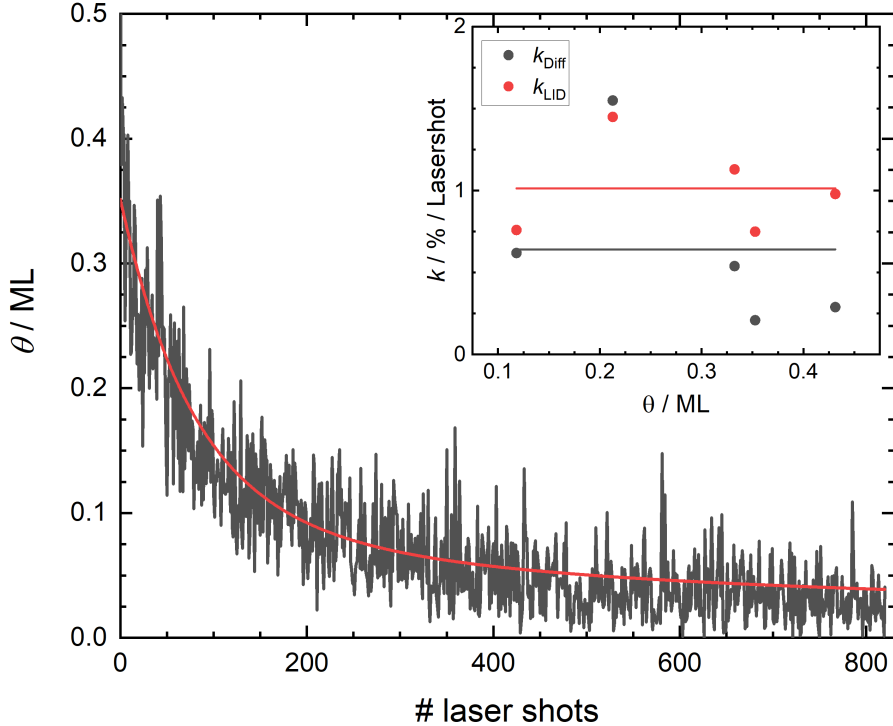


Figure 5.13: Decay of the coverage due to the desorption laser, removing CO from Pt(111) at 300 K. 15000 MB pulses were dosed before exposing the surface to the desorption laser, firing with a repetition rate of 5 Hz. The black line corresponds to the measured data points with single laser shot per image, and the red line is the numerical fit (Equation (4.33)) to the data, which includes diffusion of CO. The inset shows the results for k_{LID} and k_{Diff} as a function of coverage, and the horizontal lines represent the averaged value.

As described in Section 4.6, the LID desorption rate constant k_{LID} was determined by solving the rate equations Equation (4.33) numerically and fitting it to the data which was measured as described in Section 5.3.2. One example measurement is shown in Figure 5.13 where the surface was dosed with 15000 MB pulses and held at room temperature, where TD can be neglected. The inset shows the rate constants, which were found to be approximately independent of coverage. The averaged value for k_{LID} is $(1.0 \pm 0.2)\%$ of the coverage per laser shot or $(0.049 \pm 0.010) \text{ s}^{-1}$ with the repetition rate of 5 Hz. The averaged value for k_{Diff} is $(0.6 \pm 0.3)\%$ per laser shot, which determines the refilling of the coverage inside the laser spot.

5.3.4 Internal energy of the LID flux

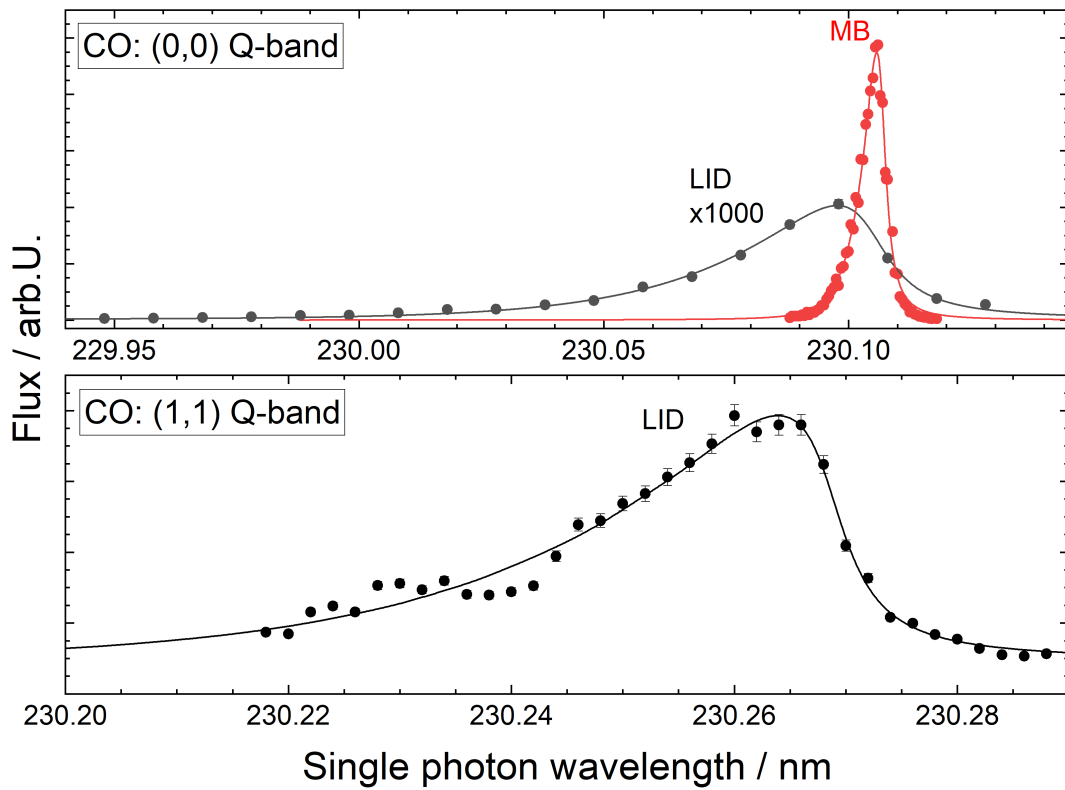


Figure 5.14: REMPI spectra of the CO $B^1\Sigma_g^+ \leftarrow X^1\Sigma_g^+(0,0)$ and $B^1\Sigma_g^+ \leftarrow X^1\Sigma_g^+(1,1)$ Q-band. The LID flux is shown as black points and the MB flux as red points. The lines are the fits to the data as described in Section 4.5. The Pt(332) surface was held at room temperature.

Figure 5.14 shows the REMPI spectra of the Q-heads of $B^1\Sigma_g^+ \leftarrow X^1\Sigma_g^+(0,0)$ and $B^1\Sigma_g^+ \leftarrow X^1\Sigma_g^+(1,1)$. In contrast to the MB pulse, the LID spectral peaks are much broader and the rotational temperatures of $B^1\Sigma_g^+ \leftarrow X^1\Sigma_g^+(0,0)$ and $B^1\Sigma_g^+ \leftarrow X^1\Sigma_g^+(1,1)$ are 1030 ± 50 K and 1130 ± 110 K, respectively. From integrating over the Q-heads, the vibrational temperature can be estimated to 1470 ± 10 K. Both the rotational - and vibrational temperature greatly exceed T_S .

5.3.5 Kinetic energy of the LID flux

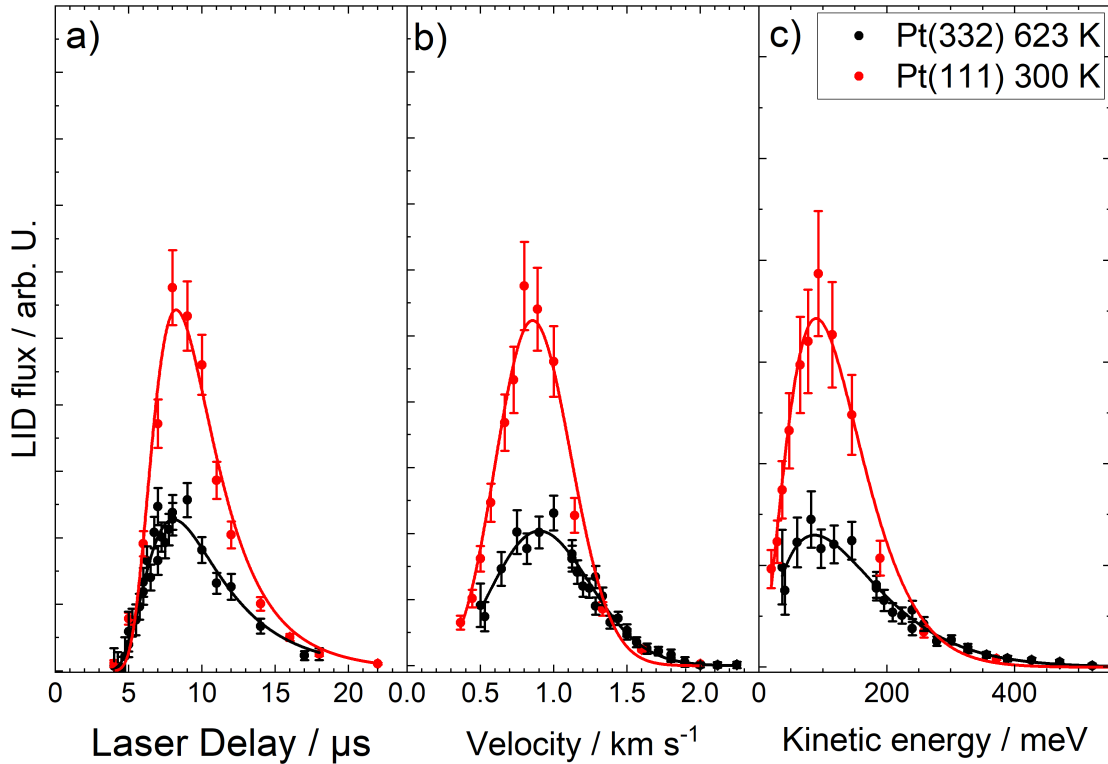


Figure 5.15: Example TOF distribution (a), velocity distribution (b) and kinetic energy distribution (c). The Pt(332) (black) was held at 623 K and Pt(111) (red) at 300K. The lines are the best fits to the data using the hyperthermal fitting functions Equations (4.11), (4.13) and (4.15) with T fixed to the respective surface temperature.

As described in Section 4.2, the TOF distributions are directly recorded by scanning the laser delay over the time period of several μs . The velocity distributions and kinetic energy distributions are calculated using the known distance between the sample and the detection laser $d_{\text{S-L}}$. Figure 5.15 shows some examples of measured distributions for Pt(332) and Pt(111). For Pt(111) the distributions are much narrower due to the lower T_{S} . They cannot be well described with the Maxwell-Boltzmann distribution of any temperature, which shows that the distributions are hyperthermal. When using the hyperthermal distribution functions (see Section 4.2.2), the data is fitted very well, as shown in Figure 5.15.

5.3.6 Laser pulse duration dependence

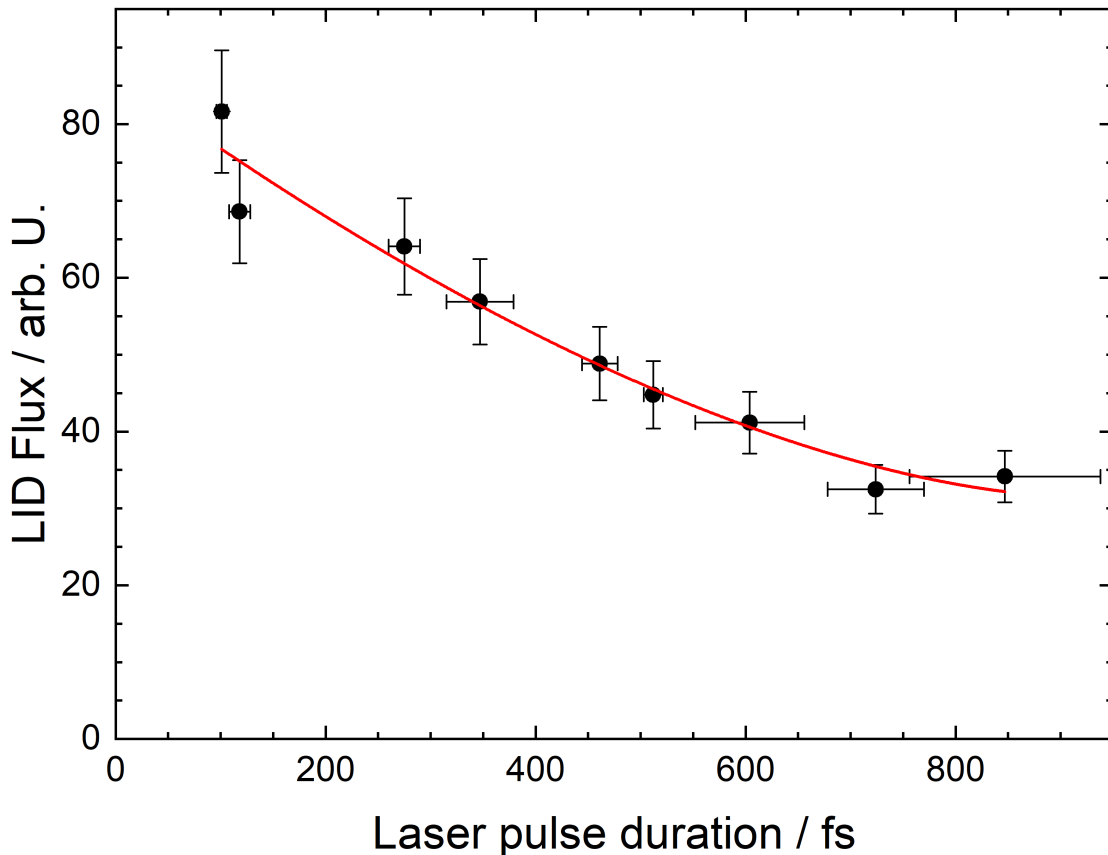


Figure 5.16: Dependence of the CO LID flux on the desorption laser pulse duration. The red line is the power law fit to the data.

Variation of the desorption laser pulse duration does not change the total laser power, but only the peak power. Nonetheless, the measured LID flux increases with shorter pulse duration below ≈ 700 fs. This dependency is shown in Figure 5.16 and is fitted with a power law which is approximately linear. Above 700 fs the measured LID flux stagnates at a constant level of $\approx 40\%$ of the LID flux at 100 fs. Even at much higher pulse duration above 1 ps, the LID flux signal stays constant, which is not shown in Figure 5.16 because the autocorrelator did not allow to measure pulse duration longer than 1000 fs accurately. The constant level of LID flux corresponds to the phonon mediated LITD mechanism[74] which only depend on the laser pulse energy and not the laser pulse duration. The increase of the desorbing LID flux below 700 fs indicates the emergence of the additional electron-mediated desorption mechanism (see Section 2.2) which does depend on the pulse duration. The constant level of $\approx 40\%$ of the phonon-mediated LITD mechanism shows that both mechanisms play an important role at 100 fs pulse duration.

Figure 5.17 shows the REMPI spectrum of the $B^1\Sigma_g^+ \leftarrow X^1\Sigma_g^+(0,0)$ and $B^1\Sigma_g^+ \leftarrow X^1\Sigma_g^+(1,1)$ Q-bands for 100 and 1000 fs pulse duration representing the two different desorption mechanisms. The pulse duration shows a strong effect on the amplitude, but not on the width of the peaks. The resulting rotational and vibrational temperatures are summarized in Table 5.2. Differences in the rotational temperature between the two vibrational states and the two desorption mechanisms are small,

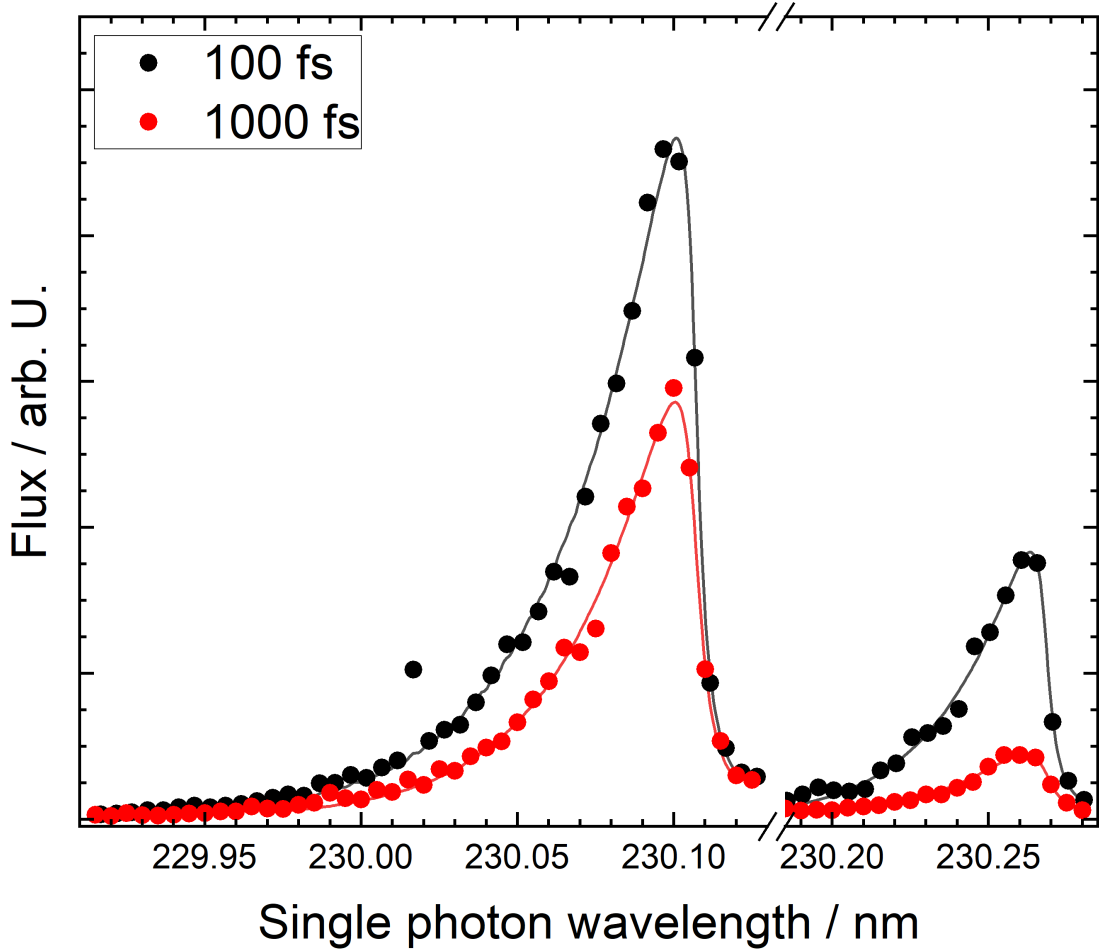


Figure 5.17: Influence of the pulse duration on the REMPI spectra of the LID flux. The Q-bands of the $B^1\Sigma_g^+ \leftarrow X^1\Sigma_g^+(0,0)$ (230.1 nm) and (1,1) transition (230.26 nm) are shown. Each measured with a pulse duration of 100 fs (black dots) and 1000 fs (red dots). The lines are fits to the data as described in Section 4.5.

with an average of $T_{\text{rot}} = 1350 \pm 150$ K. But the vibrational temperature shows a large difference between the two desorption mechanisms. This indicates that the electron-mediated desorption mechanism leads to significantly more vibrational excitation in the LID flux compared to the phonon-mediated desorption mechanism.

pulse duration	100 fs	1000 fs
$T_{\text{rot}}(B^1\Sigma_g^+ \leftarrow X^1\Sigma_g^+(0,0)) / \text{K}$	1340	1180
$T_{\text{rot}}(B^1\Sigma_g^+ \leftarrow X^1\Sigma_g^+(1,1)) / \text{K}$	1460	1440
$T_{\text{vib}} / \text{K}$	2500	1500

Table 5.2: Summary of rotational and vibrational temperatures of CO. The values were obtained from the fits of the REMPI spectra in Figure 5.17, as described in Section 4.5.

5.3.7 Laser fluence dependence

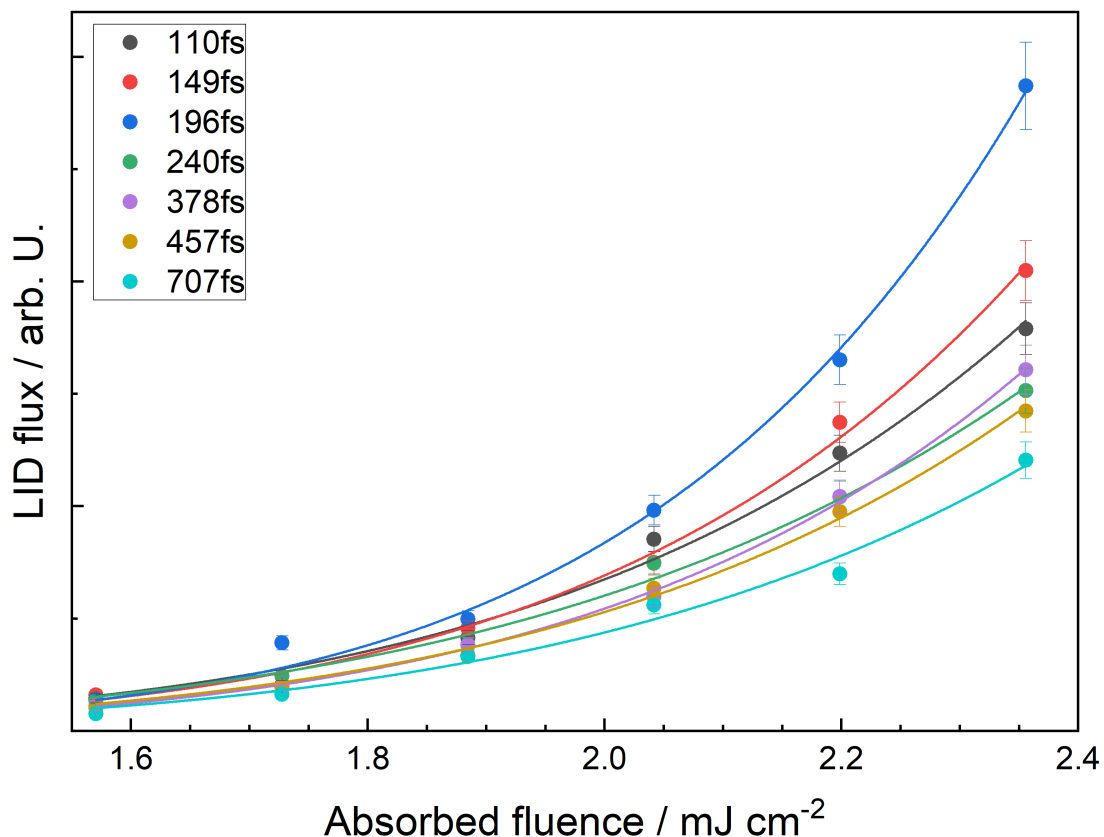


Figure 5.18: Dependence of the LID flux on the desorption laser fluence. Measured for a pulse duration from 110 fs to 707 fs. The lines are power law fits with Equation (2.4). The power k is fitted globally.

Figure 5.18 shows how the LID flux increases with the absorbed fluence for several pulse durations. The power law fit results in an exponent $k = 6 \pm 1$, independently of the pulse duration. This reveals that the LID process is highly non-linear.

Figure 5.19 shows the kinetic energy distributions with varying desorption laser fluence. The distribution changes only slightly: For a fixed value of $T = T_S$, the hyperthermal shift Δv increases with laser fluence and saturates at $\approx 530 \text{ m s}^{-1}$ (see Figure 5.20).

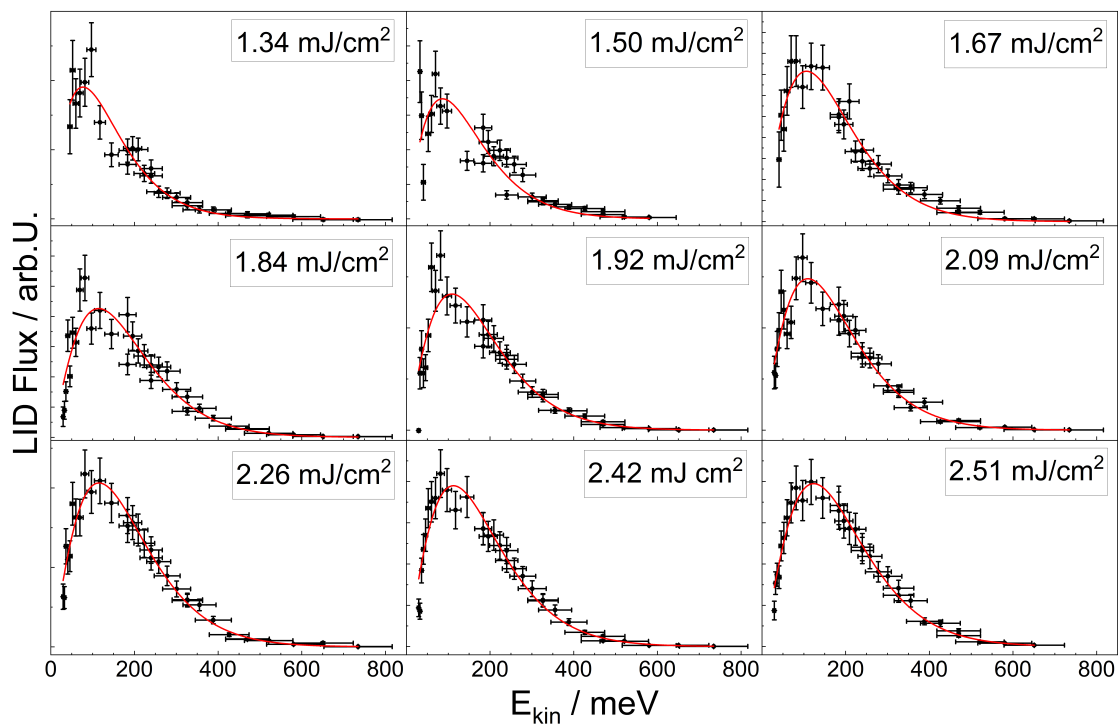


Figure 5.19: Kinetic energy distributions of the CO LID Flux with varying desorption laser fluence. The Pt(332) surface was held at 623 K.

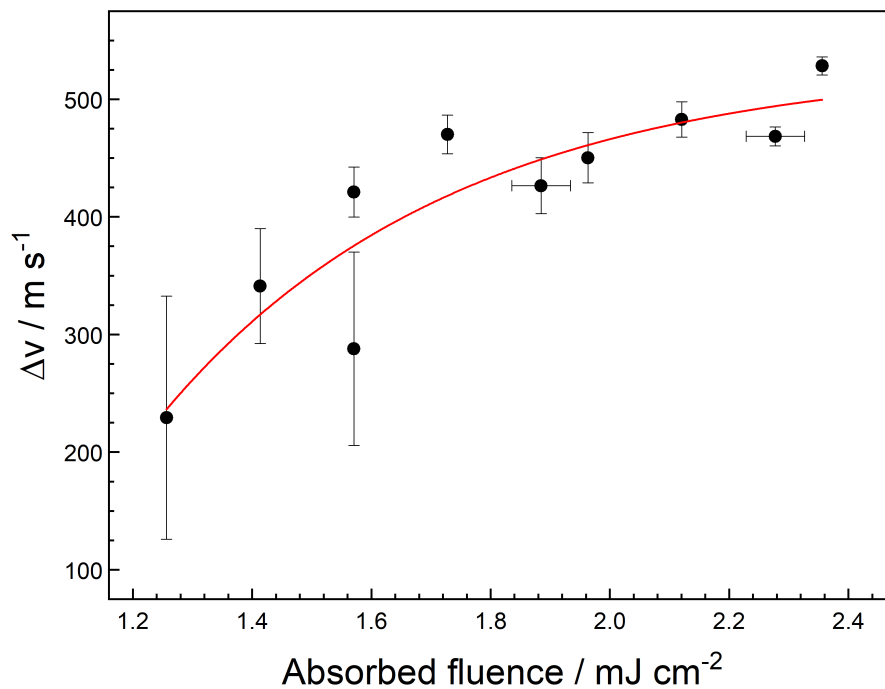


Figure 5.20: Influence on the hyperthermal shift. Dependence of the hyperthermal shift on the desorption laser fluence. The red line is the best asymptotic fit to the data.

5.3.8 Desorption kinetics

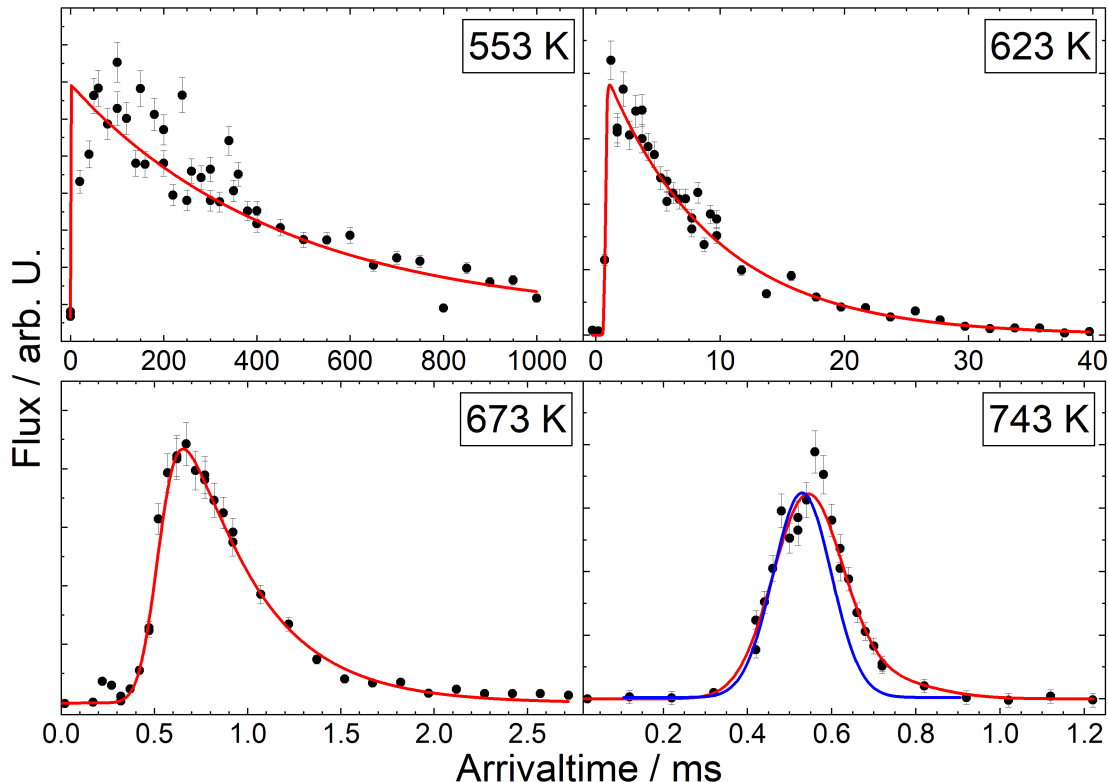


Figure 5.21: Kinetic traces of CO desorbing from Pt(332) at 4 different temperatures. The data points are shown as black dots and the fits to the data as red lines. The blue line in the graph of 470 K shows the molecular beam flux, which has been scaled down for comparison.

Figure 5.21 shows some example kinetic traces. They are fitted well with the convolution function in Equation (4.24) and the rate constant is obtained as fitting parameter. The parameters of the MB pulse were determined beforehand in Section 5.2 and were fixed for the fitting process. The rate constants were recorded for a broad temperature range from 543 K to 763 K. Above 763 K the thermal desorption becomes so fast that the measured exponential decay of the kinetic trace is not related to the desorption anymore. Then, only the falling edge of the MB pulse is measured, and the rate constants become independent of temperature. To illustrate this, the MB pulse is shown in the bottom right panel in Figure 5.21, where it is barely possible to determine k_D from the fit. The temperature dependence of the obtained rate constants can be fitted well with an Arrhenius function (Equation (4.21)).

To test the reliability of the LID-VRK method, the experiment was conducted under many conditions and the resulting rate constants are compared in Arrhenius plots in Figure 5.22. The complete set of kinetic traces and figures can be found in the appendix in figures Figure B.1 to Figure B.5.

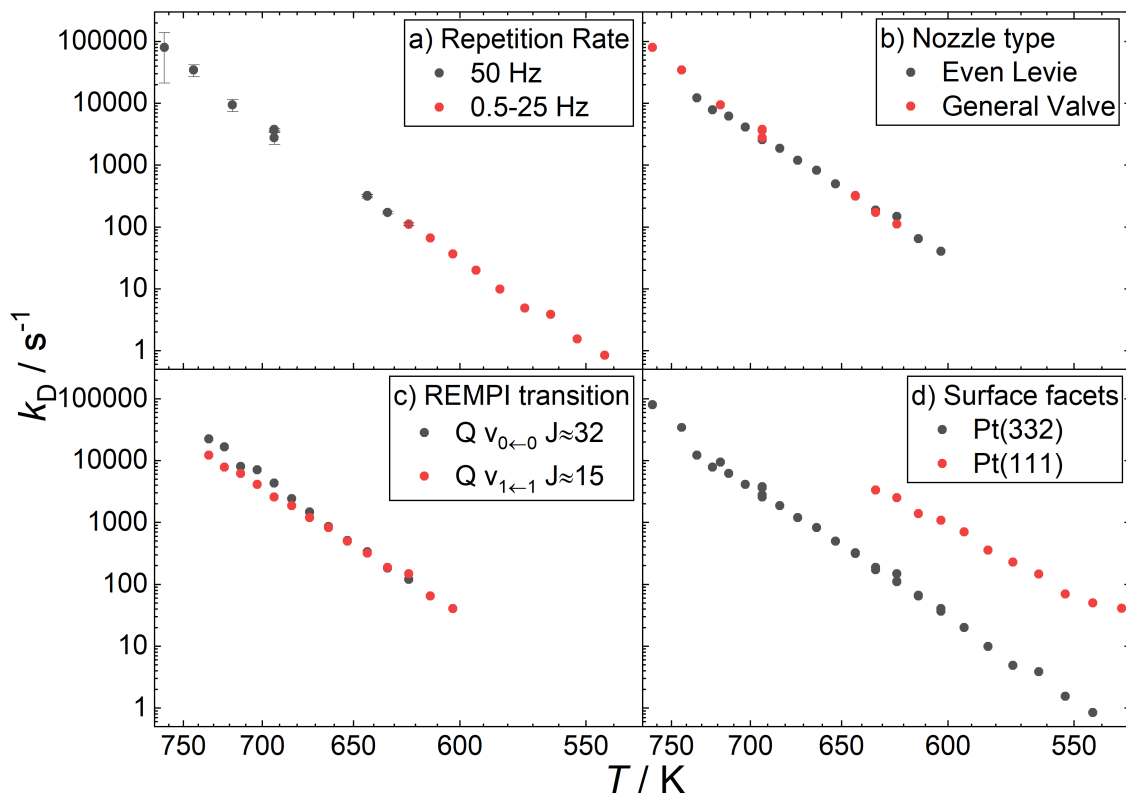


Figure 5.22: Arrhenius plots of the CO desorption rate constant for several temperatures and different experimental conditions. Unless stated otherwise, the repetition rate was 50 Hz, the nozzle type was the PGV nozzle, the REMPI wavelength was tuned to the $B^1\Sigma_g^+ \leftarrow X^1\Sigma_g^+(1,1)$ Q-head and the surface facet was Pt(332). Each panel shows the effect of changing one of these conditions.

Nozzle Repetition rate

Panel (a) of Figure 5.22 shows that the nozzle repetition rate has no influence on the kinetic rate constants. This is true only in the low coverage limit which was ensured for these measurements.

Investigations at higher coverage are summarized in Figure 5.23. The repetition rate can only be set to discrete values, which are given by dividing the maximum repetition rate of 50 Hz by an integer n . For high temperatures, 623 K and 693 K, the LID flux is almost constant for each repetition rate which is an indication of the low coverage limit where each MB pulse doses an equal amount of CO to the surface which desorbs completely before the next MB pulse. At 573 K up to 10 Hz the system is still in the low coverage limit, but at 25 and 50 Hz the coverage is no longer depleted before the next MB pulse and a steady-state coverage is building up, which is indicated by the increase in LID flux. Then the steady-state coverage does depend on the repetition rate, and therefore the LID flux does as well. For 623 K at 50 Hz a small increase in flux already signifies a small amount of steady-state coverage buildup. This effect is even more pronounced at 523 K where the low coverage limit is never reached for $f_{RR} \geq 1$ Hz and a large buildup of the steady-state coverage is observed.

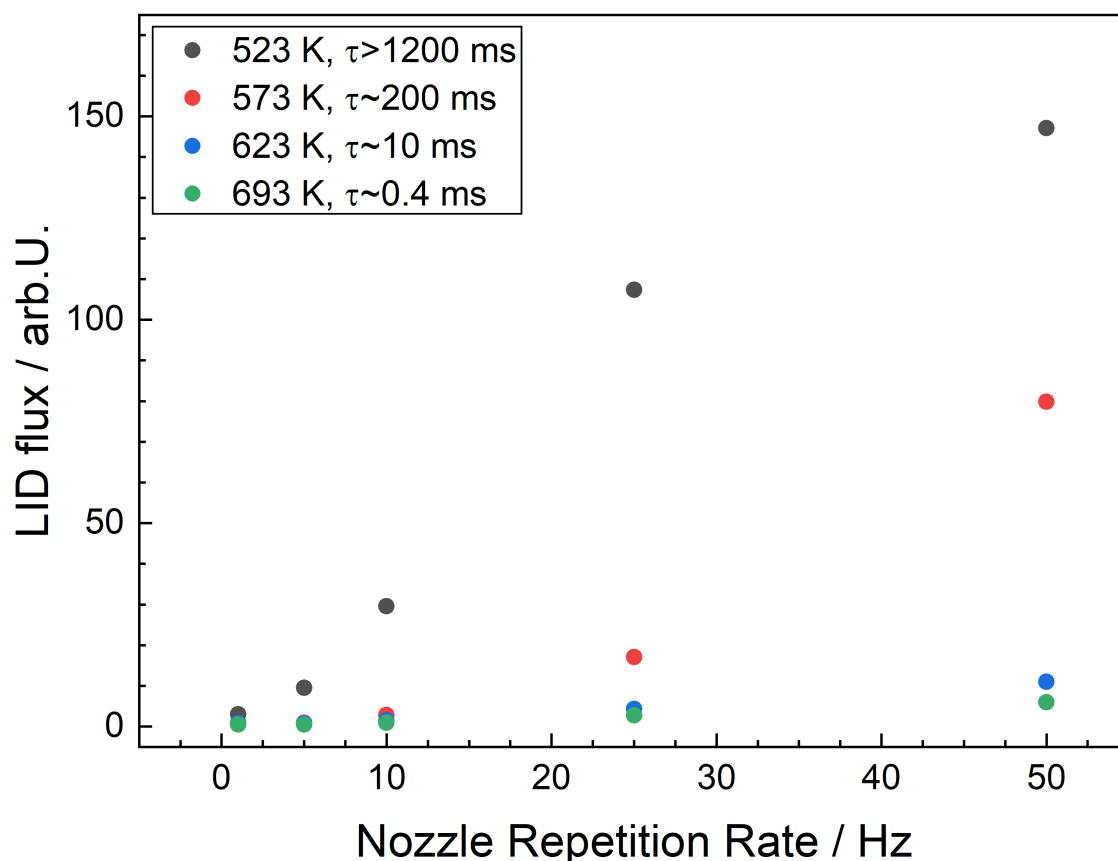


Figure 5.23: LID flux increase due to buildup of a steady state coverage on Pt(332). The LID flux was measured for several nozzle repetition rates at a surface temperature of 523 K (black), 573 K (red), 623 K (blue) and 693 K (green). The signal is normalized by dividing by the number of LID laser shots. The measured adsorption lifetimes are given in the legend to compare to the repetition rate according to Equation (4.25).

Nozzle Type

Kinetic measurements were performed with both MB nozzles to rule out any influence of the nozzle type on the measured kinetic rate constants. The comparison is shown in panel (b) of Figure 5.22 and reveals no apparent differences. This result was expected, because the value of the desorption rate constants should not depend on the way the molecules were dosed. The only expected advantage of the ELT nozzle is a shorter MB pulse width, which enables faster desorption at higher temperatures to be measured. The high temperature limit with the ELT nozzle has not been exhausted in this work.

REMPI transitions

To test if the detected vibrational state has an influence on the kinetic traces, the detection REMPI laser was tuned to the $B^1\Sigma_g^+ \leftarrow X^1\Sigma_g^+(0,0)$ Q-band. At the head of the Q-band, the signal of the TD flux of CO is very strong and the overlap with the LID flux is large. Although the velocities are very different, the overlap was too large to determine the rate constants accurately. To overcome this problem, the

wavelength was tuned to a high rotational state ($J \approx 32$) of the $B^1\Sigma_g^+ \leftarrow X^1\Sigma_g^+(0,0)$ Q-band, where the contrast between the LID signal and the TD signal is much better.

Panel (c) in Figure 5.22 compares the desorption rate constants of CO in the vibrational state $v = 0$ and $v = 1$. They are very similar but show small systematical differences at high temperatures. The discrepancy is probably due to the higher uncertainty at high temperatures.

Surface facets

Panel (d) of Figure 5.22 demonstrates the large difference between the desorption rate constants of Pt(111) and Pt(332) which is more than one order of magnitude. This difference is due to the vastly different step density of those two surface facets, as discussed in Section 2.1). The desorption from Pt(111) corresponds to desorption from terraces and for Pt(332) desorption from steps, which is an effective rate constant for diffusion from step to terrace and subsequent desorption from the terrace. The slope is also different, which corresponds to an activation energy for desorption from Pt(111) of $E_D = 1.43 \pm 0.04$ eV and $E_D = 1.65 \pm 0.03$ eV from Pt(332). The obtained prefactors are $A = 10^{14.9 \pm 0.3} \text{ s}^{-1}$ and $A = 10^{15.7 \pm 0.3} \text{ s}^{-1}$ for Pt(111) and Pt(332), respectively.

5.4 Oxygen on platinum

On Pt(332), Molecular oxygen adsorbs into a chemisorbed molecular state either directly or via a weakly bound physisorbed state by 0.08 eV[75]. From this state, the molecule can either dissociate or desorb back to the gas phase. The initial sticking probability decreases from 0.6 to 0.3 between 100 K and 600 K for low incident energy[76]. But because of the precursor state, the dissociation probability is even lower than the initial sticking probability. The dissociation is an activated process with a barrier of 0.86-0.9 eV[77] which takes place only at step sites, even on Pt(111)[78]. A direct dissociation pathway has been observed for high incident energy[79]. But this pathway is not relevant for this work because the incident energy of the MB pulse is very low. The chemisorbed O₂ is weakly bound with a theoretical binding energy of 0.35 eV[75] while atomic oxygen is bound strongly with 2.6 eV[76] on step sites.

This system is used to test the LID for these edge cases for very weak and very strong binding. All three states of the ³P_J triplet ground state of O-atoms as well as molecular oxygen can be observed in the LID flux. Molecular oxygen is distinguished by mass and the O-atom state by the REMPI wavelength.

5.4.1 Dissociation of Oxygen

At the detection laser, O₂ can absorb the UV-photons via electric dipole forbidden transitions in the Herzberg continuum[57]. This leads primarily to photo-dissociation and the ³P_J O-atom fragments are selectively ionized by REMPI. Intact O₂ molecules are ionized non-resonantly in the process. The branching ratio of the O-atoms states in the photo-dissociation is 1.0:2.9:8.7 for ³P₀, ³P₁ and ³P₂, respectively[80].

Figure 5.24 shows the images of O-atoms and molecular O₂ in the O₂ background gas. The branching ratio between the dissociation and O₂ ionization or between the three O-atom states could not be determined quantitatively from these images because not all fragments are detected. But according to Parker *et al.* [81], the fraction of dissociation is at least 20%. The different shape of the three ³P_J states indicate that the Newton sphere of dissociation products involve directional preferences relative to the horizontal laser polarization in the *xy*-plane. This leads to different amount of dissociation in *z*-direction which are excluded due to the slicing detection. In the bottom right panel, the O₂ signal reproduces the laser beam path, which is broadened only by the thermal velocity distribution of O₂ at room temperature. The O-atoms in the ³P₂ state (bottom left panel) apparently are created in two dissociation channels: One with a large kinetic energy release indicated by the large distance from the laser focus and the other with low kinetic energy release corresponding to the peak in the center. O-atoms in the ³P₁ and ³P₀ state (top panels) appear to only be created by the dissociation with low kinetic energy. No indication of a dependence on the laser polarization was found when rotating the laser polarization with a λ/2 wave plate.

The knowledge of the gas-phase dissociation is used to distinguish dissociation products from O-atoms in the LID flux. The O₂ dissociation products originate from the detection laser position in all directions, while the desorbing flux originates from the sample position only moving away from the surface in *x* direction. Because of the

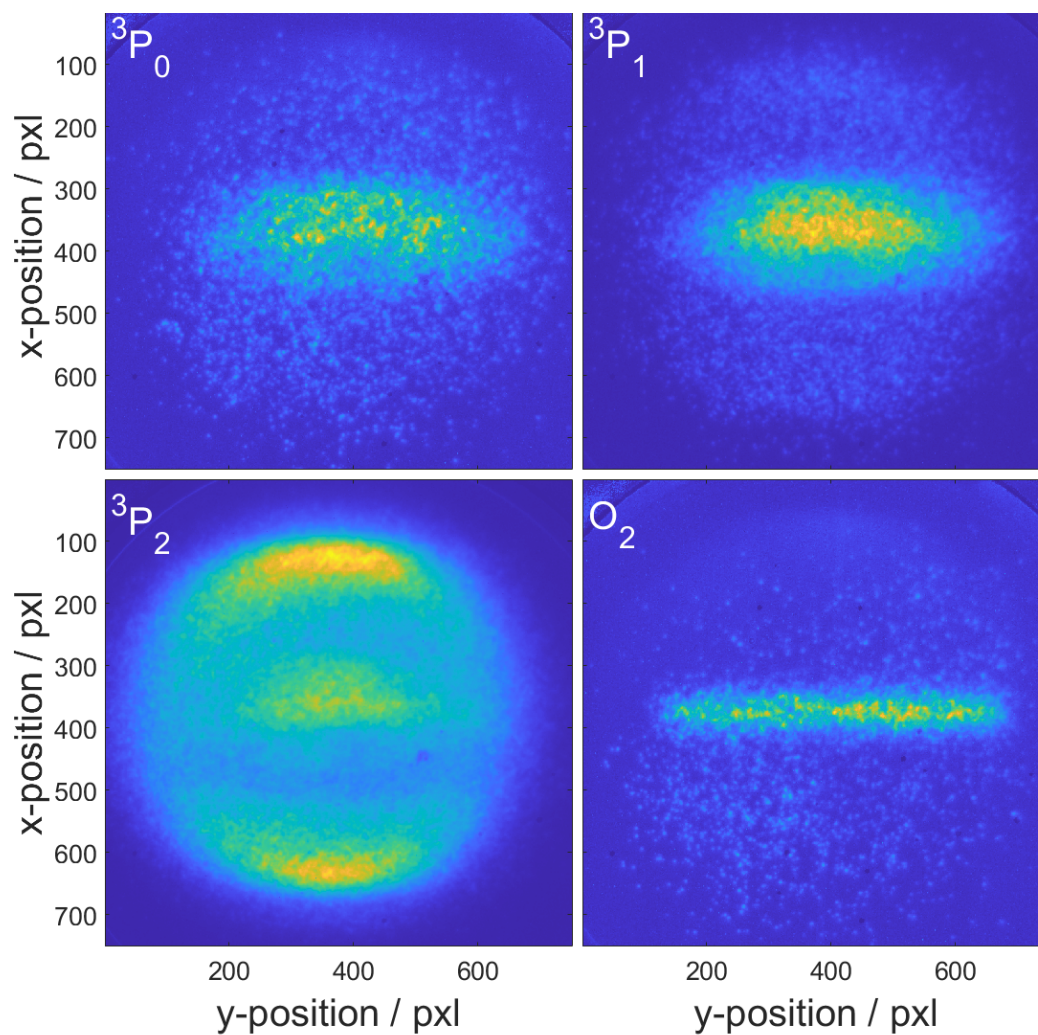


Figure 5.24: Raw images of oxygen background gas, with the REMPI wavelength tuned to each atomic state of the O-atoms. Molecular oxygen was ionized non-resonantly. The O-atoms are created by photo-dissociation.

large kinetic energy release, the 3P_2 dissociation products quickly leave the detection area when using delayed extraction.

5.4.2 Kinetic energy of the LID flux

The surface was dosed with a constant background pressure of $2 \cdot 10^{-7}$ mbar O_2 which results in a steady-state coverage of chemisorbed O_2 and O-atoms. Each coverage depends on the dissociation rate, the desorption rate of chemisorbed O_2 and the recombinative desorption rate of O-atoms, which all depend on T_S . The top panel of Figure 5.25 shows the kinetic energy distributions of O-atoms and O_2 in the LID flux at $T_S = 318$ K. Both distributions are hyperthermal, but it is apparent that the distribution of O-atoms is much broader and shifted to higher kinetic energy. This difference is due to the vastly different binding energies. LID signal of O_2 was only observed at room temperature and up to 318 K. For higher surface temperatures, no O_2 LID signal was observed. This indicates that the coverage of chemisorbed O_2 is really low due to fast dissociation or desorption, which accelerate further with increasing surface temperature. The vanishing of the O_2 LID flux above 318 K, indicates that the O_2 LID flux is proportional to the coverage of chemisorbed O_2 . If the desorption laser would induce O-atom recombination, the O_2 LID flux would depend on the O-atom coverage, which has a very different temperature dependence (see bottom panel of Figure 5.25).

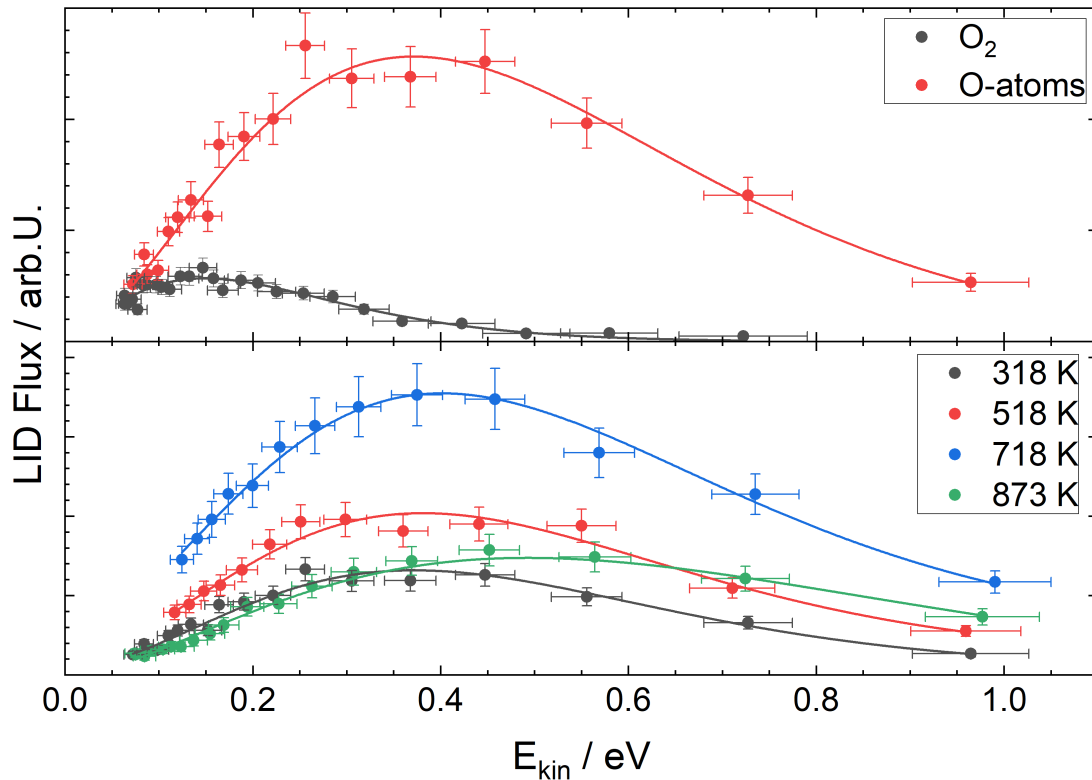


Figure 5.25: Kinetic energy distributions of the LID flux with a constant dose of $2 \cdot 10^{-7}$ mbar O_2 . The top panel compares O_2 and O-atoms at $T_S = 318$ K. The bottom panel compares the O-atom LID flux for a surface temperature of 318 K (black), 518 K (red), 718 K (blue), 873 K (green).

The effect of surface temperature on the O-atom coverage, which is proportional to the O-atom LID flux, is shown in the bottom panel of Figure 5.25. At the first three temperatures, only the amplitude of the distribution changes. At the highest temperature of 873 K, the distribution is slightly broader and shifted to higher kinetic energy. From 318 K to 718 K the LID flux increases with temperature, while from 718 K to 873 K it decreases. The dissociation of O₂ is a highly activated process with a barrier of 0.86-0.9 eV relative to chemisorbed molecular state[77]. At low temperatures, most chemisorbed O₂ molecules can not overcome the barrier and just desorb, hence the coverage of O-atoms is very low. With increasing temperature, the dissociation rate of O₂ but the desorption rate of chemisorbed O₂ also increases. A possible explanation for the experimental finding that the LID flux increases with *TS* is that above 300 K the temperature dependent increase of the dissociation rate is faster than the increase of the desorption rate of chemisorbed O₂ and therefore the overall O-atom coverage increases. This agrees with the fact that the activation energy for dissociation is larger than for desorption, 0.86-0.9 eV[77] compared to 0.35 eV[75], which indicates a larger temperature dependence.

On high step density surfaces, the recombinative desorption of oxygen becomes relevant at temperatures above 700 K[76] which decreases the O-atom coverage in addition to the desorption of molecular O₂. This can explain the strong decrease of LID flux at 873 K.

5.4.3 Laser pulse duration dependence

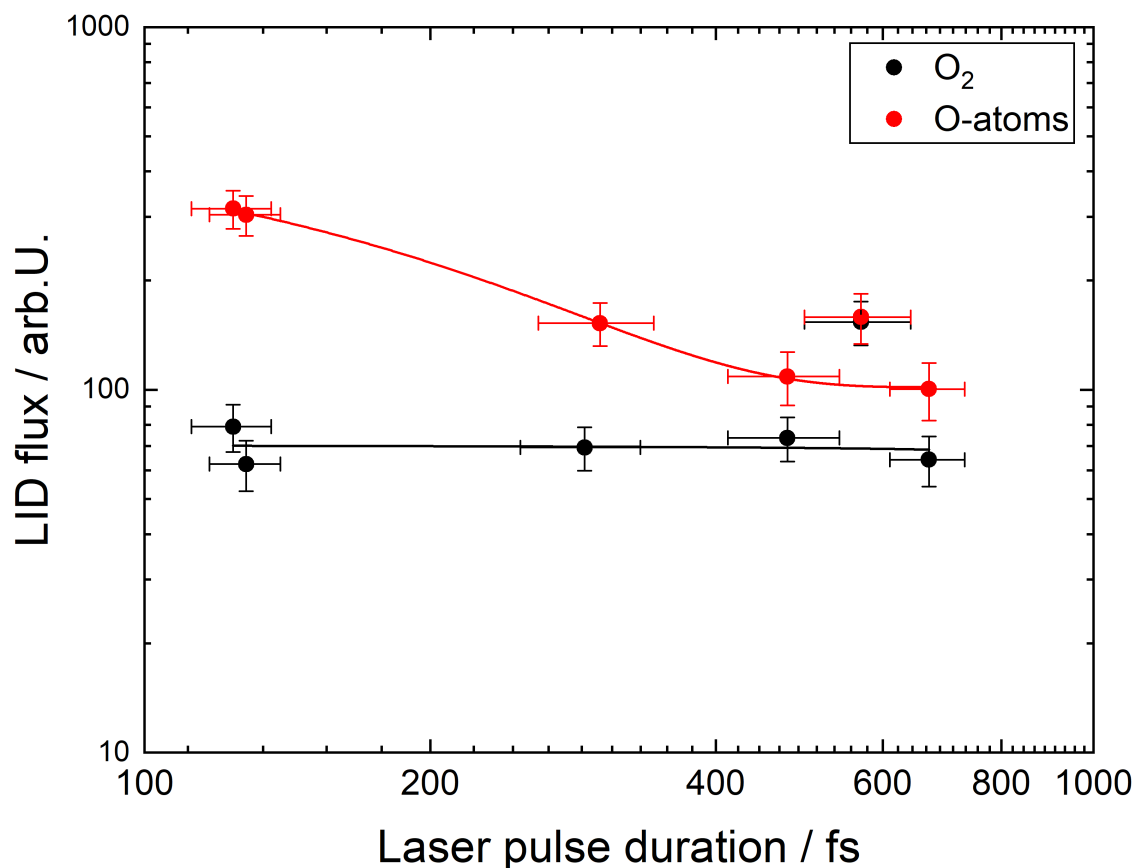


Figure 5.26: Double-logarithmic plot of the LID flux of O₂(black) and O-atoms(red) as a function of the desorption laser pulse duration. The lines are power law fits to the data. The data points at 580 fs are excluded from the fit.

Figure 5.26 shows the desorption laser pulse dependence of the LID flux for O-atoms and O₂. For O-atoms, the LID flux increases with shorter pulse duration for a pulse duration below ≈ 500 fs, similarly to CO. The power law is not linear, but increases with a power of 4 ± 1 . For O₂ on the other hand, the LID flux shows almost no dependence on the pulse duration. Therefore, O₂ can be assigned to the pure phonon-mediated desorption mechanism and O-atoms to the combination of both the electron-mediated desorption and phonon-mediated desorption mechanism. The different behavior can be explained with the different binding energies. The contribution of the phonon-mediated desorption to the O-atom LID signal is 30% at 124 fs which indicates a more dominant role of the electron-mediated LID process compared to CO.

5.4.4 Laser fluence dependence

The fluence dependence in Figure 5.27 is very different between O-atoms and O₂. The LID flux of the O-atoms increases with the laser fluence with a power of $k = 9 \pm 1$ which is highly non-linear. Molecular oxygen on the other hand increases with fluence with a power of $k = 1.6 \pm 0.2$. This leads me to assigning O₂ to a predominantly phonon-mediated LITD process and O-atoms to a large contribution of

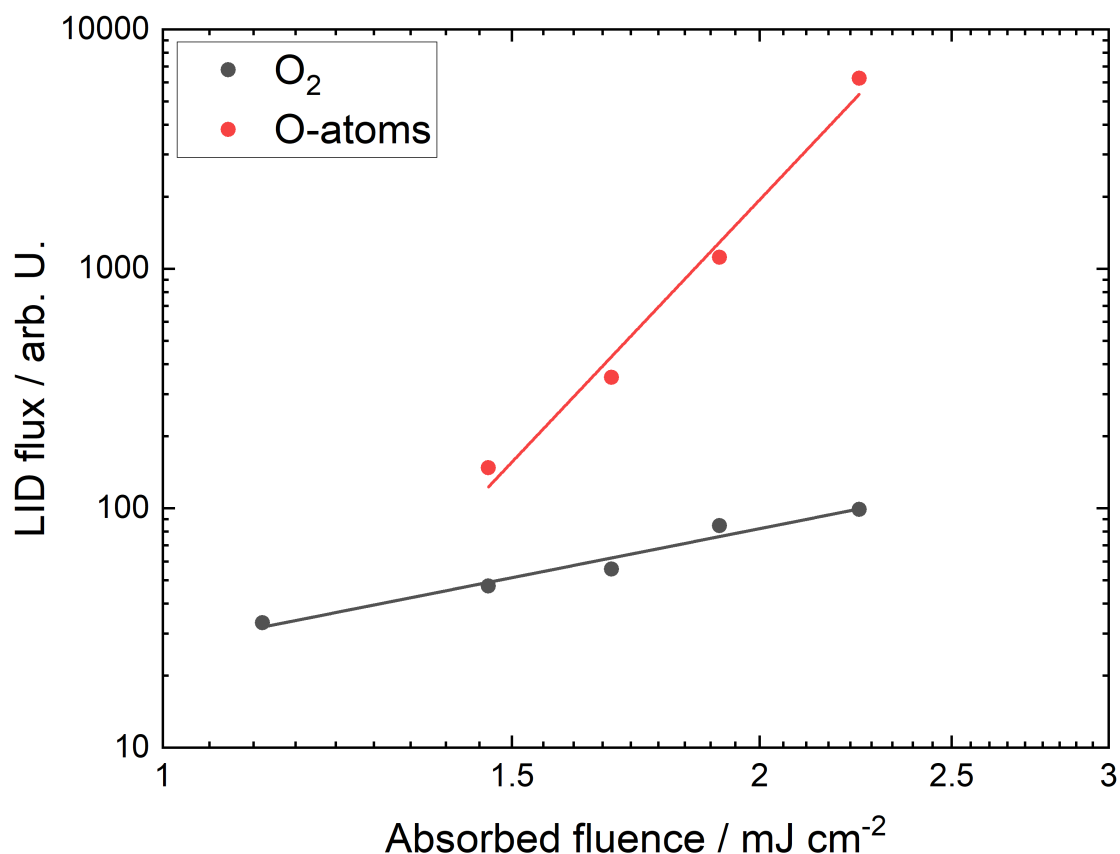


Figure 5.27: Double-logarithmic plot of the LID flux of O₂ and O-atoms as a function of the absorbed laser fluence. The Pt(332) surface was held at 300 K and dosed with $2 \cdot 10^{-7}$ mbar O₂. The lines are power law fits with Equation (2.4).

electron-mediated LID. The contrary has been found for LID of chemisorbed O₂ from Pt(111)[27] and Pd(111)[32]. They found a highly non-linear fluence dependence, similar to O-atoms in this work, but their experiments were conducted at much lower temperatures. They used cryogenic temperatures of 80 K and 140 K, respectively, which are below the temperature programmed desorption (TPD) peak temperature of 150 K[82]. At these cryogenic temperatures, the dissociation is suppressed[83] and the coverage of chemisorbed O₂ is much higher than at 300 K, which was used in this work. Maybe the low coverage of chemisorbed O₂, and therefore weak LID signal, did not allow me to observe the fluence dependence accurately.

5.4.5 Desorption kinetics

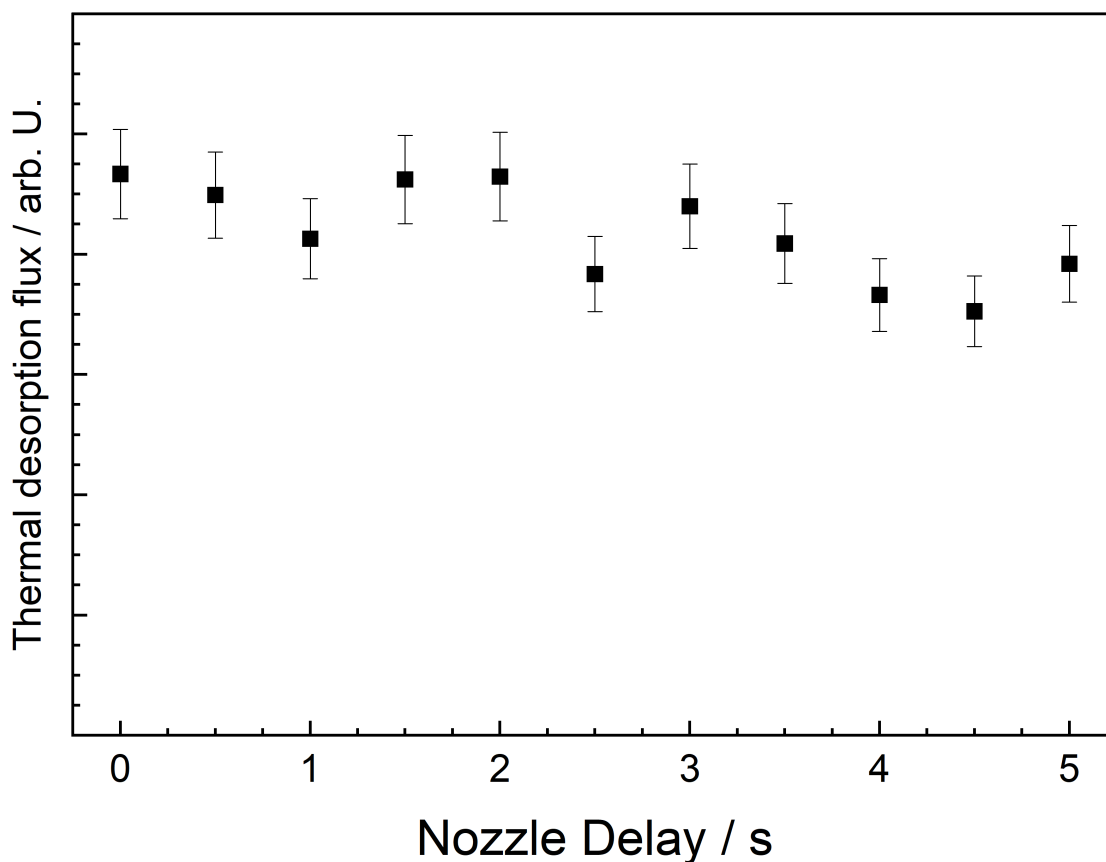


Figure 5.28: Kinetic trace of the TD flux of O_2 desorbing from Pt(332) at 1173 K. The experiment was carried out with a repetition rate of 0.2 Hz.

Thermal desorption (TD) of atomic oxygen from stepped platinum occurs from 700 K to 900 K associatively[76] with presumably second order kinetics. Unfortunately, attempts to measure the recombinative desorption kinetics were unsuccessful. At the highest reachable surface temperature, $T_S = 1173$ K, the O-atom LID signal can be observed, but the signal is very weak and falls below the detection limit for a repetition below 5 Hz. To attempt to measure the slow recombinative desorption, the TD signal of O_2 was recorded as a function of the nozzle delay, with a low repetition rate of 0.2 Hz. The kinetic trace is shown in Figure 5.28. It theoretically consists of first order desorption of chemisorbed O_2 and recombinative desorption, which is second order. But the desorption of chemisorbed O_2 is too fast at this temperature to play a role on this long timescale. The kinetic trace exhibits almost no dependence on the delay of the MB pulse over the modulation time of 5 s. This indicates that the recombinative desorption is too slow to desorb all oxygen-atoms in that time, and a steady state coverage of O-atoms is established.

5.5 Ammonia on platinum

Ammonia binds to clean Platinum without dissociation, but is readily dissociated if oxygen is present on the surface[84] which is an important catalytic reaction. A recent VRK study Borodin *et al.* [12] determined the binding energy of NH_3 on platinum as 1.13 eV and 1.36 eV for terraces and steps, respectively. These binding energies are lower compared to CO on platinum, hence the desorption rate is expected to be faster. Here, the desorption kinetics of NH_3 from Pt(111) was investigated as a secondary system to test the LID-VRK method and compare to previous methods. This system tests if the method can probe the coverage of weakly bound, polyatomic molecules without dissociation.

5.5.1 Dissociation of ammonia

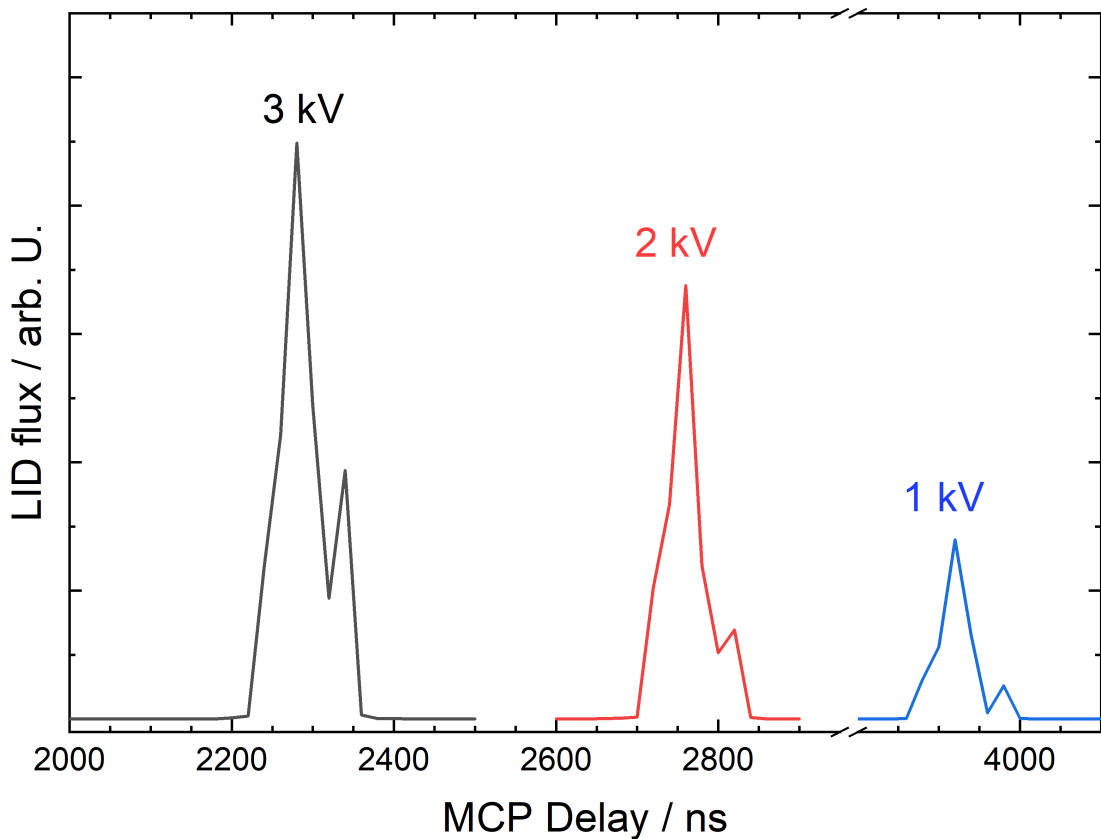


Figure 5.29: MCP-gate scans of the NH_3 LID flux from Pt(111) for a repeller voltage U of 3 kV (black), 2 kV (red) and 1 kV (blue). The molecules were ionized by non-resonant MPI.

To investigate if the desorption laser induces ammonia dissociation on the surface, MCP-gate scans of the LID flux were recorded at different repeller voltages. With a lower repeller voltage, the mass resolution is improved (see Equation (4.7)) because of the longer TOF in z -direction. The results are shown in Figure 5.29 and exhibit a main peak with a small shoulder towards higher delay, which corresponds to a larger mass. With a repeller voltage of 3 kV, the difference between the main peak is 60 μs , which would correspond to a mass difference of $\Delta m = 1$ amu. For

lower repeller voltages, the peak is expected to shift to longer MCP gates and the Δm is expected to scale up accordingly. But it is found that the difference between the peaks stays constant for all repeller voltages. This indicates that the shoulder is an artifact and not related to a different mass Δm . The cause of the artifact probably was a misalignment of the detection laser beam.

Since no fragmentation is observed, the main peak can be assigned to the intact NH_3 molecule with 17 amu, which agrees well when comparing to the MCP gate of CO under the same conditions.

5.5.2 Desorption kinetics

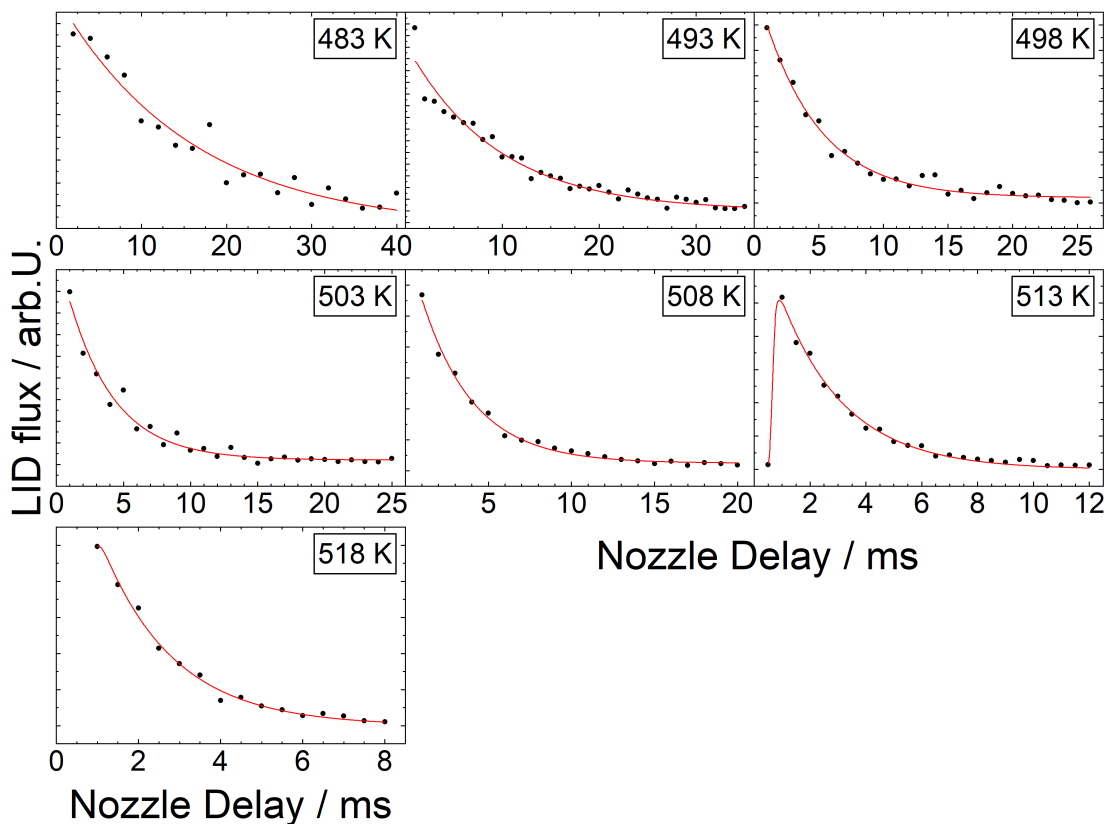


Figure 5.30: Kinetic traces of NH_3 from Pt(332). The desorbing flux is ionized with non-resonant MPI. The black dots are the measured data points, and the red lines are the best fits to the data.

Desorption kinetics for NH_3 from Pt(332) were measured with the VRK-LID method. The kinetic traces are fitted in the same fashion as CO, with the convolution of the MB pulse and a single exponential decay (see Equation (4.24)). The resulting fits are displayed in Figure 5.30. At most temperatures, not enough data points were recorded at low nozzle delay. Therefore, the rising edge of the MB dosing pulse is not captured by the fits. Since the decay determines the desorption kinetics, the resulting error due to some missing data should be negligible. From the fit parameters of the Arrhenius plot, the activation energy of desorption $E_D = 1.18 \pm 0.13$ eV and the prefactor $A = 10^{14.2 \pm 1.3} \text{ s}^{-1}$ are determined.

Chapter 6

Discussion

6.1 The LID process

The ultra-fast LID process, which was utilized in this work, shows all signs of the electron-mediated desorption mechanism, which were presented in Section 2.2. The fluence dependence of the flux is highly non-linear, and the power k correlates with the binding energy. The weakly bound O₂ exhibits a weak dependence with $k = 1.7 \pm 0.3$, while the strongly bound O-atoms exhibit a strong non-linear dependence of $k = 9 \pm 1$. With an intermediate binding energy, CO also shows a non-linear dependence with an intermediate power $k = 5 \pm 1$. This trend continues when looking at the pulse duration dependence: With stronger adsorbate binding energy, the dependence becomes more non-linear. The ratio between the LID mechanisms changes as well: The electron-mediated mechanism becomes more important with higher binding energy. The kinetic energy distribution also shifts to higher energy and becomes more hyperthermal with higher adsorbate binding energy, which is one degree of freedom to dissipate excess energy. Other degrees of freedom are the molecular vibration and rotation, which receive a high level of excitation in the LID of CO.

I have shown that it is possible to desorb even O-atoms from platinum, which is one of the strongest binding energies for adsorbates on surfaces. Hence, with LID, it should be possible to desorb basically all kinds of small adsorbates. I have also shown that the LID process is very selective and induces desorption without other competing pathways. For all molecules in this work, no laser-induced dissociation was observed on the surface. Some larger and less stable molecules might be unsuitable for LID if the laser irradiation causes unwanted dissociation.

6.2 Kinetic measurements

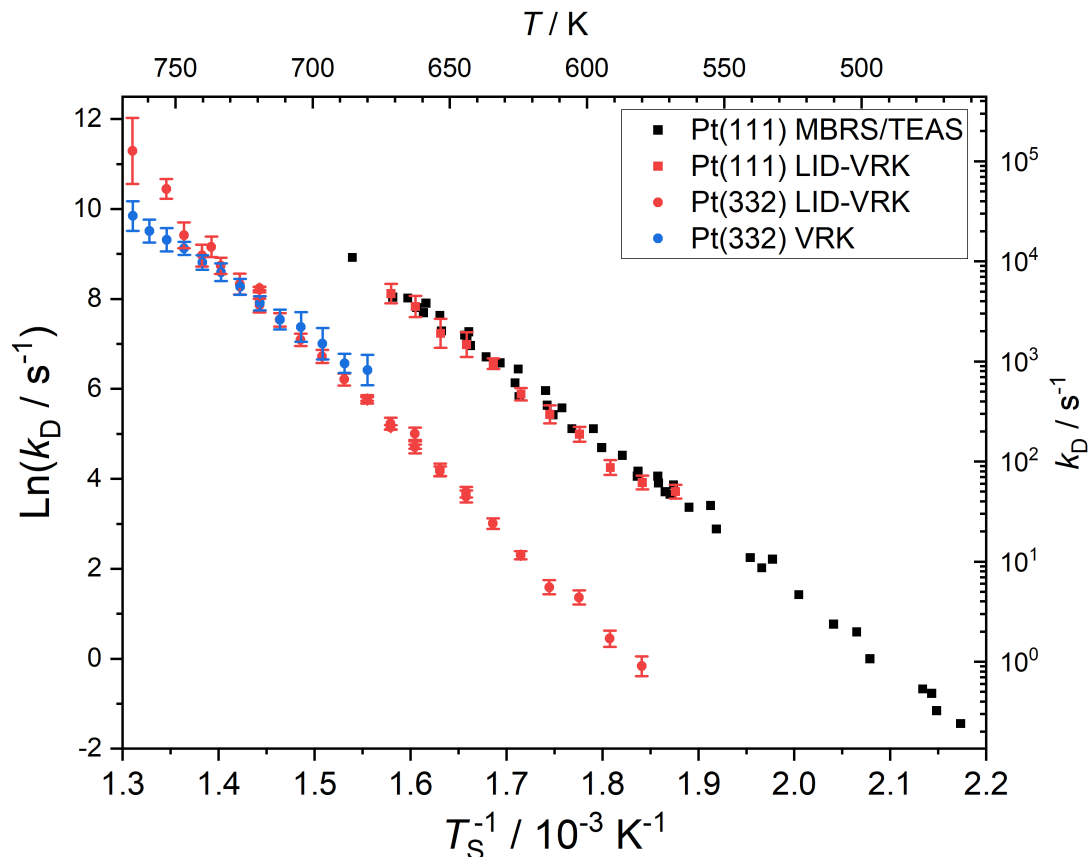


Figure 6.1: CO desorption rate constants from this work compared to literature. The squares represent desorption from Pt(111) and the circles represent the desorption from Pt(332). The colors represent different experimental methods: LID-VRK in red (This work), VRK[8] in blue and MBRs/TEAS[5] in black.

To validate that the new LID-VRK method reproduces the desorption rate constants of CO correctly, the results are compared to the literature in Figure 6.1. The literature values were measured with VRK(see Section 4.3.1)[63, 8, 12], phase-lag[3] or a combination of molecular beam relaxation spectroscopy (MBRS) and thermal energy atom scattering (TEAS)[5]. The absolute rate constants from Pt(111) and Pt(332) are in good agreement for the majority of the temperature range. Only at very high temperatures above 750 K, there are some deviations for Pt(332). The discrepancies could be explained by the higher uncertainty in the determination of the rate constants at these relatively high temperatures (see Section 5.3.8). The desorption rate constants of NH_3 from Pt(332) are also compared to literature in Figure 6.2 and agree very well.

The Arrhenius parameters are summarized in Table 6.1. They should be taken with care because they are strongly correlated and can be misleading and blow small differences out of proportion. This is the case for Pt(332) where the differences in the Arrhenius parameters seem large in comparison to the VRK results. The Pt(332) LID-VRK data of CO shows a linear Arrhenius behavior over a large temperature range of more than 150 K, which is more than double the temperature

range of the VRK data[8]. For ammonia from Pt(332)[12] and CO from Pt(111)[1, 5] the Arrhenius parameters agree well with the literature. The difference of the activation energies between Pt(111) and Pt(332) for CO desorption is 0.22 ± 0.05 eV and corresponds to the difference between steps and terraces. This is reasonable agreement with the difference in activation energy of 0.16 eV for CO on the Pt(557) surface[3], which has very similar kind of steps as Pt(332).

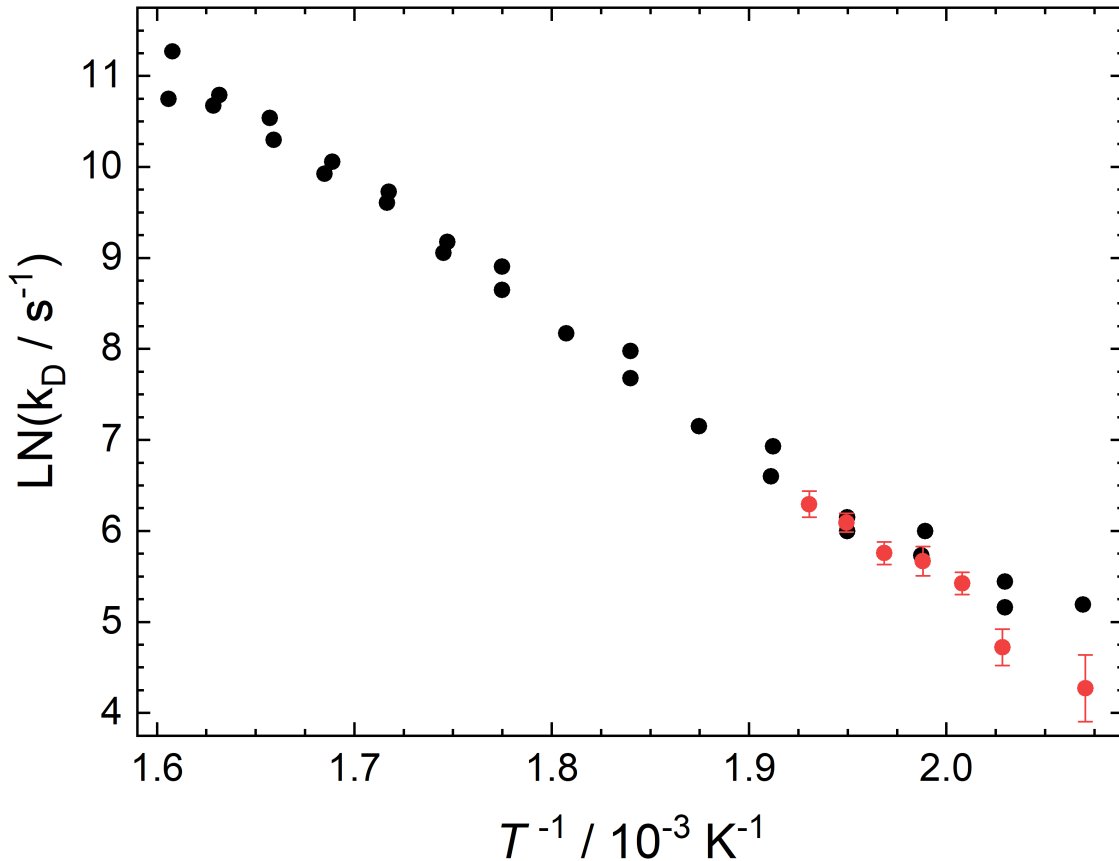


Figure 6.2: Arrhenius plot of the desorption rate constants of NH_3 from Pt(332). The red dots are the measured rate constants from the kinetic traces in Figure 5.30 and the black dots are taken from Borodin *et al.* [12] obtained with VRK.

An improved analysis would involve using transition state theory (TST) instead of the Arrhenius equation (Equation (4.21)) to model the temperature dependence of the rate constant. Recently, this has been applied successfully to VRK desorption measurements[85, 12] to obtain binding energies and rate constants of elementary steps.

The inner consistency of the LID-VRK data and the comparison of the rate constants with literature confirms that this method is capable of measuring the desorption kinetics of CO and NH_3 from platinum accurately. Expanding the method to other adsorbates or substrates should be easily possible. But the specifications of the laser and detection system must be reevaluated for each adsorbate/substrate systems. For example, the ablation threshold surely will be different for another substrate and needs to be newly determined. Also, the binding energy of the adsorbate on the surface is an important factor for the desorption yield and the temperature dependence.

substrate	adsorbate	method	E_D / eV	$\log_{10}(A / \text{s}^{-1})$
Pt(111)	CO	LID-VRK	1.43	14.9
Pt(111)	CO	VRK[63]	1.28	13.8
Pt(111)	CO	MBRS/TEAS[5]	1.39	14.8
Pt(332)	CO	LID-VRK	1.65	15.7
Pt(332)	CO	VRK[8]	1.26	12.6
Pt(557)	CO	Phase-lag[3]	1.46	13.9
Pt(332)	NH ₃	LID-VRK	1.18	14.2
Pt(332)	NH ₃	VRK[12]	1.17	14.2

Table 6.1: Summary of Arrhenius parameters for the desorption of CO and NH₃ from Pt(111) and Pt(332) and comparison with literature.

6.3 Binding energy of CO on Pt(111)

As shown in Section 5.3.2, LID can be used to measure adsorption isotherms. The isosteric heat of adsorption ΔH_{Ad} can be understood as the binding energy of the adsorbates on the Pt(111) surface. The value for $\Delta H_{\text{Ad}} = 1.03 \text{ eV}$, for the low coverage limit, does not agree well with early isotherm measurements by Ertl *et al.* [1] or newer calorimetric measurements[86] with values of 1.40 eV and 1.35 eV, respectively.

The explanation for the underestimation of ΔH_{Ad} could be either an error in the analysis or in the experiment. Despite taking great care, maybe the experimental conditions were unsuitable for the assumption made for the isotherm measurements, that the equilibrium is reestablished between each LID laser shot.

The adsorption of CO on Pt(111) is not an activated process[1] which is indicative from the observation that the initial sticking probability decreases with T_S [87]. An example for an activated adsorption process is the dissociation of oxygen, where the initial sticking probability increases with T_S , as shown by the increase of the LID flux with T_S in Figure 5.25. Because the CO adsorption is barrierless, the activation energy of desorption, E_D , is closely related to the binding energy[63]. When comparing the obtained value of $E_D = 1.43 \text{ eV}$, to the isotherm and calorimetric measurements in the literature mentioned above[1, 86], the agreement is very good.

6.4 Oxygen desorption kinetics

Unfortunately, I could not measure the recombinative desorption of oxygen, which is a second order reaction. The kinetics appear to be too slow at the maximum reachable surface temperature of $T_S = 1173 \text{ K}$. Hence, implementing a different heating technique like electron bombardment heating could be helpful. The main problem then would probably be, that the O-atom coverage from one O₂ MB pulse is just too low. To overcome this problem, a stronger MB could be implemented or a different gas than O₂ could be used for the MB dosing. Good candidate gases would be NO₂[88, 89] or ozone[90]. Those studies achieved a very high maximum coverage of O-atoms, but at temperatures far below 1173 K. These possibilities are promising because these gases have a high sticking probability and dissociate readily to NO or O₂ while leaving behind oxygen atoms on the surface. Dosing a large coverage of

O-atoms with a MB beam of O-atoms is also possible[91] and eliminates the dissociation barrier completely.

Another idea could be to look at the kinetics of a different oxygen desorption reaction, the desorption of molecular O₂ from the chemisorbed state. For this, cryogenic temperatures around 100 K would be necessary to suppress the dissociation reaction, which starts around 150 K[82]. At similar temperatures the molecular oxygen also starts to desorb which might make it difficult to find a temperature range with sufficiently fast desorption without dissociation. If that is not possible, the dissociation has to be taken into account for the kinetic model because it would reduce the measured O₂ coverage and block more and more binding sites over the course of one experiment.

6.5 Reaction intermediates

The main motivation of this work was the prospect of measuring the coverage of reaction intermediates on a surface, which promises new insights into reactions on catalysts. Examples of reaction intermediate detection in the gas phase by LITD[92] or directly on the surface[93] can be found, but are rather rare. Probing reaction intermediates was beyond the scope of this work, but I expect this new kinetic method, that I developed and presented here, to be capable of recording the kinetic traces of reaction intermediates. In fact, these measurements are planned for the near future. First, the OH radical intermediate in the catalytic oxidation of hydrogen will be studied. This reaction is relatively simple with no other intermediates and only water as reaction product. However, the reaction mechanism is still not completely understood[46, 11]. Following the time-dependent coverage of the OH intermediate with LID-VRK might provide invaluable information to help to explain the mechanism.

A second step would be the investigation of the catalytic oxidation of ammonia, also known as the Ostwald process. This reaction is more complicated with three main products, NO, N₂ and H₂O, and many possible intermediates as NH₂, NH, OH, N-atoms and O-atoms[94, 95, 96, 12]

6.6 Summary

To conclude, I will summarize some advantages and disadvantages of the new LID-VRK method presented in this work.

Probably the biggest advantage is that, in theory, the kinetic trace of all kinds of adsorbates is obtainable, including reactive intermediates. Other desorption measurements are restricted to molecules that are stable in the gas phase that can desorb thermally. Reaction intermediates though do not thermally desorb, but instead they simply chemically react to the reaction products. Another advantage is that the measured LID flux depends much less on the surface temperature. Other methods record the thermally desorbing flux directly, which falls off with decreasing surface temperature. This is not the case with LID-VRK and it is possible to measure slow kinetics at low surface temperature. This comes in addition to the fast high temperature kinetics and expands the kinetic measurements over a large

temperature range. The analysis of the data is also simpler than in VRK because of the velocity slicing and the absence of the direct scattering component in the flux.

One disadvantage of this method is that rather unstable substrates or adsorbates could be unusable with this method if the laser irradiation causes the adsorbates to dissociate or the substrate to ablate. Reducing the laser fluence could circumvent this problem, but also reduces the yield. Another disadvantage is that measuring real time kinetics is not possible. Real-time kinetics use a detection laser with kHz repetition rate to measure the whole kinetic trace during a single MB pulse with a resolution of at least 1 ms[97]. We recently published a paper about real-time kinetics using an event based camera[98] for VRK. This approach is not compatible with LID-VRK because the LID laser pulse desorbes a significant portion of the coverage, which would interfere with the subsequent data points. LID-VRK must be conducted as Delay Scan so that each laser shot probes a freshly dosed coverage without influence of the previous laser shot.

Appendix A

Pixel to mm conversion

Figure A.1 shows the inner and outer ring of the extraction grid on the image. The respective diameters, of 46 mm and 49 mm, are known from manufacturing. By measuring the diameter of the rings on the image in units of pixels, the conversion factor can be determined to $52 \mu\text{m}/\text{pxl}$.

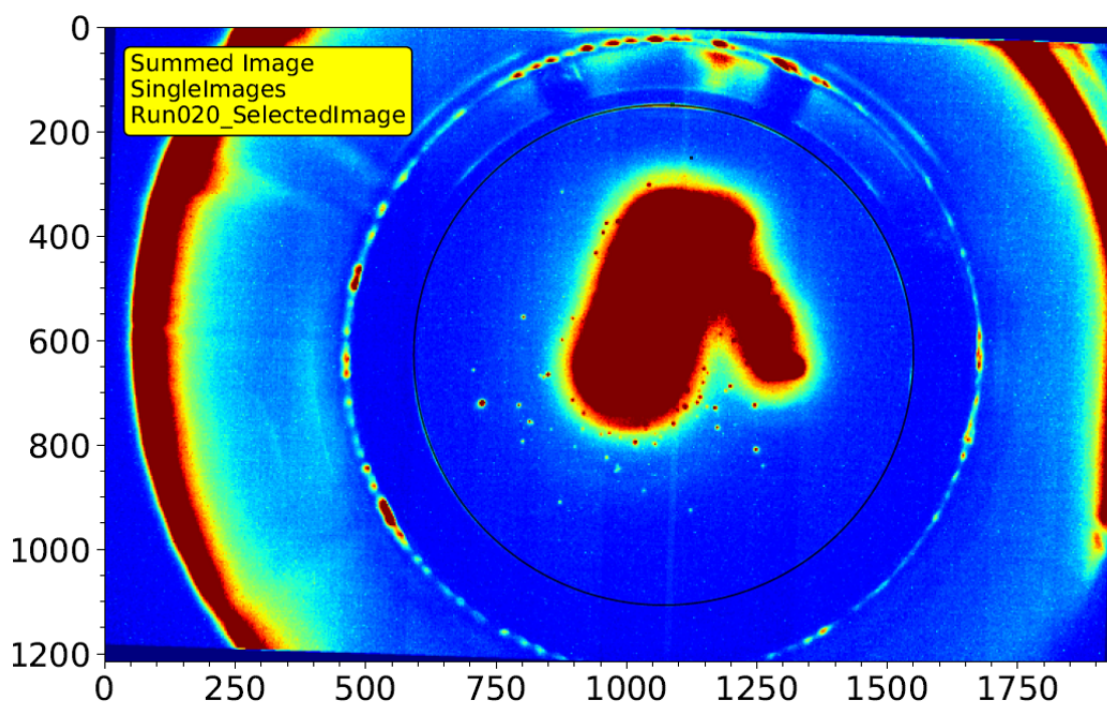


Figure A.1: Bright image to make the outer and inner ring clearly visible, which correspond to the extraction grid.

Appendix B

Kinetic traces

Figure B.1 through Figure B.5 show all the kinetic traces of CO used to determine the rate constants, which are depicted in Figure 5.22. The data points are drawn as black dots and the best fits as red lines. The relevant parameters are noted in the captions.

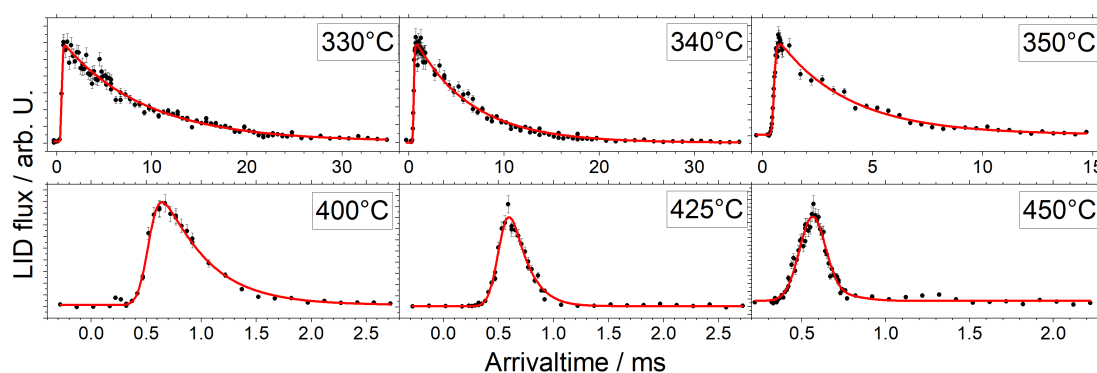


Figure B.1: Kinetic traces of CO from Pt(332) using the wavelength of the (1,1) Q-head and the PGV nozzle at 50 Hz.

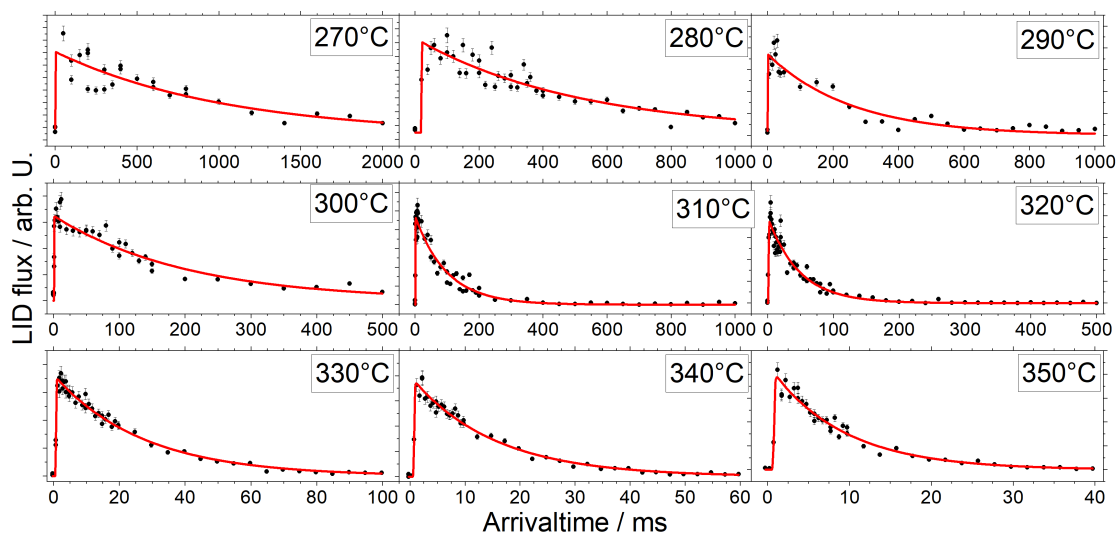


Figure B.2: Kinetic traces of CO from Pt(332) using the wavelength of the (1,1) Q-head and the PGV nozzle at 0.5 to 25 Hz.

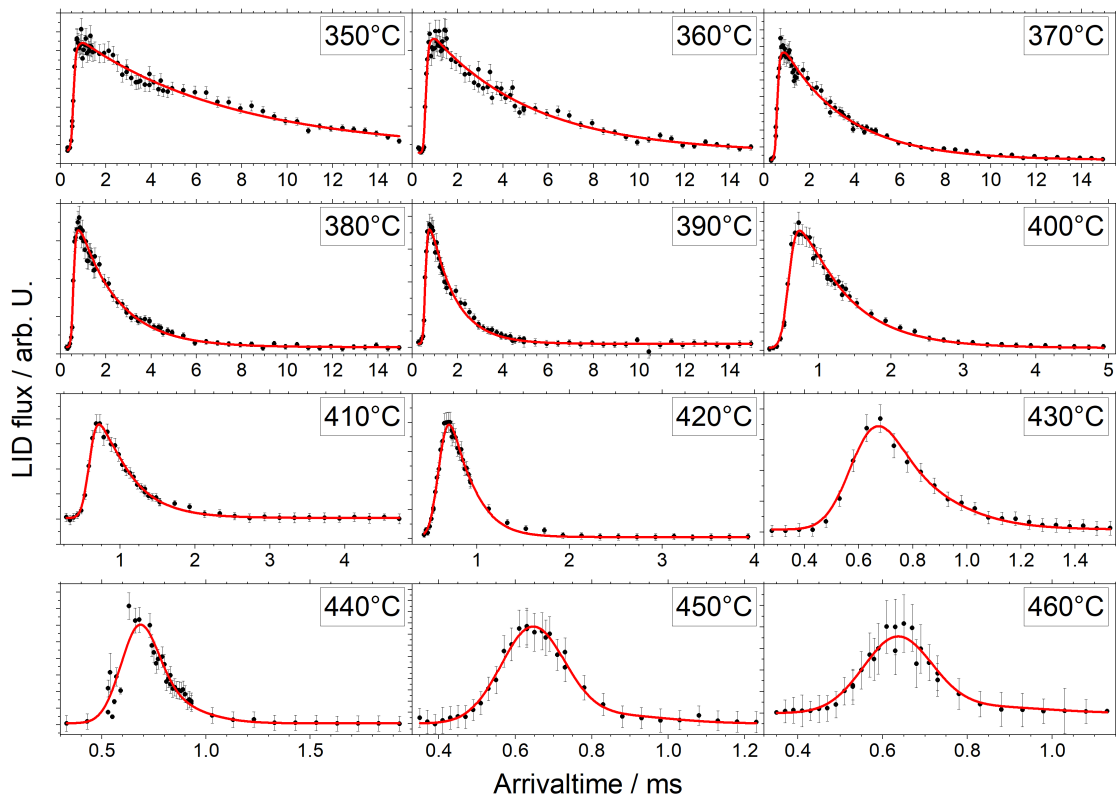


Figure B.3: Kinetic traces of CO from Pt(332) using the wavelength of the (0,0) Q-head and the ELT nozzle at 50 Hz.

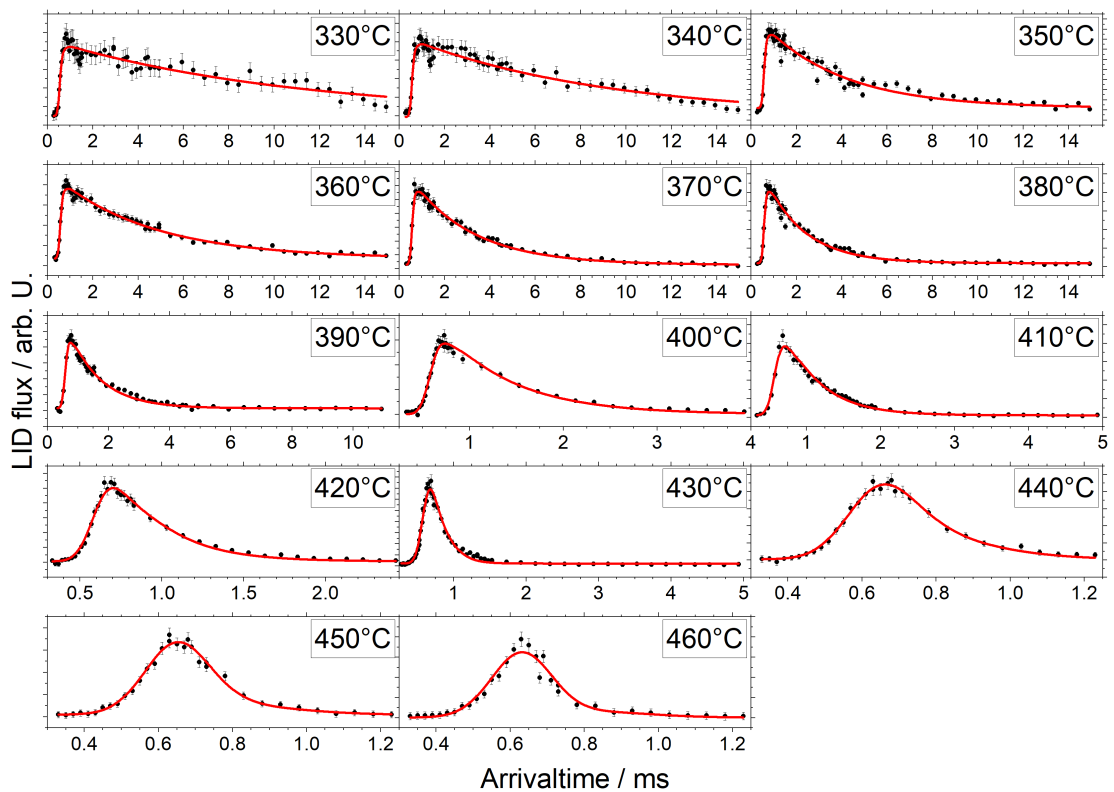


Figure B.4: Kinetic traces of CO from Pt(332) using the wavelength of the (1,1) Q-head and the ELT nozzle at 50 Hz.

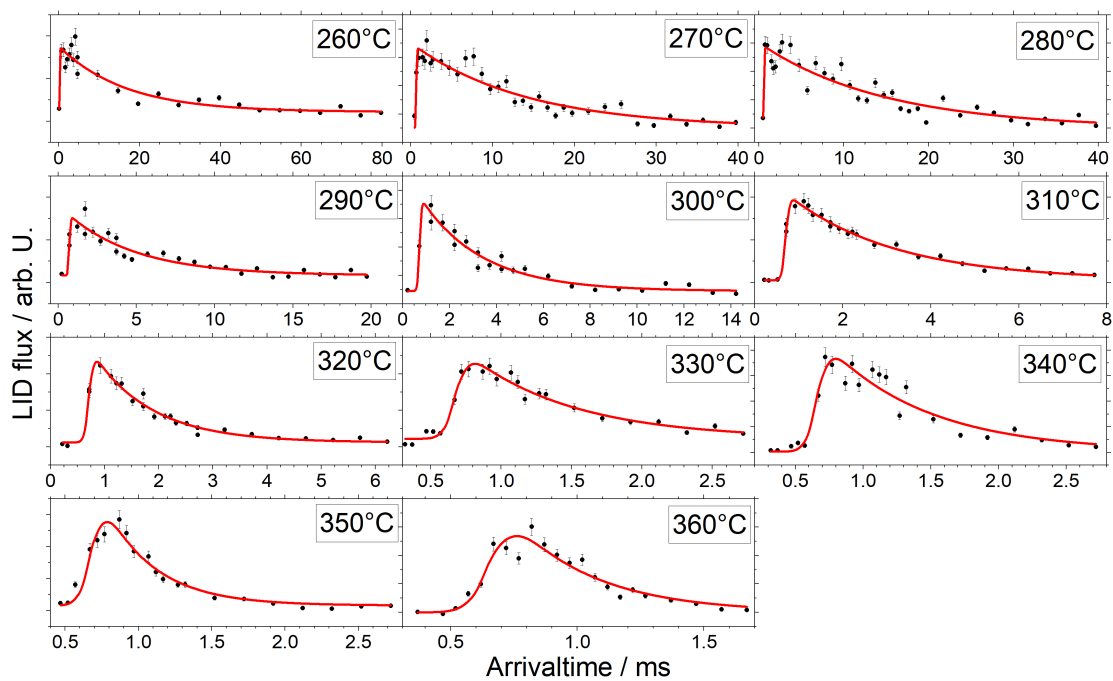


Figure B.5: Kinetic traces of CO from Pt(111) using the wavelength of the (1,1) Q-head and the PGV nozzle with 10-50 Hz.

Bibliography

- [1] G. Ertl, M. Neumann, and K. M. Streit. “Chemisorption of Co on Pt(111) Surface”. In: *Surface Science* 64.2 (1977), pp. 393–410. DOI: [Doi10.1016/0039-6028\(77\)90052-8](https://doi.org/10.1016/0039-6028(77)90052-8).
- [2] C. T. Campbell *et al.* “A Molecular-Beam Investigation of the Interactions of Co with a Pt(111)Surface”. In: *Surface Science* 107.1 (1981), pp. 207–219.
- [3] T. H. Lin and G. A. Somorjai. “Modulated molecular beam scattering of CO and NO from Pt(111) and the stepped Pt(557) crystal surfaces”. In: *Surface Science* 107.2 (1981), pp. 573–585. DOI: [https://doi.org/10.1016/0039-6028\(81\)90546-X](https://doi.org/10.1016/0039-6028(81)90546-X).
- [4] D. H. Winicur *et al.* “Co desorption and adsorption on Pt(111)”. In: *Surface Science* 109.1 (1981), pp. 263–275. DOI: [http://dx.doi.org/10.1016/0039-6028\(81\)90523-9](http://dx.doi.org/10.1016/0039-6028(81)90523-9).
- [5] L. K. Verheij *et al.* “A molecular beam study of the interaction of CO molecules with a Pt(111) surface using pulse shape analysis”. In: *Surface Science* 182.3 (1987), pp. 390–410. DOI: [http://dx.doi.org/10.1016/0039-6028\(87\)90008-2](http://dx.doi.org/10.1016/0039-6028(87)90008-2).
- [6] J. S. Luo *et al.* “CO adsorption site occupation on Pt(335): a quantitative investigation using TPD and EELS”. In: *Surface Science* 274.1 (1992), pp. 53–62. DOI: [https://doi.org/10.1016/0039-6028\(92\)90099-R](https://doi.org/10.1016/0039-6028(92)90099-R).
- [7] K. Golibrzuch *et al.* “CO Desorption from a Catalytic Surface: Elucidation of the Role of Steps by Velocity-Selected Residence Time Measurements”. In: *Journal of the American Chemical Society* 137.4 (2015), pp. 1465–1475. DOI: [10.1021/ja509530k](https://doi.org/10.1021/ja509530k).
- [8] J. Neugeboren *et al.* “Velocity-resolved kinetics of site-specific carbon monoxide oxidation on platinum surfaces”. In: *Nature* 558.7709 (2018), pp. 280–+. DOI: [10.1038/s41586-018-0188-x](https://doi.org/10.1038/s41586-018-0188-x).
- [9] G. B. Park *et al.* “The kinetics of elementary thermal reactions in heterogeneous catalysis”. In: *Nature Reviews Chemistry* 3.12 (2019), pp. 723–732. DOI: [10.1038/s41570-019-0138-7](https://doi.org/10.1038/s41570-019-0138-7).
- [10] L. S. Zhou *et al.* “Origin of Thermal and Hyperthermal CO₂ from CO Oxidation on Pt Surfaces: The Role of Post-Transition-State Dynamics, Active Sites, and Chemisorbed CO₂”. In: *Angewandte Chemie-International Edition* 58.21 (2019), pp. 6916–6920. DOI: [10.1002/anie.201900565](https://doi.org/10.1002/anie.201900565).
- [11] D. Borodin *et al.* “The puzzle of rapid hydrogen oxidation on Pt(111)”. In: *Molecular Physics* (2021). DOI: [10.1080/00268976.2021.1966533](https://doi.org/10.1080/00268976.2021.1966533).

- [12] D. Borodin *et al.* “Kinetics of NH₃ Desorption and Diffusion on Pt: Implications for the Ostwald Process”. In: *Journal of the American Chemical Society* 143.43 (2021), pp. 18305–18316. DOI: 10.1021/jacs.1c09269.
- [13] G. Ertl and M. Neumann. “Rapid Laser-Beam Induced Thermal Desorption from Solid Surfaces”. In: *Zeitschrift Fur Naturforschung Section a-a Journal of Physical Sciences A* 27.11 (1972), pp. 1607–1610.
- [14] J. H. Bechtel. “Heating of Solid Targets with Laser Pulses”. In: *Journal of Applied Physics* 46.4 (1975), pp. 1585–1593.
- [15] M. Lax. “Temperature rise induced by a laser beam”. In: *Journal of Applied Physics* 48.9 (1977), pp. 3919–3924. DOI: 10.1063/1.324265.
- [16] D. Burgess, P. C. Stair, and E. Weitz. “Calculations of the surface temperature rise and desorption temperature in laser-induced thermal desorption”. In: *Journal of Vacuum Science & Technology A: Vacuum, Surfaces, and Films* 4.3 (1986), pp. 1362–1366. DOI: 10.1116/1.573571.
- [17] R. B. Hall. “Pulsed-laser-induced desorption studies of the kinetics of surface reactions”. In: *The Journal of Physical Chemistry* 91.5 (1987), pp. 1007–1015. DOI: 10.1021/j100289a003.
- [18] W. Ho. “Reactions at metal surfaces induced by femtosecond lasers, tunneling electrons, and heating”. In: *Journal of Physical Chemistry* 100.31 (1996), pp. 13050–13060.
- [19] J. A. Prybyla *et al.* “Desorption Induced by Femtosecond Laser-Pulses”. In: *Physical Review Letters* 64.13 (1990), pp. 1537–1540. DOI: DOI10.1103/PhysRevLett.64.1537.
- [20] D. G. Busch and W. Ho. “Direct observation of the crossover from single to multiple excitations in femtosecond surface photochemistry”. In: *Physical Review Letters* 77.7 (1996), pp. 1338–1341.
- [21] W. Ho. “Femtosecond laser-induced dynamical quantum processes on solid surfaces (DQPSS)”. In: *Surface Science* 363.1-3 (1996), pp. 166–178.
- [22] D. M. Newns, T. F. Heinz, and J. A. Misewich. “Desorption by Femtosecond Laser-Pulses - an Electron-Hole Effect”. In: *Progress of Theoretical Physics Supplement* 106 (1991), pp. 411–418.
- [23] J. A. Misewich *et al.* “Femtosecond Surface Dynamics - Desorption Induced by Multiple Electronic-Transitions”. In: *Abstracts of Papers of the American Chemical Society* 204 (1992), 260–Phys.
- [24] J. A. Misewich, T. F. Heinz, and D. M. Newns. “Desorption induced by multiple electronic transitions”. In: *Phys Rev Lett* 68.25 (1992), pp. 3737–3740. DOI: 10.1103/PhysRevLett.68.3737.
- [25] R. R. Cavanagh *et al.* “Dynamics of Nonthermal Reactions - Femtosecond Surface-Chemistry”. In: *Journal of Physical Chemistry* 97.4 (1993), pp. 786–798. DOI: DOI10.1021/j100106a002.
- [26] M. Brandbyge *et al.* “Electronically Driven Adsorbate Excitation Mechanism in Femtosecond-Pulse Laser-Desorption”. In: *Physical Review B* 52.8 (1995), pp. 6042–6056. DOI: DOI10.1103/PhysRevB.52.6042.

- [27] F. Kao *et al.* “Femtosecond laser desorption of molecularly adsorbed oxygen from Pt(111)”. In: *Phys Rev Lett* 71.13 (1993), pp. 2094–2097. DOI: 10.1103/PhysRevLett.71.2094.
- [28] D. G. Busch *et al.* “Femtosecond Desorption Dynamics Probed by Time-Resolved Velocity Measurements”. In: *Physical Review Letters* 75.4 (1995), pp. 673–676. DOI: 10.1103/PhysRevLett.75.673.
- [29] S. Gao, D. G. Busch, and W. Ho. “Femtosecond dynamics of electron-vibrational heating and desorption”. In: *Surface Science* 344.3 (1995), pp. L1252–L1258. DOI: [https://doi.org/10.1016/0039-6028\(95\)00927-2](https://doi.org/10.1016/0039-6028(95)00927-2).
- [30] L. Cai, X. D. Xiao, and M. M. T. Loy. “Femtosecond laser desorption of CO from the Pt(111) surface”. In: *Surface Science* 464.2-3 (2000), pp. L727–L731.
- [31] F. Budde *et al.* “Vibrational Distributions in Desorption Induced by Femtosecond Laser-Pulses - Coupling of Adsorbate Vibration to Substrate Electronic Excitation”. In: *Surface Science* 283.1-3 (1993), pp. 143–157.
- [32] J. A. Misewich *et al.* “Vibrationally Assisted Electronic Desorption - Femtosecond Surface-Chemistry of O₂/Pd(111)”. In: *Journal of Chemical Physics* 100.1 (1994), pp. 736–739.
- [33] J. A. Misewich *et al.* “Anomalous branching ratio in the femtosecond surface chemistry of O₂/Pd(111)”. In: *Surface Science* 363.1-3 (1996), pp. 204–213. DOI: Doi10.1016/0039-6028(96)00138-0.
- [34] J. A. Prybyla, H. W. K. Tom, and G. D. Aumiller. “Femtosecond Time-Resolved Surface-Reaction - Desorption of Co from Cu(111) in Less-Than 325 Fsec”. In: *Physical Review Letters* 68.4 (1992), pp. 503–506. DOI: DOI10.1103/PhysRevLett.68.503.
- [35] C. Springer, M. Headgordon, and J. C. Tully. “Simulations of Femtosecond Laser-Induced Desorption of Co from Cu(100)”. In: *Surface Science* 320.1-2 (1994), pp. L57–L62. DOI: Doi10.1016/0039-6028(94)00569-9.
- [36] C. Springer and M. HeadGordon. “Simulations of the femtosecond laser-induced desorption of CO from Cu(100) at 0.5 ML coverage”. In: *Chemical Physics* 205.1-2 (1996), pp. 73–89.
- [37] L. M. Struck *et al.* “Femtosecond laser-induced desorption of CO from Cu(100): Comparison of theory and experiment”. In: *Physical Review Letters* 77.22 (1996), pp. 4576–4579.
- [38] J. A. Serri, J. C. Tully, and M. J. Cardillo. “The Influence of Steps on the Desorption-Kinetics of No from Pt(111)”. In: *Journal of Chemical Physics* 79.3 (1983), pp. 1530–1540. DOI: Doi10.1063/1.445946.
- [39] V. J. Kwasniewski and L. D. Schmidt. “Surface diffusion of CO on Pt(111)”. In: *Surface Science* 274.3 (1992), pp. 329–340. DOI: [https://doi.org/10.1016/0039-6028\(92\)90838-W](https://doi.org/10.1016/0039-6028(92)90838-W).
- [40] D. Bejan. “Photodesorption of molecular adsorbates from metallic surfaces”. In: *Journal of Optoelectronics and Advanced Materials* 6.2 (2004), pp. 359–384.

- [41] S. Funk *et al.* “Desorption of CO from Ru(001) induced by near-infrared femtosecond laser pulses”. In: *Journal of Chemical Physics* 112.22 (2000), pp. 9888–9897.
- [42] M. Bonn *et al.* “Ultrafast electron dynamics at metal surfaces: Competition between electron-phonon coupling and hot-electron transport”. In: *Physical Review B* 61.2 (2000), pp. 1101–1105. DOI: 10.1103/PhysRevB.61.1101.
- [43] E. G. Seebauer, A. C. F. Kong, and L. D. Schmidt. “Adsorption and Desorption of No, Co and H-2 on Pt(111) - Laser-Induced Thermal-Desorption Studies”. In: *Surface Science* 176.1-2 (1986), pp. 134–156.
- [44] E. G. Seebauer and L. D. Schmidt. “Surface-Diffusion of Hydrogen on Pt(111) - Laser-Induced Thermal-Desorption Studies”. In: *Chemical Physics Letters* 123.1-2 (1986), pp. 129–133.
- [45] J. P. Cowin *et al.* “Measurement of Fast Desorption-Kinetics of D2 from Tungsten by Laser-Induced Thermal Desorption”. In: *Surface Science* 78.3 (1978), pp. 545–564.
- [46] V. J. Kwasniewski and L. D. Schmidt. “Steps in the reaction hydrogen + oxygen .dblharw. water on platinum(111): laser-induced thermal desorption at low temperature”. In: *The Journal of Physical Chemistry* 96.14 (1992), pp. 5931–5938. DOI: 10.1021/j100193a052.
- [47] W. S. M. Werner, K. Glantschnig, and C. Ambrosch-Draxl. “Optical Constants and Inelastic Electron-Scattering Data for 17 Elemental Metals”. In: *Journal of Physical and Chemical Reference Data* 38.4 (2009), pp. 1013–1092. DOI: 10.1063/1.3243762.
- [48] Sergei I. Anisimov, B. L. Kapeliovich, and T. L. Perelman. “Electron emission from metal surfaces exposed to ultrashort laser pulses”. In: *Journal of Experimental and Theoretical Physics* (1974).
- [49] L. Cai, X. Xiao, and M. M. T. Loy. “Femtosecond desorption of CO from metal surfaces: the role of the 2pi*-derived states”. In: *Surface Science* 492.1 (2001), pp. L688–L692. DOI: [https://doi.org/10.1016/S0039-6028\(01\)01439-X](https://doi.org/10.1016/S0039-6028(01)01439-X).
- [50] K. Fukutani *et al.* “Uv-Laser-Induced Desorption of No from Pt(111)”. In: *Surface Science* 311.1-2 (1994), pp. 247–256.
- [51] K. Stépan *et al.* “Laser-induced diffusion of oxygen on a stepped Pt(111) surface”. In: *Surface Science* 593.1 (2005), pp. 54–66. DOI: <https://doi.org/10.1016/j.susc.2005.06.047>.
- [52] K. D. Childs. *Handbook of Auger electron spectroscopy : a book of reference data for identification and interpretation in Auger electron spectroscopy*. Vol. 3. Eden Prairie, Minnesota: Physical Eletronics Industries, Inc., 1995.
- [53] W. P. Ellis and R. L. Schwoebel. “Leed from Surface Steps on Uo2 Single Crystals”. In: *Surface Science* 11.1 (1968), pp. 82–+. DOI: [Doi10.1016/0039-6028\(68\)90040-X](https://doi.org/10.1016/0039-6028(68)90040-X).
- [54] U. Even. “The Even-Lavie valve as a source for high intensity supersonic beam”. In: *Epj Techniques and Instrumentation* 2 (2015). DOI: 10.1140/epjti/s40485-015-0027-5.

- [55] P. J. H. Tjossem and K. C. Smyth. “Multiphoton Excitation Spectroscopy of the B1sigma+ and C1sigma+ Rydberg States of Co”. In: *Journal of Chemical Physics* 91.4 (1989), pp. 2041–2048. DOI: Doi10.1063/1.457064.
- [56] D. J. Bamford, L. E. Jusinski, and W. K. Bischel. “Absolute two-photon absorption and three-photon ionization cross sections for atomic oxygen”. In: *Physical Review A* 34.1 (1986), pp. 185–198. DOI: 10.1103/PhysRevA.34.185.
- [57] G. Herzberg. “Forbidden Transitions in Diatomic Molecules .2. The 3-Sigma-U+]-3-Sigma-G(-) Absorption Bands of the Oxygen Molecule”. In: *Canadian Journal of Physics* 30.3 (1952), pp. 185–&. DOI: DOI10.1139/p52-019.
- [58] D. W. Chandler and P. L. Houston. “Two-Dimensional Imaging of State-Selected Photodissociation Products Detected by Multiphoton Ionization”. In: *Journal of Chemical Physics* 87.2 (1987), pp. 1445–1447. DOI: Doi10.1063/1.453276.
- [59] A. Eppink and D. H. Parker. “Velocity map imaging of ions and electrons using electrostatic lenses: Application in photoelectron and photofragment ion imaging of molecular oxygen”. In: *Review of Scientific Instruments* 68.9 (1997), pp. 3477–3484. DOI: 10.1063/1.1148310.
- [60] C. R. Gebhardt *et al.* “Slice imaging: A new approach to ion imaging and velocity mapping”. In: *Review of Scientific Instruments* 72.10 (2001), pp. 3848–3853. DOI: Doi10.1063/1.1403010.
- [61] D. J. Harding *et al.* “Using Ion Imaging to Measure Velocity Distributions in Surface Scattering Experiments”. In: *Journal of Physical Chemistry A* 119.50 (2015), pp. 12255–12262. DOI: 10.1021/acs.jpca.5b06272.
- [62] D. B. Harding. “The Crisis of Modernity”. In: *Heythrop Journal* 58.4 (2017), pp. 737–738. DOI: 10.1111/heyj.12649.
- [63] D. J. Harding *et al.* “Ion and velocity map imaging for surface dynamics and kinetics”. In: *Journal of Chemical Physics* 147.1 (2017). DOI: Artn01393910.1063/1.4983307.
- [64] C. Frischkorn and M. Wolf. “Femtochemistry at metal surfaces: Nonadiabatic reaction dynamics”. In: *Chemical Reviews* 106.10 (2006), pp. 4207–4233.
- [65] R. E. Imhof, S. T. Beckett, and F. H. Read. “Determination of Transition Moment of B1sigma+-X1sigma+ Transition in Co”. In: *Journal of Physics Part B Atomic and Molecular Physics* 5.4 (1972), pp. 896–902. DOI: Doi10.1088/0022-3700/5/4/025.
- [66] P. H. Krupenie. “The Band Spectrum of Carbon Monoxide”. In: *Nat. Bur. Stand. NSRDS-5* (1966).
- [67] W. G. Roeterdink *et al.* “Comment on ”Ultrafast laser excitation of CO/Pt(111) probed by sum frequency generation: Coverage dependent desorption efficiency””. In: *Physical Review Letters* 93.24 (2004). DOI: ARTN24960110.1103/PhysRevLett.93.249601.
- [68] E. H. G. Backus *et al.* “Real-time observation of molecular motion on a surface”. In: *Science* 310.5755 (2005), pp. 1790–1793.
- [69] M. R. Cervenán and N. R. Isenor. “Multiphoton Ionization Yield Curves for Gaussian Laser-Beams”. In: *Optics Communications* 13.2 (1975), pp. 175–178.

- [70] M. A. Hines, H. A. Michelsen, and R. N. Zare. “2+1 Resonantly Enhanced Multiphoton Ionization of Co Via the E1-II-X1-Sigma+ Transition - from Measured Ion Signals to Quantitative Population-Distributions”. In: *Journal of Chemical Physics* 93.12 (1990), pp. 8557–8564. DOI: Doi10.1063/1.459293.
- [71] W. Li *et al.* “Multiphoton processes of CO at 230 nm”. In: *Physical Chemistry Chemical Physics* 8.25 (2006), pp. 2950–2957.
- [72] Z. F. Sun *et al.* “Imaging multiphoton ionization and dissociation of rotationally warm CO via the B-1 Sigma(+) and E-1 Π electronic states”. In: *Journal of Chemical Physics* 147.1 (2017).
- [73] G. A. Somorjai. *Introduction to Surface Chemistry and Catalysis*. New York: Wiley, 1994.
- [74] K. Fukutani, M. B. Song, and Y. Murata. “Photodesorption of CO and CO+ from Pt(111): Mechanism and site specificity”. In: *The Journal of Chemical Physics* 103.6 (1995), pp. 2221–2228. DOI: 10.1063/1.469697.
- [75] P. Valentini, T. E. Schwartzentruber, and I. Cozmuta. “Molecular dynamics simulation of O-2 sticking on Pt(111) using the ab initio based ReaxFF reactive force field”. In: *Journal of Chemical Physics* 133.8 (2010). DOI: Artn08470310.1063/1.3469810.
- [76] L. Jacobse, A. den Dunnen, and L. B. Juurlink. “The molecular dynamics of adsorption and dissociation of O₂ on Pt(553)”. In: *J Chem Phys* 143.1 (2015), p. 014703. DOI: 10.1063/1.4923006.
- [77] A. Eichler and J. Hafner. “Molecular precursors in the dissociative adsorption of O-2 on Pt(111)”. In: *Physical Review Letters* 79.22 (1997), pp. 4481–4484.
- [78] A. T. Gee and B. E. Hayden. “The dynamics of O-2 adsorption on Pt(533): Step mediated molecular chemisorption and dissociation”. In: *Journal of Chemical Physics* 113.22 (2000), pp. 10333–10343.
- [79] C. T. Campbell *et al.* “A Molecular-Beam Study of the Adsorption and Desorption of Oxygen from a Pt(111)Surface”. In: *Surface Science* 107.1 (1981), pp. 220–236.
- [80] A. J. Alexander, Z. H. Kim, and R. N. Zare. “Photodissociation of O-2 via the Herzberg continuum: Measurements of O-atom alignment and orientation”. In: *Journal of Chemical Physics* 118.23 (2003), pp. 10566–10574.
- [81] D. H. Parker and A. T. J. B. Eppink. “Photoelectron and photofragment velocity map imaging of state-selected molecular oxygen dissociation/ionization dynamics”. In: *The Journal of Chemical Physics* 107.7 (1997), pp. 2357–2362. DOI: 10.1063/1.474624.
- [82] J. L. Gland. “Molecular and Atomic Adsorption of Oxygen on the Pt(111) and Pt(S)-12(111)X(111) Surfaces”. In: *Surface Science* 93.2-3 (1980), pp. 487–514. DOI: Doi10.1016/0039-6028(80)90278-2.
- [83] H. Wang *et al.* “Adsorption and dissociation of oxygen on Pt(335)”. In: *Surface Science* 372.1-3 (1997), pp. 267–278. DOI: Doi10.1016/S0039-6028(96)01101-6.

- [84] D. P. Sobczyk *et al.* “Activation of ammonia dissociation by oxygen on platinum sponge studied with positron emission profiling”. In: *Journal of Catalysis* 219.1 (2003), pp. 156–166. DOI: 10.1016/s0021-9517(03)00191-x.
- [85] D. Borodin *et al.* “NO Binding Energies to and Diffusion Barrier on Pd Obtained with Velocity-Resolved Kinetics”. In: *Journal of Physical Chemistry C* 125.21 (2021), pp. 11773–11781. DOI: 10.1021/acs.jpcc.1c02965.
- [86] J. H. Fischer-Wolfarth *et al.* “An improved single crystal adsorption calorimeter for determining gas adsorption and reaction energies on complex model catalysts”. In: *Review of Scientific Instruments* 82.2 (2011).
- [87] B. Poelsema, L. K. Verheij, and G. Comsa. “Temperature Dependency of the Initial Sticking Probability of H-2 and Co on Pt(111)”. In: *Surface Science* 152.Apr (1985), pp. 496–504.
- [88] M. E. Bartram, R. G. Windham, and B. E. Koel. “The Molecular Adsorption of Nitrogen-Dioxide on Pt(111) Studied by Temperature Programmed Desorption and Vibrational Spectroscopy”. In: *Surface Science* 184.1-2 (1987), pp. 57–74.
- [89] D. H. Parker, M. E. Bartram, and B. E. Koel. “Study of High Coverages of Atomic Oxygen on the Pt(111) Surface”. In: *Surface Science* 217.3 (1989), pp. 489–510. DOI: Doi10.1016/0039-6028(89)90443-3.
- [90] N. Saliba *et al.* “Oxidation of Pt(111) by ozone (O-3) under UHV conditions”. In: *Surface Science* 419.2-3 (1999), pp. 79–88.
- [91] J. F. Weaver, J.-J. Chen, and A. L. Gerrard. “Oxidation of Pt(111) by gas-phase oxygen atoms”. In: *Surface Science* 592.1-3 (2005), pp. 83–103. DOI: 10.1016/j.susc.2005.07.010.
- [92] D. P. Land *et al.* “Detection of Reaction Intermediates in the Conversion of Cyclohexane to Benzene on Pt(111)”. In: *Journal of the American Chemical Society* 111.15 (1989), pp. 5970–5972. DOI: DOI10.1021/ja00197a084.
- [93] W. D. Mieher and W. Ho. “Thermally Activated Oxidation of Nh3 on Pt(111) - Intermediate Species and Reaction-Mechanisms”. In: *Surface Science* 322.1-3 (1995), pp. 151–167. DOI: Doi10.1016/0039-6028(95)90026-8.
- [94] A. Scheibe, M. Hinz, and R. Imbihl. “Kinetics of ammonia oxidation on stepped platinum surfaces”. In: *Surface Science* 576.1-3 (2005), pp. 131–144. DOI: 10.1016/j.susc.2004.12.007.
- [95] A. Scheibe, U. Lins, and R. Imbihl. “Kinetics of ammonia oxidation on stepped platinum surfaces. I. Experimental results”. In: *Surface Science* 577.1 (2005), pp. 1–14. DOI: 10.1016/j.susc.2004.12.027.
- [96] J. D. Gonzalez *et al.* “The effect of surface coverage on N2, NO and N2O formation over Pt(111)”. In: *Phys Chem Chem Phys* 20.39 (2018), pp. 25314–25323. DOI: 10.1039/c8cp04066d.
- [97] D. Borodin *et al.* “Measuring Transient Reaction Rates from Nonstationary Catalysts”. In: *Acs Catalysis* 10.23 (2020), pp. 14056–14066. DOI: 10.1021/acscatal.0c03773.

-
- [98] K. Golibrzuch *et al.* “Application of an Event-Based Camera for Real-Time Velocity Resolved Kinetics”. In: *The Journal of Physical Chemistry A* (2022). DOI: 10.1021/acs.jpca.2c00806.

Curriculum vitae

Personal details:

Name: Kim Papendorf
Address: Valentinsbreite 21
37077 Göttingen
Day of birth: 28.03.1989
Place of birth: Galway (Ireland)
Nationality: German

Education:

1999 - 2008 Robert-Bosch-Comprehensive school Hildesheim
Abitur
10/2009 – 07/2012 Georg-August-University Göttingen
Bachelor of Science
10/2012 – 06/2017 Georg-August-University Göttingen
Master of Science
Since 10/2017 Georg-August-University Göttingen
PhD student

Civilian service:

07/2008 – 04/2009 St. Bernwards Hospital Hildesheim
Hospital nurse

Further education:

2019 - 2021 Friedrich-Schiller University Jena
Distance studies on lasertechnology
instructed by Dr. S. Gräf